Mon. Not. R. Astron. Soc. **000**, 000–000 (0000) Printed 29 October 2010 (MN LATEX style file v2.2)

A joint analysis of BLAST 250–500 μm and LABOCA 870 μm observations in the Extended Chandra Deep Field South

Edward L. Chapin[1⋆], Scott C. Chapman[2], Kristen E. Coppin[3], Mark J. Devlin[4], [1]Dept. of James S. Dunlop[5], Thomas R. Greve[6,7], Mark Halpern[1], Matthew F. Hasselfield[1], David H. Hughes[8], Rob J. Ivison[9,5], Gaelen Marsden[1], Lorenzo Moncelsi[10], Calvin B. Netterfield[11,12], Enzo Pascale[10], Douglas Scott[1], Ian Smail[3], Marco Viero[11], Fabian Walter[6], Axel Weiss[13], Paul van der Werf[14]
[2]*Institute of Astronomy, University of Cambridge, Madingley Road, Cambridge CB3 0HA, UK*
[3]*Institute for Computational Cosmology, Durham University, South Road, Durham DH1 3LE, UK*
[4]*Department of Physics and Astronomy, University of Pennsylvania, 209 South 33rd Street, Philadelphia, PA 19104, USA*
[5]*SUPA† Institute for Astronomy, University of Edinburgh, Royal Observatory, Blackford Hill, Edinburgh, EH9 3HJ, UK*
[6]*Max-Planck Institute für Astronomie, Königstuhl 17 D-69117, Heidelberg, Germany*
[7]*Dark Cosmology Centre, Niels Bohr Institute, University of Copenhagen, Juliane Maries Vej 30, DK-2100 Copenhagen, Denmark*
[8]*Instituto Nacional de Astrofísica, Óptica y Electrónica (INAOE), Aptdo. Postal 51 y 216, Puebla, Mexico*
[9]*UK Astronomy Technology Centre, Royal Observatory, Blackford Hill, Edinburgh, EH9 3HJ, UK*
[10]*School of Physics & Astronomy, Cardiff University, 5 The Parade, Cardiff, CF24 3AA, UK*
[11]*Department of Astronomy & Astrophysics, University of Toronto, 50 St. George Street Toronto, ON M5S 3H4, Canada*
[12]*Department of Physics, University of Toronto, 60 St. George Street, Toronto, ON M5S 1A7, Canada*
[13]*Max-Planck-Institut für Radioastronomie, Auf dem Hügel 69, Bonn, D-53121, Germany*
[14]*Leiden Observatory, Leiden University, PO Box 9513, NL-2300 RA Leiden, the Netherlands*

29 October 2010

ABSTRACT

We present a joint analysis of the overlapping BLAST 250, 350, 500 μm, and Large APEX Bolometer Camera 870 μm observations (from the LESS survey) of the Extended Chandra Deep Field South. Out to $z \sim 3$, the BLAST filters sample near the peak wavelength of thermal far-infrared (FIR) emission from galaxies (rest-frame wavelengths $\sim$ 60–200 μm), primarily produced by dust heated through absorption in star-forming clouds. However, identifying counterparts to individual BLAST peaks is very challenging, given the large beams (FWHM 36–60 arcsec). In contrast, the ground-based 870 μm observations have a significantly smaller 19 arcsec FWHM beam, and are sensitive to higher redshifts ($z \sim$ 1–5, and potentially beyond) due to the more favourable negative K-correction. We use the LESS data, as well as deep *Spitzer* and VLA imaging, to identify 118 individual sources that produce significant emission in the BLAST bands. We characterize the temperatures and FIR luminosities for a subset of 69 sources which have well-measured submm SEDs and redshift measurements out to $z \sim 3$. For flux-limited sub-samples in each BLAST band, and a dust emissivity index $\beta = 2.0$, we find a median temperature $T = 30$ K (all bands) as well as median redshifts: $z = 1.1$ (interquartile range 0.2–1.9) for $S_{250} > 40$ mJy; $z = 1.3$ (interquartile range 0.6–2.1) for $S_{350} > 30$ mJy; and $z = 1.6$ (interquartile range 1.3–2.3) for $S_{500} > 20$ mJy. Taking into account the selection effects for our survey (a bias toward detecting lower-temperature galaxies), we find no evidence for evolution in the local FIR-temperature correlation out to $z \sim 2.5$. Comparing with star-forming galaxy SED templates, about 8% of our sample appears to exhibit significant excesses in the radio and/or mid-IR, consistent with those sources harbouring an AGN. Since our statistical approach differs from most previous studies of submm galaxies, we describe the following techniques in two appendices: our 'matched filter' for identifying sources in the presence of point-source confusion; and our approach for identifying counterparts using likelihood ratios. This study is a direct precursor to future joint far-infrared/submm surveys, for which we outline a potential identification and SED measurement strategy.

1 INTRODUCTION

Observations in the submillimetre (submm) wavelength band (defined here to be 200–1000 μm) are ideal for detecting light from massive star-forming galaxies out to cosmological distances. It has been known since the all-sky *Infrared Astronomical Satellite (IRAS)* survey of the 1980's that such sources contain significant amounts of dust, so that the ultra-violet (UV) light of newly-formed stars is absorbed by the galaxies' interstellar medium (ISM) (Sanders & Mirabel 1996). The dust is typically heated to tens of Kelvin, and most of the light is then thermally re-radiated at far-infrared (FIR) wavelengths (∼60–200 μm). In the submm, the thermal spectral energy distribution (SED) drops off steeply, so that there is a progressively stronger negative K-correction with increasing observing wavelength. The correction is so strong that near ∼1 mm the observed flux density for a galaxy of fixed luminosity is approximately constant from $1 \lesssim z \lesssim 10$ (Blain et al. 2002).

Even though much of the submm band is obscured to ground-based observations by atmospheric water vapour, a number of surveys over the last decade have exploited transparency in several spectral windows to successfully locate high-redshift ($z > 1$) dusty star-forming galaxies solely through their submm emission (submillimetre galaxies, or SMGs). Their discovery was first made with the Submillimetre Common User Bolometer Array (SCUBA Holland et al. 1999) at 850 μm (e.g., Smail et al. 1997; Hughes et al. 1998; Barger et al. 1998; Cowie et al. 2002; Scott et al. 2002; Borys et al. 2003; Webb et al. 2003; Coppin et al. 2006). Several other instruments confirmed their existence in the slightly more transparent 1.1–1.2 mm band (e.g., Greve et al. 2004; Laurent et al. 2005; Scott et al. 2008; Perera et al. 2008; Austermann et al. 2010). These ground-based surveys at 850–1200 μm typically cover $\ll 1\,\mathrm{deg}^2$, and detect several tens of sources per field. The typical angular resolution of these surveys is in the range ∼9–20 arcsec full-width at half-maximum (FWHM). It is worth noting that observations at 350 and 450 μm have also been attempted from the ground (e.g., Smail et al. 1997; Hughes et al. 1998; Fox et al. 2002; Kovács et al. 2006; Khan et al. 2007; Coppin et al. 2008). However, this wavelength range is much more difficult, due to increased atmospheric opacity, so that these surveys have only detected a handful of sources.

While the first generation surveys successfully demonstrated the existence of these ultra-luminous infrared galaxies (ULIRGs) at $z \sim 1.5$–4 (e.g Chapman et al. 2003; Aretxaga et al. 2003; Chapman et al. 2005), sample sizes have been modest (typically $\ll$ 100 sources in a given field). Most of what is known about SMGs is based on cross-identifications with sources in higher-resolution data, particularly in the radio (primarily 1.4 GHz Very Large Array maps, e.g., Smail et al. 2000; Ivison et al. 2007) and in the mid-IR (such as 24 μm *Spitzer* maps, e.g., Ivison et al. 2004; Pope et al. 2006). While these counterpart identification strategies could be biased toward lower redshifts due to the *positive* K-corrections in the radio/mid-IR, more observationally time-consuming mm-wavelength interferometric observations (e.g., Lutz et al. 2001; Dannerbauer et al. 2004; Iono et al. 2006; Younger et al. 2007) demonstrate reasonable correspondence with proposed radio/mid-IR counterparts for a handful of sources. With accurate positions it is then possible to identify optical counterparts, although they are usually extremely faint due to obscuration by the same dust that makes them bright in the submm–FIR, and the fact that stellar light from the most distant objects gets red-shifted out of the optical bands into the near-IR. Obviously, ground-based optical spectroscopy is even more challenging given the difficulty in imaging the counterparts.

Recent observations by the 1.8-m Balloon-borne Large Aperture Submillimeter Telescope (BLAST) at 250, 350, 500 μm (a pathfinder for *Herschel*/SPIRE, Pascale et al. 2008) toward the Extended Chandra Deep Field South (ECDF-S) have provided the first confusion-limited submm maps at these wavelengths which cover areas larger than $1\,\mathrm{deg}^2$. These bands were chosen to bracket the peak rest-frame FIR emission from the SMG population at $z \sim 1$–4. However, given the size of its primary mirror, the BLAST diffraction-limited angular resolution of 36–60 arcsec FWHM at 250–500 μm has made associations between submm emission peaks and individual sources at other wavelengths considerably more challenging than with the existing ground-based surveys at longer wavelengths. For this reason many of the primary BLAST scientific results to date have been derived from the statistics of brightness fluctuations for entire maps, such as the number counts (Devlin et al. 2009; Patanchon et al. 2009), contributions of known sources to the Cosmic Infrared Background (CIB Puget et al. 1996; Fixsen et al. 1998) in the BLAST bands (Devlin et al. 2009; Marsden et al. 2009; Pascale et al. 2009), evolution in the FIR–radio correlation (Ivison et al. 2010), and the large-scale clustering of infrared-bright galaxies (Viero et al. 2009). We emphasize that *none of these results depend on identifying individual submm sources in the BLAST maps.*

More traditional analyses of BLAST sources identified through peaks in maps convolved with the point spread function (PSF) have also been attempted (Dye et al. 2009; Dunlop et al. 2010; Ivison et al. 2010). In general, it has been a struggle to determine whether these peaks are produced primarily by single galaxies, or blends of several faint sources, necessitating either: conservative cuts in the signal-to-noise ratio (SNR) to consider only the very brightest sources; or a careful (though subjective) comparison of all the multi-wavelength data on a case-by-case basis to decide whether single or multiple objects are the likely source of the submm emission. In these earlier papers, Poisson chance alignment 'P' probabilities (Downes et al. 1986) have been used to rank potential counterparts to the BLAST peaks from external matching catalogues, showing that 10% spurious threshold probabilities must be adopted to obtain reasonable source statistics (unlike the more conservative 5% that is typical in the submm community). These methods yield limited results for these wide-area BLAST maps, despite the fact that the SNR of the individual peaks rival those of most previous ground-based observations.

In this paper, driven by the apparent inadequacy of existing methods for studying individual sources in the low-resolution BLAST maps, we develop improved approaches for: (i) filtering confused maps to find emission peaks that are more likely to be produced by individual (or at least a small number of) sources; and (ii) identifying counterparts to these peaks in external matching catalogues using Likelihood Ratios (LR), a method which can incorporate more prior information than that assumed in the calculation of

P. In addition to deep BLAST observations of the ECDF-S, we also make extensive use of the deepest wide-area submm map at ∼1 mm to date: the Large APEX Bolometer Camera (LABOCA) ECDFS Submm Survey (LESS) at 870 μm (Weiss et al. 2009), taken with the 12 m APEX telescope (Güsten et al. 2006). This first detailed comparison between BLAST and longer-wavelength ground-based submm data helps in two key ways. First, the LABOCA beam has a 19 arcsec FWHM (roughly half that of the 250 μm BLAST beam), enabling us to ascertain *directly* whether some of the BLAST peaks resolve into multiple submm counterparts. Second, like SCUBA, LABOCA (Siringo et al. 2009) is more sensitive to $z > 1$ sources than BLAST, and the most distant sources ($z > 4$, e.g., Coppin et al. 2009) are expected to be LABOCA-detected BLAST-dropouts. Therefore this study will offer superior constraints on the high-redshift submm galaxy population than earlier BLAST studies.

Now that we have entered the era of *Herschel* surveys, we also show that these techniques will be useful, despite the approximately twofold improvement in angular resolution offered by SPIRE compared to BLAST. We explore this issue using simulations of SPIRE maps using the smaller PSFs. While we find that the situation is certainly improved for SPIRE, confusion will continue to seriously hamper the interpretation of these new surveys.

The analysis is organized as follows. In Section 2.1 we summarize our treatment of the submm data using our new 'matched filter' to identify individual peaks (full details are given in Appendix A). We produce an external matching catalogue in Section 2.2 combining 24 μm mid-IR and 1.4 GHz radio priors to select sources from a deep *Spitzer* IRAC near-IR catalogue. The LR identification technique is summarized in Section 3.1 (a full development, and calculation of priors are given in Appendix B), and it is used to produce a list of potential matches to the submm peaks in Section 3.2. Also, for cases where matches in the catalogue could not be identified, we search for counterparts in the higher-resolution LESS 870 μm peak catalogue. At this stage we have a collection of submm peaks, and a list of individual galaxies that we believe produce these peaks – in many cases blends of several galaxies. To establish their submm flux densities we fit PSFs at all of their locations simultaneously, in each of the submm maps, in Section 4.1. The effects of confusion, missing identifications, and clustering are explored in Sections 4.2–4.4 using simulations. We derive redshifts for the proposed counterparts in Section 5.1, and study the rest-frame properties of the sample in Section 5.2, showing in particular how confusion may have biased some of the earlier BLAST results. Finally, in Section 5.3 we simulate SPIRE data to demonstrate the usefulness of our techniques for these new surveys.

2 DATA

2.1 Submillimetre Data

2.1.1 BLAST

In 2006 BLAST conducted a two-tiered nested survey centred over the Great Observatories Origins Deep Surveys South (GOODS-S): BLAST GOODS-South Wide (BGS-Wide) over 10 $\deg^2$ to instrumental RMS depths 36, 31 and 20 mJy, at 250, 350 and 500 μm, respectively; and BLAST GOODS-South Deep (BGS-Deep) over 0.9 $\deg^2$ to RMS depths 11, 9 and 6 mJy. It is important to note that a significant additional contribution to the noise in these maps is produced by point source confusion, estimated to be 21, 17 and 15 mJy in the three bands (Marsden et al. 2009). The ECDF-S is completely encompassed by the BGS-Deep coverage. The BLAST maps were produced using SANEPIC (Patanchon et al. 2008), and were filtered to suppress residual noise on scales larger than approximately 10 arcmin (the array footprint). The BLAST beams have FWHM 36, 42, and 60 arcsec at 250, 350, and 500 μm. The maps and data reduction are discussed in detail in Devlin et al. (2009). Details on instrument performance and calibration are provided in Pascale et al. (2008); Truch et al. (2009).

2.1.2 LESS

The LABOCA Survey of the Extended Chandra Deep Field South (LESS, Weiss et al. 2009) provides deep 870 μm data, with an RMS better than 1.2 mJy across the full 30 arcmin × 30 arcmin ECDFS. A combination of time-domain filtering of the raw bolometer data, as well as the suppression of residual noise on scales $\gtrsim$ 90 arcsec were incorporated as part of the reduction procedure. Similar to the BLAST data, this map was then smoothed with the 19 arcsec FWHM diffraction-limited PSF to identify 126 point sources in Weiss et al. (2009) above a significance of 3.7σ (equivalent to a false detection rate of $< 5\%$).

2.1.3 Submm Peak Catalogues

It is standard practice in the submm community to find sources in maps by cross-correlating with the PSF (this strategy was used both in earlier analyses of BLAST data and the LESS 870 μm map as noted above). This operation is optimal for the case of an isolated point source in a field of statistically un-correlated noise: the cross-correlation gives the maximum-likelihood flux density of a point source fit to every position in the map.[1] However, sources are *not* isolated in the real submm maps under discussion. Their high surface density, combined with the large beams, practically ensures that every pixel in these maps has at least some contribution from multiple overlapping sources. This "confusion noise", $N_{\rm c}$, is independent of the approximately white instrumental noise, $N_{\rm w}$. Confusion noise must be considered when asking the question: what is the flux density of a *particular* point source at an arbitrary location on the sky? One can think of $N_{\rm c}$ as the distribution of flux densities in a map with no instrumental noise source (i.e. a map of point sources smoothed by the PSF), precisely the distribution that is modelled in a $P(D)$ analysis. As shown in Patanchon et al. (2009) for BLAST, this distribution is asymmetric, with a positive tail that converges to the underlying differential counts distribution at large flux densities (since brighter sources have a lower surface density, and therefore stand out more against the confusion of fainter sources). For the remainder of this paper, both $\sigma_{\rm w}$ and $\sigma_{\rm c}$ will refer to the

[1] This procedure has long been understood in astronomical data analysis in other wavebands, e.g., Stetson (1987).

RMS of the respective noise distributions, where the former is an output of the map-making process, and the latter is estimated from simulated maps with no instrumental noise added.

The previously published BLAST PSF-smoothed maps lie in a regime where $\sigma_{\rm w}$ is about a factor of two smaller than confusion noise, $\sigma_{\rm c}$. In contrast, for LESS the two noise components are roughly equal.[2] Since confusion is a source of noise that is *correlated on the scale of the PSF*, we have investigated a modified filter for identifying peaks. If one imagines the extreme opposite case of that used to motivate cross-correlation with the PSF – that there is no instrumental noise in the image whatsoever, and so the only signal is the confused pattern of many overlapping sources, clearly any additional smoothing will only make matters worse. In this extreme case, one must clearly bin the data into a finely-sampled grid and simply identify peaks without any filtering that might further degrade the resolution — or alternatively attempt to *de*-convolve the PSF.

We approach this problem by developing a 'matched filter' that maximizes the SNR of individual point sources in the presence of the two noise components. The resulting filter in each band can be thought of as an optimal balance between smoothing and de-convolving the PSF, depending on the relative sizes of the white and confusion noise components. We cross-correlate the raw submm maps with these new filters, and produce source lists from peaks in the resulting SNR maps. A detailed description of our matched filter is given in Appendix A, with Fig. A1 comparing the matched filter with the PSF at 500 μm.

How much does this filter improve the SNR at each wavelength? To address this question we turn to simulations, drawing point source flux densities from the best-fit number counts measured in each band (from Patanchon et al. (2009) and Weiss et al. (2009) for BLAST and LESS respectively), distributing them uniformly in maps, smoothing the maps with the respective PSFs, adding instrumental white noise to match the levels reported for the real observations, and finally subtracting the map means. We then compare the relative sizes of confusion ($\sigma_{\rm c}$), white ($\sigma_{\rm w}$) and combined ($\sigma_{\rm t} \equiv \sqrt{\sigma_{\rm c}^2 + \sigma_{\rm w}^2}$) noise components in: (i) the raw un-smoothed maps; (ii) maps smoothed by the PSFs; and (iii) maps smoothed by the matched filters. The results are summarized in Table 1, and in Fig. 1 a sample portion of the ECDF-S is compared in all four submm bands with no filtering, matched filtering, and PSF filtering.

We find that the point-source sensitivities in the match-filtered BLAST maps improve by ∼15–20% over those reported for the PSF smoothed maps in Devlin et al. (2009) (comparing the bold-face $\sigma_{\rm t}$ columns for the PSF and Matched Filter in Table 1). However, the increase in the LESS point-source sensitivities, ∼ 5%, is not as significant due to the relatively smaller contribution of confusion.

Finally, we produce catalogues of submm peaks for which we will attempt to identify the source(s) of submm emission. Given the marginal improvement in the 870 μm map using the new filter, and for the sake of simplicity, we use the full 870 μm LESS catalogue from Weiss et al. (2009) (down to a SNR of 3.7σ). However, we construct new 3.75σ peak lists for BLAST (relative to instrumental noise) from the match-filtered maps (all submm catalogues are provided in Appendix C).[3] These thresholds ensure that the peaks are likely to be caused by submm emission rather than spurious instrumental noise; such cuts typically result in false-identification rates (the probability that the underlying flux density within an instrument beam at that location is negative) of order 5% (e.g., Coppin et al. 2006; Perera et al. 2008; Weiss et al. 2009). In total, within the region of overlap, there are 64 peaks at 250 μm, 67 peaks at 350 μm, 55 peaks at 500 μm, and 81 peaks at 870 μm. We emphasize, at this stage, that we do not know whether they are produced primarily by one, or multiple overlapping sources. We will will explore the properties of peaks selected this way using simulations in Section 4.

Table 1. Comparison of confusion ($\sigma_{\rm c}$), white ($\sigma_{\rm w}$) and total ($\sigma_{\rm t}$) noise contributions in the raw submm maps, maps cross-correlated with the full PSF, and maps cross-correlated with the matched filter which compensates for confusion. Each quantity was estimated using simulations based on un-clustered realizations of sources drawn from the measured number counts distributions of Patanchon et al. (2009) and Weiss et al. (2009), for BLAST and LESS respectively. All noise values are standard deviations in mJy. Note that our definition of confusion noise here is simply the RMS of a noise-free map containing point sources only. This calculation shows that white noise is more effectively suppressed by PSF filtering than matched filtering. However, the confusion noise is significantly larger in the PSF filtered maps than the match filtered maps. For this reason the *total* noise in the match filtered maps is smaller.

λ	Raw			PSF			Matched Filter		
(μm)	$\sigma_{\rm c}$	$\sigma_{\rm w}$	$\sigma_{\rm t}$	$\sigma_{\rm c}$	$\sigma_{\rm w}$	$\sigma_{\rm t}$	$\sigma_{\rm c}$	$\sigma_{\rm w}$	$\sigma_{\rm t}$
250	14.5	31.2	**34.4**	21.9	11.5	**24.7**	14.6	13.8	**20.1**
350	12.5	28.5	**31.1**	17.3	8.90	**19.5**	13.0	10.7	**16.8**
500	11.6	27.4	**29.8**	16.1	6.70	**17.4**	11.7	8.30	**14.3**
870	0.70	2.00	**2.12**	0.97	0.84	**1.28**	0.82	0.90	**1.22**

2.2 Matching Catalogue

The ideal matching catalogue for our lists of submm peaks would contain *all* of the sources that emit significantly in the submm, without having any spurious interlopers. The starting point for our catalogue is IRAC data from SIMPLE (*Spitzer* IRAC/MUSYC Public Legacy in ECDF-S, Gawiser et al. 2006). This sample is approximately flux-limited with $S_{3.6\mu{\rm m}} \gtrsim 5\,\mu$Jy and $S_{4.5\mu{\rm m}} \gtrsim 5\,\mu$Jy (although there is significant scatter at the faint end, presumably due to noise and completeness effects). Anecdotally, such deep near-IR catalogues appear to contain counterparts to some of the faintest and highest-redshift submm sources detected in ground-based surveys (e.g., Pope et al. 2006; Chapin et al. 2009; Coppin et al. 2009). However, the high surface densities, in this case 48.3 arcmin^{-2} for the ECDF-S, make it impossible to directly associate individual sources with the much

[2] For BLAST the ratios of confusion RMS to instrumental noise in the PSF-smoothed maps are 1.9, 1.9, and 2.4 at 250, 350, and 500 μm. For the LESS PSF-smoothed map the ratio is 1.15.

[3] The new BLAST GOODS-S match-filtered maps and peak lists are available at `http://blastexperiment.info/`.

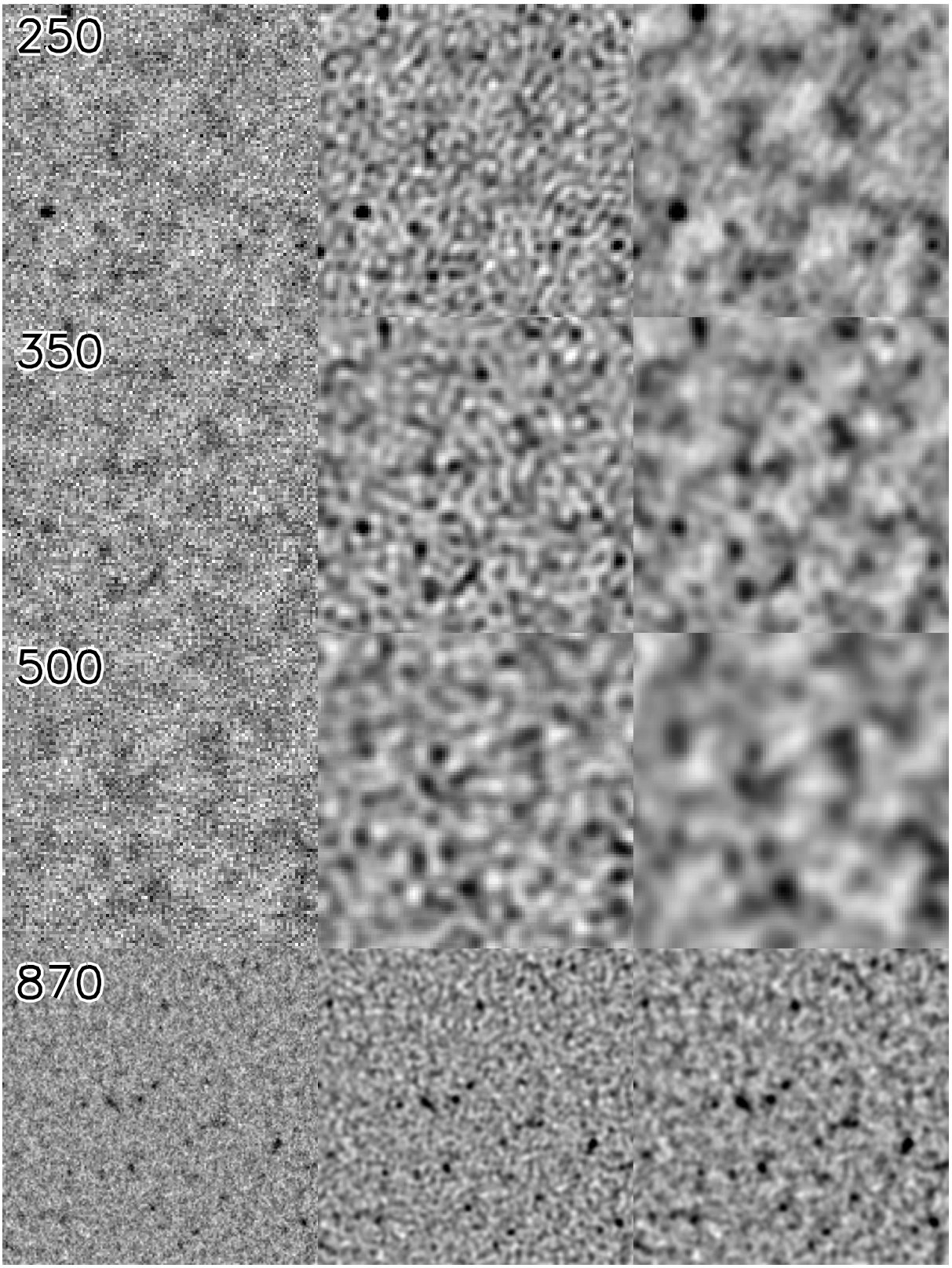

Figure 1. Comparison of maps at all four wavelengths (rows), and smoothing scales in a 0.3 deg × 0.3 deg patch of the ECDF-S. The first column shows un-smoothed maps (noisy, but diffraction-limited resolution), the second column maps smoothed by the matched filter (greatly improved SNR at the expense of a slight degradation in the resolution), and the last column maps smoothed by the PSF (less improvement in the SNR, and resolution degraded by $\sqrt{2}$). The greyscales indicate the significance of point-source flux densities in the maps, ranging from $-3\,\sigma$ (white) to $+4\,\sigma$ (black), considering both the instrumental and confusion noise contributions to each pixel (estimated from simulations – see boldface values in Table 1).

lower-resolution submm peaks. For this reason it is generally necessary to use other priors to cull known spurious sources (such as stars, or galaxies with little or no dust). Fortunately, in this field there also exist deep 24 μm *Spitzer* and 1.4 GHz VLA maps. These two wavelength regimes have been used considerably in the past to identify submm sources as they are sensitive to the presence of dust and star-formation activity, respectively. We check for emission in these additional data sets to reduce the 33962 sources from SIMPLE covering the 703 arcmin^2 region of overlap (Fig. 2), to a total of 9216 entries, a surface density of 13.1 arcmin^{-2}. There are 8833 sources detected at 24 μm, 1659 at 1.4 GHz, and 1276 at both 24 μm and 1.4 GHz.

In Sections 2.2.1 and 2.2.2 we describe our treatment of the mid-IR and radio data, respectively. Then, in addition to the previous plausibility arguments, we use stacking to check directly whether our combined catalogue reproduces the diffuse measurements of the CIB, and hence determine how complete it is in the four submm bands under consideration in Section 2.2.3.

2.2.1 FIDEL

A deep Multiband Imaging Photometer for Spitzer (MIPS) 24 and 70 μm catalogue was produced by Magnelli et al. (2009), combining *Spitzer* data from GOODS-S with the Far-Infrared Deep Extragalactic Legacy survey (FIDEL, P.I. Mark Dickinson). The PSFs have FWHM 5.5 arcsec and 16 arcsec, in each band respectively. The catalogue uses SIMPLE as a positional prior enabling de-blending of sources down to separations as small as 0.5 times the MIPS FWHM. This catalogue is the same that was used for other recent BLAST studies in ECDF-S (Devlin et al. 2009; Dye et al. 2009; Marsden et al. 2009; Pascale et al. 2009), and is consistent with producing the entire CIB across the BLAST bands. This catalogue is also used in the LESS identification paper (Biggs et al. submitted), although it is known that such catalogues do not reproduce the entire CIB at wavelengths approaching $\sim$ 1 mm (Wang et al. 2006; Pope 2007; Marsden et al. 2009).

2.2.2 Radio

The VLA 1.4 GHz data are from the survey of Miller et al. (2008). Given the low elevation of this southern field, and observing from the VLA in the north, the synthesized beam is significantly elongated with dimensions 2.8 arcsec × 1.7 arcsec. We use a new radio catalogue produced by Biggs et al. (submitted) that was developed to identify counterparts to LESS sources. An initial catalogue of 3 σ peaks in the map is produced, and then Gaussians are fit at each of those positions, allowing the sizes to vary. Since this fit is particularly noisy at the faint end, we cull sources with integrated flux densities that are less significant than 2 σ. Finally, we only include sources that lie within 2 arcsec of the IRAC positions. This strategy enables us to go significantly deeper than the published 7 σ catalogue from Miller et al. (2008), or the 5 σ catalogue from Dye et al. (2009), at the expense of missing a handful of brighter radio sources that do not appear to have IRAC associations. Since Monte Carlo simulations based on the submm data and matching catalogue are used in Section 3.2 to calculate the probability that individual counterparts are real, any spurious radio sources near the detection threshold will simply reduce the identification efficiency (see also Fig. B3). Finally, we note that Biggs et al. (submitted) also find identifications for LESS sources using a combination of the radio, MIPS, and IRAC catalogues, although the IRAC data are not explicitly used as a prior for the radio positions.

2.2.3 Stacks

We use the method of Marsden et al. (2009) to measure the submm surface brightnesses of the complete SIMPLE catalogue, as well as the 24 μm (FIDEL), 1.4 GHz (VLA), and combined 24 μm and 1.4 GHz (FIDEL+VLA) subsets of SIMPLE in Table 2. These values are compared to the absolute measurements of Fixsen et al. (1998).

First, we find that the stack on the *complete* (and very high-surface density) SIMPLE catalogue results in lower values than the lower-surface density FIDEL and FIDEL+VLA catalogues. Even though we know that this IRAC catalogue contains sources that are not strong submm emitters (e.g., stars), following the arguments in Section 3.1 of Marsden et al. (2009) we would not expect these extraneous sources to bias the result unless they were somehow correlated on the sky (they are simply an additional source of noise). Therefore, we believe that this peculiar result simply demonstrates the presence of an un-characterized systematic in the SIMPLE spatial distribution (i.e., they are anti-correlated with submm emission). We note that Marsden et al. (2009) also found unexpected behaviour when stacking on a high-surface density optical catalogue.

Second, we find that stacks on the FIDEL catalogue yield results consistent with those quoted in Marsden et al. (2009) (our values are slightly lower, as expected, because we have not corrected for completeness in FIDEL at faint flux densities as they did). Within the uncertainties, this catalogue is consistent with reproducing the entire CIB at 250–500 μm, but recovers less than half of the CIB at 870 μm, consistent with the previous stacking measurements noted earlier.

Finally, we see that the addition of 1.4 GHz detected, but 24 μm un-detected sources ("VLA only"), to FIDEL systematically increases the value of the stack slightly; i.e. the stack on FIDEL+VLA is greater than the stack on FIDEL by itself. We use this fact as our primary justification for including the additional faint radio sources.

While this catalogue arguably contains the majority of the sources that produce significant submm flux in the BLAST bands, the catalogue is certainly missing a significant portion of the 870 μm emitters. Unfortunately, we do not know whether these missing sources are, on average, the same sources that produce the 870 μm peaks, or fainter sources that do not typically contribute to the brighter peaks. We note that the LESS identification paper, Biggs et al. submitted, also fails to identify counterparts for a number of the 870 μm sources using similar matching data. We will attempt to address the impact of this shortcoming in Section 4.3.

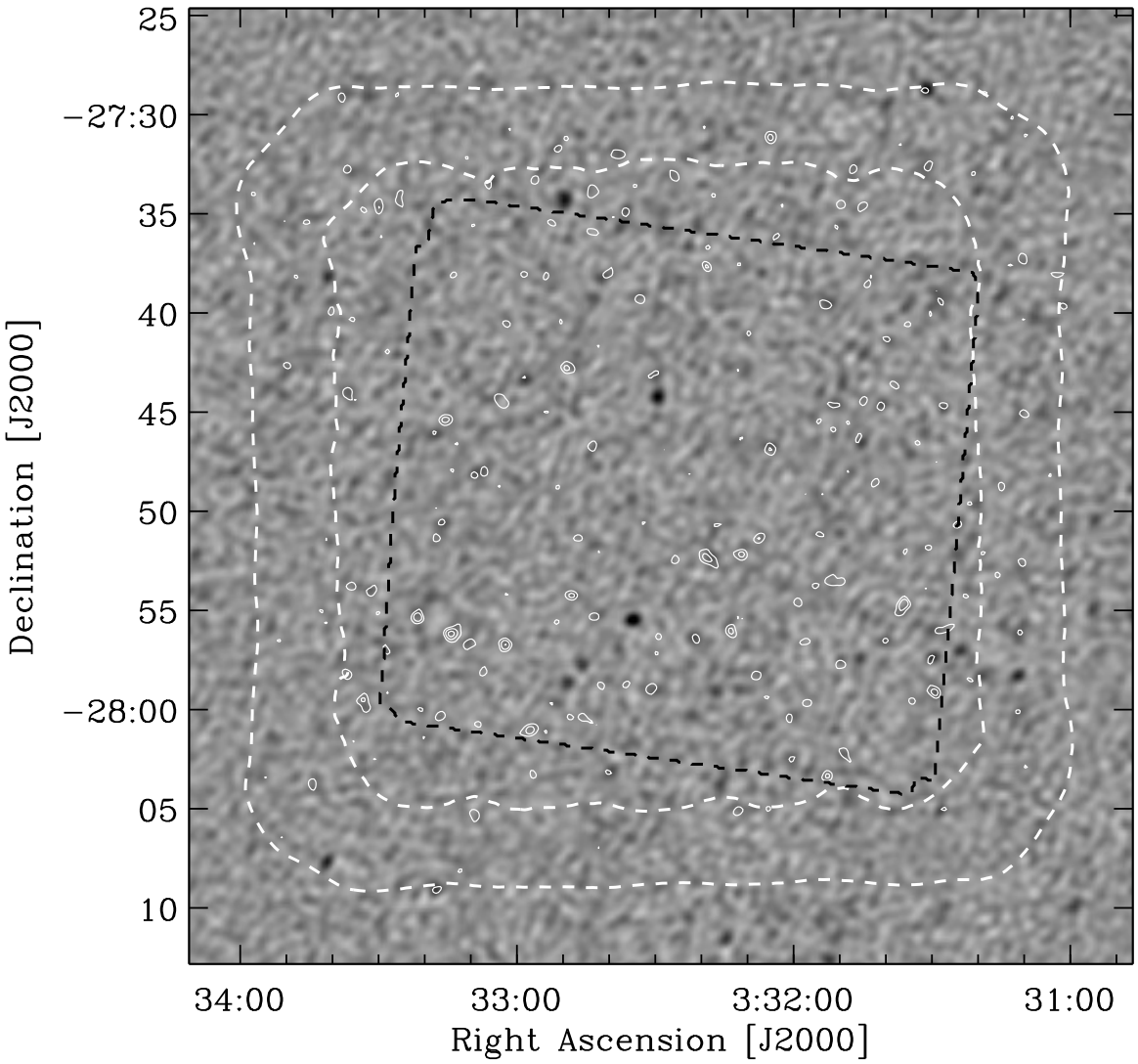

Figure 2. Relative coverage of data sets in ECDF-S. The background greyscale image shows the BLAST 250 μm match-filtered SNR map (this field is completely encompassed by the BGS-deep region described in Devlin et al. 2009), scaled between $-10\,\sigma$ (white) and $+13\,\sigma$ (black). The solid white contours show the LESS SNR map at levels 3, 6 and $10\,\sigma$. The white dashed lines show the LESS 1.3 and 2.2 mJy instrumental noise contours. The dashed black line indicates the 708 arcmin^2 region common to the VLA and FIDEL survey coverage within which we perform out counterpart search. The ECDF-S presently has the best (widest and deepest) submm coverage from 250–870 μm on the sky, with the mid/far-IR and radio data of matching quality required to identify counterparts.

3 CROSS-IDENTIFICATIONS

Given the poor positional uncertainties inherent to the current generation of submillimetre waveband surveys (typically several arcsec), there are usually many potential optical counterparts for each SMG. Thus it has usually been necessary to search for identifications in lower surface density catalogues at radio and mid-IR wavelengths. Also, as mentioned in Section 2.2, emission in these two wavebands are expected to be physically correlated with the submm–FIR emission; there is not a similarly strong correlation for optically-selected sources. The method usually adopted is to estimate 'P' Poisson chance alignment probabilities (Downes et al. 1986) in order to exclude the least likely candidates (although this does not provide a probability that a given source 'is *the* counterpart'). This calculation only uses the source counts of the matching catalogue and an empirically derived maximum search radius. The expected distribution of offsets for true matches is *not* used, except perhaps to set the search radius.

In this paper we take a different approach, using a 'likelihood ratio' (LR) formalism. The basic idea attempts to answer the following question: given a potential counterpart to the submm peak, what is the relative likelihood that it could be a real counterpart given its measured properties (e.g., radial offset, flux density, colour etc.), versus the probability

Table 2. Surface brightnesses resulting from stacks on different catalogues as compared to absolute measurements of the total CIB (values shown in brackets are from Fixsen et al. 1998), in order of decreasing surface density (quoted values in arcmin^{-2}): SIMPLE is the entire IRAC catalogue; FIDEL+VLA includes sources from SIMPLE that exhibit 24 μm emission, and additional VLA 1.4 GHz sources that have a significance $> 2\sigma$ within 2 arcsec of a SIMPLE position; FIDEL is the 24 μm catalogue based on SIMPLE from Magnelli et al. (2009); and VLA is the subset of SIMPLE sources with 1.4 GHz emission that are *not* members of FIDEL. The units of the surface brightness measurements are nW m^{-2} sr^{-1}. The FIDEL+VLA catalogue (indicated in boldface) is used for matching throughout this paper.

Catalogue	Surface Density	250 μm (10.4 ± 2.3)	350 μm (5.4 ± 1.6)	500 μm (2.4 ± 0.6)	870 μm (0.47 ± 0.1)
SIMPLE	48.3	4.33 ± 0.87	3.71 ± 0.51	1.75±0.30	0.13 ± 0.01
FIDEL+VLA	**13.1**	$\mathbf{8.25 \pm 0.46}$	$\mathbf{4.60 \pm 0.27}$	$\mathbf{2.09 \pm 0.16}$	$\mathbf{0.17 \pm 0.01}$
FIDEL	12.6	8.16 ± 0.45	4.56 ± 0.26	2.02 ± 0.16	0.17 ± 0.01
VLA only	0.54	0.35 ± 0.10	0.16 ± 0.06	0.15 ± 0.03	0.004 ± 0.001

that it is a chance interloper (given the background source counts as a function of measured properties)? Versions of this technique have been used in a variety of contexts (e.g., Sutherland & Saunders 1992; Mann et al. 1997; Rutledge et al. 2000). Clearly the LR can explicitly use information such as the expected positional uncertainties, whereas the P calculation does not (although the maximum search radius implicitly incorporates some of this information). It should be noted that, in the past, colour-based priors have been used to cull matching catalogues, and hence reduce the surface density of spurious sources, before finding counterparts using P statistics (e.g Pope et al. 2006; Yun et al. 2008, Biggs et al. submitted). By itself the LR can still only be used to *rank* potential counterparts (similar to the problem with P statistics), but we attempt to establish both the false identification rates, and identification completeness rates for given absolute LR thresholds in each band.

It appears that the reason the LR formalism has not been used for submm identification work in the past is due to its reliance on prior information which historically has been extremely difficult to estimate (see discussion in Serjeant et al. 2003; Clements et al. 2004). With individual surveys covering $\ll 1\,\mathrm{deg}^2$ and having typically fewer than several tens of peaks per field, and very low SNR, the precise positional uncertainty distribution is unknown. However, the BLAST and LESS data, combined with the deep radio and *Spitzer* mid-IR data covering the ECDF-S, enable estimates of priors (such as the radial offset distribution of counterparts) with sufficient precision to produce useful results. Forthcoming *Herschel*, SCUBA-2, and LMT surveys will have better angular resolution, depth, and cover substantially larger areas, so that the methods employed here will also be fruitful (however, note that these future surveys will depend on radio and mid/near-IR data of comparable area and depth for identifying counterparts, and they do not presently exist). In Section 3.1 we summarize the LR method and the priors that we have developed. In Section 3.2 we then use this method to identify a list of potential counterparts from our matching catalogue to the submm peaks.

3.1 Likelihood Ratios and priors

As described in Section 2 we have produced a matching catalogue based on sources from SIMPLE (IRAC) that exhibit either mid-infrared (*Spitzer* MIPS photometry from FIDEL), or VLA 1.4 GHz emission. For the purpose of identifying counterparts we have focussed on three features of this catalogue in addition to positions: 24 μm and 1.4 GHz flux densities (when available) — both of which have commonly been used in the calculation of P values; and the $c \equiv [3.6] - [4.5]$ IRAC colour, which is sensitive to redshift (e.g., Simpson & Eisenhardt 1999; Sawicki 2002; Pope et al. 2006; Yun et al. 2008; Devlin et al. 2009) as it traces the peak of the rest-frame stellar bump.

We fully develop the LR formulae and priors in Appendix B, but provide the main results here. Given the flux densities S (at 24 μm and 1.4 GHz in this case), the IRAC colour c, and the distance r to the jth matching catalogue source from the ith submm peak for which we are searching for a counterpart, we calculate the LR:

$$L_{i,j} = \frac{q(S_j, c_j) e^{-r_{i,j}^2 / 2\sigma^2}}{2\pi\sigma^2 \rho(S_j, c_j)}. \quad (1)$$

Here σ characterizes a radially-symmetric Gaussian positional uncertainty, $q(S, c)$ is the prior distribution for flux densities and colours of matches to submm peaks, and $\rho(S, c)$ is the background source distribution.

All of the priors, σ, $q(S, c)$ and $\rho(S, c)$, have been estimated directly from the data by counting sources in the matching catalogue as a function of each property around submm peak positions (of order ∼60 in each submm band), and comparing to the counts for the entire matching catalogue over the full survey area. We find that sources in the matching catalogue near submm peaks (i.e., potential counterparts): have radial offset distributions that are proportional to the instrumental PSF sizes, as expected; tend to have 24 μm and 1.4 GHz flux densities that are brighter than typical sources in the catalogue; and have redder $[3.6] - [4.6]$ IRAC colours than typical sources in the catalogue, particularly at 500 and 870 μm. We also find that, on average, there are *multiple* extra sources from the matching catalogue near each submm peak, an excess E, of: 3.2 at 250 μm; 3.4 at 350 μm; 3.7 at 500 μm; and 2.2 at 870 μm. This result demonstrates that the submm data are highly confused, but clustering in the matching catalogue may also have an impact.

There could be submm-faint matching catalogue members that cluster around a smaller number of submm-bright sources which produce the observed submm peaks. However, we note that E is strongly correlated with the PSF size; if

Table 3. Summary of the matching catalogue selection function and priors for Likelihood Ratios. Flux cuts for the matching catalogue are only approximate (see Section 2.2). No hard cutoffs are used as priors, there are only weights applied as a function of the distance between the submm peak and proposed counterparts, the 24 μm and 1.4 GHz flux densities, and [3.6] − [4.5] near-IR colours (see Appendix B and Figs. B1-B4)

Catalogue selection	Notes
$S_{24\mu m} \gtrsim 13\,\mu$Jy	*Spitzer*/MIPS, FIDEL (uses SIMPLE IRAC positions as a prior, see below)
	or
$S_{1.4GHz} \gtrsim 20\,\mu$Jy	VLA
	and
$S_{3.6\mu m} \gtrsim 5\,\mu$Jy	*Spitzer*/IRAC, SIMPLE
$S_{4.5\mu m} \gtrsim 5\,\mu$Jy	”
Prior	
$f(r)$	Favour nearby counterparts
$q(S_{24\mu m})$	Favour brighter $S_{24\mu m}$
$q(S_{1.4GHz})$	Favour brighter $S_{1.4GHz}$
$q(c)$	Favour redder [3.6] − [4.5] colour

this clustering scenario were the dominant effect we would expect the same integrated excess regardless of beam size. We will further explore the potential impact of clustering in Section 4.4.

We believe that our excess counting procedure yields a high-SNR measurement of the positional offset distribution, since we need only bin measurements for the submm peaks (in each band) along one coordinate, r, which we then fit with a simple one-parameter model, $f(r) = (r/\sigma_r^2)e^{-r^2/2\sigma_r^2}$. However, there is an implicit assumption that the sources (both in the submm and matching catalogues) are spatially un-clustered. In Table 3 we summarize the matching catalogue selection function, (described in Section 2.2), as well as the basic effect of the priors used in the LR calculation.

Ideally we would bin $q(S, c)$ and $\rho(S, c)$ along all three axes simultaneously (two flux densities and a colour), but in practice this is not feasible given the numbers of submm peaks that we have to work with. We therefore handle the priors *independently*, e.g., estimating $q(S, c) \simeq q(S_{24})q(S_r)q(c)$, and $\rho(S, c) \simeq \rho(S_{24})\rho(S_r)\rho(c)$. This assumption certainly introduces a bias, since in practice these properties are correlated (for example, see Fig. 7 in Dye et al. 2009, showing the correlation between 24 μm and 1.4 GHz flux densities for counterparts to bright BLAST sources). These correlations are simply a reflection of the fact that submm galaxies have a particular range of SED *shapes* (including the radio and near-IR discussed here). We have not attempted to measure these shapes, but an alternative method might consider a range of plausible, physically-motivated SEDs as part of the identification process (e.g. Roseboom et al. 2009). Instead, we have chosen to compensate for the bias by using Monte Carlo simulations to estimate a threshold in the LR that produces a false identification rate of 10%.

We establish the appropriate level by choosing 10,000 random positions in the field, and calculating the LR of matching catalogue sources around those positions. In each submm band we choose a threshold in LR that rejects 90% of the matched sources from this random sample. For convenience, we then calculate normalized LRs for counterparts to submm peaks in each band by dividing the raw LR from Eq. 1 by these thresholds. We therefore only consider potential counterparts to submm peaks those objects for which the normalized LR is greater than 1. While this choice of normalization is arbitrary, the relative LRs for potential counterparts are meaningful (i.e., a LR of 2 indicates double the relative likelihood that it is real compared to a LR of 1). We also estimate that a proposed counterpart with a normalized LR of 1 is about three times more likely to be real than spurious.

Finally, note that the LR only gives the relative chance that a proposed counterpart is real. We have *not* attempted to derive an absolute reliability, R, the probability that a proposed counterpart is correct, as in Sutherland & Saunders (1992), since their formulation assumes that there is a *single* counterpart to each peak (see Appendix B). Instead we rely on our threshold in LR to ensure our spurious fraction of 10% for the ensemble of proposed counterparts.

In summary, while our simplifying assumption that the flux densities and colour are independent of one another is incorrect, we have established a cut on LR that will restrict the number of false positive identifications in the matching catalogue to around 10% (with respect to the number of submm peaks). This idea of setting a threshold to reject unrelated sources is similar to adopting a cut on P, although here we have included more prior information to improve the efficiency. However, we warn the reader that the calibration of the LR and P are both tied to our assumption that clustering in the matching catalogue around submm positions is a negligible effect.

3.2 Potential counterparts

We search for counterparts to all of the submm peaks independently in all four submm bands out to a search radius of 60 arcsec. In practice we could use a much larger search radius, but, since the expected radial probability density, $f(r)$, rolls off to ~ 0 before this radius, even at 500 μm, there is no difference in the list of counterparts with normalized LR > 1 if it is increased. We identify the following numbers of potential counterparts in each band: 52 at 250 μm; 50 at 350 μm; 31 at 500 μm; and 66 at 850 μm.

As noted in the previous section, we expect to encounter several counterparts, on average, for each submm peak. However, with the threshold LR chosen, we only detect a fraction of the total number of counterparts expected: 22% at 250 μm, 19% at 350 μm, 13% at 500 μm, and 32% at 870 μm. It is probably the case that this low identification rate is simply due to the quality of the submm data.

For comparison, we have also identified potential counterparts using P statistics based on the 24 μm and 1.4 GHz flux densities. We counted the numbers of IDs with $P < 0.1$ using both of these sub-catalogues around random positions (as a control, similar to the method employed to normalize the LR), and around submm positions (similar to Fig. 3 in Chapin et al. 2009). We discovered that, while the radio catalogue was well-behaved (a 10% false ID rate was obtained

for random positions), we obtained too many false IDs with the 24 μm catalogue. This result is probably demonstrating that the 24 μm catalogue is slightly clustered. We therefore tuned the cut on P_{24} to 0.08 to obtain the desired 10% rate using random positions. The search radii that we used were $1.5\,\sigma_{\rm r}$ (the single parameter in the radial offset distributions); these search radii are roughly comparable to those adopted in previous studies of BLAST peaks (Dye et al. 2009; Ivison et al. 2010; Dunlop et al. 2010), and encompass approximately 68% of the true counterparts inferred from the excess counting statistics. Using $P_{24} < 0.08$ we would find 45, 31, 12 and 33 potential counterparts, and using $P_{\rm r} < 0.10$ we would find 51, 35, 17 and 44, at 250, 350, 500, and 870 μm, respectively. Clearly there is a significant (although modest) improvement using our LR calculation over P statistics, particularly at the longer wavelengths where the [3.6] − [4.5] IRAC colour is a good discriminator of redshift.

As our goal is to study the properties of BLAST-selected peaks, we identify all of the unique sources from our matching catalogue that potentially produce the observed 250, 350 and 500 μm emission. However, we only consider matches to the LESS peaks that lie within a $2\,\sigma$ search radius of *any* 3.75σ BLAST peak (combining both the BLAST and LABOCA positional uncertainties in quadrature). With this search radius we expect to find 95% of the real matches, and given the surface density of the LESS catalogue, we will have a 10% spurious ID rate (the same as that adopted for the cut on LR). In total, 42 out of the 81 LESS peaks that land within the survey region are associated with BLAST sources, and 36 of them are identified in the matching catalogue using LRs. The remaining 6 LESS peaks are still included as potential matches for BLAST peaks, although they may themselves also be blends of multiple galaxies within the LABOCA beam, and none of them have associated radio, mid- or near-IR flux densities with which to conduct further analysis.

The end result of our matching procedure is a list of 118 unique sources that are believed to contribute to the submm peaks in all four bands (including the 6 that are simply LESS 870 μm sources with no matches at other wavelengths). The coordinates of these sources, and the submm peaks to which they were matched, are given in Table C5. Postage stamps showing the locations of the matches in relation to the submm positions are shown in Fig. D1. For each ID, in addition to the LR, we also provide P values for matches to the 24 μm and 1.4 GHz radio catalogues, using search radii $1.5\sigma_{\rm r}$ (see Table B1).

Note that the third columns in the lists of submm peaks, Tables C1–C4, give references to the individual identifications from the matching catalogue in Table C5 (again, within a $2\,\sigma$ search radius). Since these sources may have been matched to submm peaks in *any* band, the total numbers of counterparts listed here exceed the numbers of matches found independently in each band. In other words, we can now see how the simultaneous observations in the four submm bands have helped one another: 77%, 72%, 76%, and 86% of the 250, 350, 500, and 870 μm peaks have at least one potential counterpart identified. In many cases the same sources appear in several bands, and the higher-resolution observations have enabled counterpart identifications where the lower-resolution observations failed. However, counting the total number of proposed counterparts, we find 64, 65, 59, and 51 sources at 250, 350, 500, and 870 μm[4]. These numbers still fall far short of the total numbers expected, especially in the BLAST bands. We will attempt to quantify the impact of the missing matches in Section 4.3.

4 SUBMILLIMETRE SPECTRAL ENERGY DISTRIBUTIONS

In this section we re-measure the submm flux densities from the combined list (i.e., selected in *any* BLAST band) at the positions of their proposed counterparts in the raw submm maps. Using simulations, we explore the impact of confusion, missing sources, and clustering on these measurements. Finally, we fit these observed-frame SEDs with simple isothermal models, and measure the observed number counts in our catalogue as a function of limiting flux density. Together, these calculations allow us to explore bias and completeness effects for our sample.

4.1 Submm photometry

Under the assumption that the potential counterparts identified in the previous section produce the observed submm emission (and are not simply other galaxies clustered around the submm peaks), we return to the four submm maps and perform simultaneous fits of point sources at all 118 locations to measure their flux densities. This procedure is expected to reduce the Eddington-like bias, or *flux-boosting*, inherent to low-SNR submm surveys (Coppin et al. 2005) in two ways. First, since peaks are initially selected in three different bands, the component of bias introduced by instrumental noise is reduced (as it is independent in each map) — submm peaks preferentially detected on positive noise excursions in one map will not necessarily also land on positive noise excursions in other maps. Second, since we allow for the possibility of *multiple* counterparts to each submm peak (a hypothesis confirmed by the excess counting statistics described in Section B1), the simultaneous fit can, to some extent, de-blend some of the brighter confused sources (confusion itself also contributes to Eddington bias, and unlike the instrumental noise, is correlated between the submm bands).

The fit is performed by modeling the emission of the counterparts as the submm PSFs scaled by their unknown submm flux densities S_i at the locations from the matching catalogue. Under the assumption that the instrumental noise in our submm maps is un-correlated from one map pixel to the next (a reasonable assumption for the raw, un-smoothed maps on the scale of the PSF), there is a simple maximum-likelihood solution for the S_i that takes into account the correlations that arise in cases where multiple sources overlap within a PSF footprint — we follow the derivation provided in Appendix A of Scott et al. (2002). This solution only

[4] Note that at 870 μm 57 matches are indicated, but 6 of those are the LESS sources themselves, leaving 51. We have only searched for counterparts to the 42 LESS peaks that appear to be associated with BLAST peaks, so the average counterparts per peak is actually 51/42=1.21

uses the maps, instrumental noise estimates, and source positions. No preferential weight is given to counterparts with larger LRs, so the noise in the answer only depends on how well the map is fit using our simple parameterization.

A downfall of this approach is that we ignore the additional component of confusion noise from un-identified sources that is correlated on the scale of the PSF. We therefore estimate the total noise by adding the confusion noise for the simulated raw maps from Table 1 to the variances for each source flux density, $\sigma_i^2 = \mathrm{Cov}(S_i, S_i)$. This operation should give good estimates for isolated sources, but we warn that it produces an under-estimate of the variances for the most confused sources. In Section 4.3 we will test the validity of our estimated uncertainties using simulated data sets.

For isolated sources, the recovered flux density is identical to that obtained from the PSF-smoothed map at the location of its counterpart, and its value is un-correlated with the measured flux densities for all other sources in the map. However, for blended sources, the total flux density in the map is divided among the multiple counterparts, and there are non-negligible covariances $\mathrm{Cov}(S_i, S_j)$ for all sources i, j that lie roughly within a FWHM of each other. We therefore evaluate the full expression for the covariances between measured flux densities, i.e., using the off-diagonals of Eq. A11 in Scott et al. (2002).

The individual observed-frame submm SEDs based on these measurements are given in Table C6. We also display the submm SEDs in Fig. E1, along with the 1.4 GHz, MIPS 24 and 70 μm flux densities (when available), and the photometry from the 3.6, 4.5, 5.8 and 8.0 μm IRAC bands (all sources) from the matching catalogue.

4.2 Confusion

Our method assumes that the proposed counterparts to the submm peaks comprise *all* of the galaxies that contribute significant submm emission. However, we have made two fairly arbitrary choices: we select only peaks that have a significance of $3.75\,\sigma$ over the instrumental noise levels; and we only consider sources with a 10% threshold false association rate from the LR analysis. To assess the impact these choices have on the measured flux densities and completeness, we have generated simulated maps drawing sources from the measured number counts in the BLAST bands from Patanchon et al. (2009), and then adding appropriately scaled white noise to mimic the estimated instrumental noise levels.

First, we identify individual peaks in the simulated BLAST maps above the same 3.75σ SNR threshold as for the real data using the same matched filter. Given the sizes of the BLAST beams, and the surface density of the sources, *every* location in the filtered maps has a contribution from multiple submm galaxies (even if they are extremely faint). For each 3.75σ peak we therefore identify *the single* source that makes the *largest* contribution to the observed flux density from the input catalogue at that location — considering the PSFs in each band, input source brightnesses and their distances from the peaks in the filtered maps. In this way a faint source will only be identified provided that it is very close to the submm peak in question, and exceeds the brightnesses of the tails of all the more distant sources in the catalogue. We then re-run this procedure on 100 independent realizations of the maps at each wavelength to fully characterize the scatter in the results. Each time we randomly select a different differential counts distribution from the actual Markov Chains produced from the the $P(D)$ fits in Patanchon et al. (2009).

We find that these brightest sources statistically contribute fractions $0.73^{+0.57}_{-0.57}$, $0.57^{+0.56}_{-0.22}$, and $0.58^{+0.65}_{-0.25}$ (means and 95% confidence intervals) of the peak flux densities in the filtered maps at 250, 350 and 500 μm. Note that the fraction can be greater than one since the simulation is noisy (the source may have landed on a large positive noise excursion). This test shows us that, using a 3.75σ cut, submm peaks are usually a significant blend of two or more individual sources, although there is an incredibly large scatter; a peak may have *many contributors*, but it is also true, in some cases, that a peak is dominated by a single bright source. This result is broadly consistent with a similar set of simulations used by Moncelsi et al. (2010) to correct BLAST peak flux density biases. Also, we have noted that the radial distribution of the brightest sources identified for each submm peak (not shown) broadly resemble the radial distributions estimated for the LR analysis (Eq. B2).

There are numerous obvious examples of blends of sources from the matching catalogue in the real submm maps. We have flagged 42/118 of the most extreme cases with the letter 'C' in Fig. E1 indicating that they are confused to the point that the submm photometry cannot be used reliably, particularly in the BLAST channels. For example, sources 2, 3, 4 and 5 comprise one of the most confused regions of BLAST emission in the entire ECDF-S, as can clearly be seen in the postage stamps (Fig. D1). By comparison, the superior LESS resolution can nearly resolve the entire feature into a string of individual peaks. The inferred flux densities at 250–500 μm therefore have strong *anti-correlations*, since the emission from those four sources must sum to the total integrated flux density of the feature. In fact, the maximum-likelihood solution we have adopted can even allow negative values, a problem which occurs in a number of the most confused examples. The low SNR of the submm maps, combined with confusion from fainter submm sources, and the close proximity of the counterparts, has resulted in flux densities with drastically under-estimated error bars in cases such as sources 2–5. In contrast, sources 61 and 62 are an example where the joint-fit at the positions of two nearby counterparts has recovered plausible flux densities in all the submm bands (this is a low-redshift interacting pair first discussed in Dunlop et al. 2010). In this case, the BLAST SNR is much higher, and the two potential counterparts have sufficient separation to disentangle them.

Next, we investigate the completeness by counting the number of sources above different flux limits in the input catalogue that are recovered in the match-filtered source list (again, considering only the single brightest submm galaxies that contribute to the observed brightness). The recovered percentages are: 50% above 30 mJy, and 90% above 60 mJy at 250 μm; 50% above 15 mJy, and 90% above 45 mJy at 350 μm; and 50% above 10 mJy, and 90% above 25 mJy at 500 μm.

4.3 Missing counterparts

Another significant problem that we face is the issue of missing source matches to the submm peaks. As mentioned in Section 2.2.3, the matching catalogue is probably missing a significant fraction of the 870 μm emitters, and possibly a smaller fraction of the 250–500 μm emitters. More importantly, in Section 3.2 we were not able to identify a large portion of the counterparts to the submm peaks expected in the matching catalogue. Therefore, the measured flux densities for the sources that *were* correctly identified are noisier, and perhaps biased, due to these missing sources in the fitting procedure. We attempted to account for this noise in Section 4.1 by adding the RMS of simulated, instrumental noise-free maps in quadrature to the noise returned from the fitting procedure. Here we will use simulations to estimate how biased and noisy this procedure is.

We use the simulated maps from the previous section that were generated using realizations of sources drawn from the measured counts distributions for the real maps, and assigning them random positions. We now also simulate 870 μm maps using the best-fit counts as reported in Weiss et al. (2009). For each realization we add a random 20% uncertainty to the total number of sources drawn from the distribution to approximate the error indicated in the faintest bin of their cumulative catalogue-based counts.

To approximate the source identification procedure, we first produce 3.75σ peak lists, and then identify the brightest sources from the input catalogue that contributed to each of the peaks. We include as matches only those sources from the input catalogue that contribute more than a threshold fraction of the observed peak, chosen to produce the same average number of matches per peak as we obtained using the real maps and matching catalogue. In this way we associate a range of matches from the input catalogue (with known flux densities) to each observed peak, with a similar surface density of matches as for the real data. However, we stress that this is only a *plausible* simulation, since there is no guarantee that the matches proposed for the real data are in fact the brightest contributors as is the case for this simulation. A significantly more complicated simulation could be undertaken in which we: generate galaxies with full radio–submm–IR SEDs (that are consistent with the true surface densities of sources in each band); create a matching catalogue (i.e., simulating radio, mid- and near-IR catalogues with realistic noise); repeat the process of estimating priors; and finally use LRs to propose matches for each peak. However, we felt that such a simulation was beyond the scope of this paper, and opted instead for the simpler approach that captures most of the necessary ingredients.

With simulated maps, and lists of proposed matches to each peak, we repeat the maximum-likelihood fitting operation of Section 4.1, in all of the submm bands. Since we know the true flux densities for each of the matched sources, $S_{\rm t}$, we are able to directly probe the scatter of the observed flux densities, $R \equiv (S_{\rm t} - S_{\rm o})/\sigma_{\rm o}$, where $S_{\rm o}$ is the inferred flux density, and $\sigma_{\rm o}$ its uncertainty derived from the fitting process (which accounts for instrumental noise and overlap with other nearby sources), and then adding the additional confusion noise for the simulated raw maps from Table 1 in quadrature. The expectation is that this distribution has a mean of zero, and a standard deviation of one. Combining the results for all 100 simulations in each band, we measure the following mean values and standard deviations for R: 0.17 ± 1.23 at 250 μm; 0.19 ± 1.20 at 350 μm; 0.25 ± 1.20 at 500 μm; and -0.05 ± 0.97 at 870 μm.

These results suggest that there is only a small upward bias in the measured flux densities across the BLAST bands, of order $\sigma_{\rm o}/4$, and negligible bias at 870 μm. In absolute terms, we can scale this bias to approximate flux density units by multiplying by the mean values of $\sigma_{\rm o}$ in each band: +3.2 mJy at 250 μm; +3.2 mJy at 350 μm; +3.5 mJy at 500 μm; and −0.05 mJy at 870 μm. We also find that our inclusion of the confusion noise only under-estimates the noise in the BLAST bands by at most ∼23% (as discussed in Section 4.1 our estimate is a lower-limit on the noise for any particular source).

Finally, as noted at the end of Section 2.2.3, our matching catalogue is potentially very incomplete at 870 μm. However, the results of our 870 μm simulation suggest that the missing sources are so faint that they do not contribute significantly to the submm peaks we are analyzing. Again, for this to be true, the sources that *are* in the matching catalogue need to account for the bulk of the brightest 870 μm emitters in the sky.

4.4 The impact of clustering

In addition to the confusion arising from a uniformly distributed population of submm emitters (i.e., chance superpositions of objects at different redshifts, as in Section 4.2), the submm emitters themselves, and/or the matching catalogue, could also be clustered. There are three distinct cases that would affect the results in this paper worth considering:

(i) The low-resolution submm peak could be resolved into multiple components at approximately the same redshift. This is plausible, since it is known that about 10% of SCUBA sources are associated with double radio sources (e.g., Ivison et al. 2002; Chapman et al. 2005; Pope et al. 2006; Ivison et al. 2007), and Väisänen et al. (2010) show that many of their 180 μm-selected sources are blends of multiple galaxies at $z < 0.3$. We also note that a significant clustering signal on angular scales < 1 arcmin has been measured for the LESS catalogue in excess of the Poisson expectation (Weiss et al. 2009).

(ii) The submm peaks could instead be dominated primarily by single matching catalogue sources with a lower surface density, in which case the extra sources counted in the radial excess plots may be spatially correlated, but are not otherwise directly associated with the submm emitter (e.g., galaxies with lower star-formation rates in the same structures).

(iii) Massive foreground structures could enhance the brightnesses of background galaxies through lensing. This scenario would have a similar effect to the previous one; there could be a number of additional foreground galaxies near the positions of submm peaks, even though they do not themselves contribute significantly to the submm flux.

The impact of these clustering scenarios is not easy to assess accurately with simulations because it is simply unknown how *all* galaxy populations cluster throughout the history of the Universe; indeed, this is one of the major outstanding questions in modern Cosmology. While there

are a number of ways to simulate clustered galaxy populations, such as the Halo model (Mo & White 1996) used to fit BLAST data in Viero et al. (2009), or more complicated semi-analytical models (e.g. Baugh et al. 2005), it is beyond the scope of this paper to test the full range of models that are plausible. On the other hand, there is clear evidence that some clustering is required to explain both the BLAST and LESS submm maps. Since we have argued that the bulk of the submm emission is produced by sources in the matching catalogue, a reasonable approach is to incorporate these real, and clustered positions in our simulated maps to see what impact they have.

We repeat the simulations of the previous sections, drawing sources from the measured counts distributions, but now randomly assigning them positions from the real matching catalogue. With this limitation, we can only draw the same number of sources as in the real matching catalogue, so we restrict ourselves to a flux-limited sample that results in the same surface density. We then produce maps, and identify 3.75σ peaks as before.

To assess the relative impact of clustering, we also produce simulations with the same surface density of input sources, but using uniformly distributed positions. In both cases we measure the radial excess counts in the matching catalogue around peaks, with respect to the entire catalogue (as in Figure B1). We find that the clustered simulations yield systematically larger excesses per submm peak, by factors 1.07, 1.02, 1.02, and 1.24 at 250, 350, 500, and 870 µm, respectively. The trend is for this excess to be larger for the *highest-resolution* measurements, which might be expected given the large 2-point correlation measurements from Weiss et al. (2009) growing towards scales < 1 arcmin. However, considering the scatter in the 100 simulations, we also find that the uncertainties in the excess measurements are 21%, 14%, 19%, and 16% in the four bands. In other words, when testing the hypothesis that the difference observed for the clustered simulations are significant compared to the un-clustered simulations, only the excess at 870 µm is marginally significant (a 1.5σ outlier).

However, we warn that our simulation is only testing a particularly weak form of clustering. It is probable that subsets of our matching catalogue have significantly different angular clustering signatures when compared to the catalogue as a whole, and it may be possible to identify them through their redshifts, colours, and brightnesses. If such populations are correlated more, or less strongly with the submm emitters, their may be additional significant biases in our LR approach – effectively cases (ii) and (iii) described above. We note that Chary & Pope (2010) investigate the impact of just such an effect on stacking analyses in this field, although the results depend substantially on their model for the redshift evolution of submm galaxies and their multi-wavelength SEDs.

We note additional support for the hypothesis that clustering has a negligible impact in Section 3.2: the excess matching catalogue counts around submm positions are correlated with the angular resolution of the submm maps. The same integrated excess would be measured, regardless of the PSF shape, if the submm emission were produced by single galaxies.

As a final word on this subject, what would the effect be on our analysis if there *were* significant clustering in the matching catalogue around the submm peaks? In this case the radial excess distributions (Fig. B1), and our measurements of $q(S, c)$ (Figs. B2–B4) would trace the properties of the clustered objects (e.g., spatial extent, colours and brightnesses), rather than the properties of submm sources, and we would end up with many more false positives than the target 10% rate. While we do not believe this is the most likely scenario based on the arguments made in this section, and the fact that the SEDs for the counterparts seem to match models for star-forming galaxies, only higher-resolution studies will be able to settle this issue unambiguously.

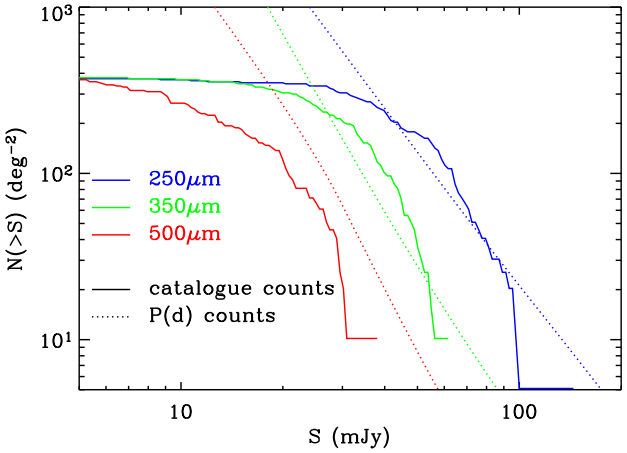

Figure 3. The integral number counts for our sample (solid lines), compared with the total counts inferred from the $P(D)$ analysis of Patanchon et al. (2009) (dotted lines), at 250 (blue), 350 (green) and 500 µm (red).

4.5 Isothermal SED models and number counts

We fit optically-thin isothermal modified blackbody functions (modified blackbodies henceforth), $S_\nu \propto \nu^\beta B_\nu(T)$, to the new submm photometry, and use Monte Carlo simulations to characterize the uncertainties (as described in Section 4 of Chapin et al. 2008). Following the work of Wiebe et al. (2009), who examined the detailed spatially-resolved SEDs of several nearby resolved galaxies observed with BLAST, as well as an earlier study by Klaas et al. (2001) who combined ground-based submm photometry with FIR measurements of ULIRGs, we choose to model the submm emission using an emissivity index of $\beta = 2.0$. The only free parameters are the amplitudes and temperatures (see Table C6 and Fig. E1).

To test the completeness of our catalogue, and also to gauge the degree to which our procedure has dealt with flux boosting in the submm peak catalogues, we compare the integral source counts from our sample (summing the number of sources in the catalogue above a given flux density limit, and dividing by the survey area of 708 arcmin^2) to the total counts inferred from $P(D)$ analysis in Patanchon et al. (2009). Rather than using the submm photometry directly, we use the flux densities from the fitted SED models evaluated in each band. The results of this comparison are shown in Fig. 3. In the 250 and 350 µm channels the catalogue counts slightly exceed the $P(D)$ counts above approximately 30 and 40 mJy, respectively. While this excess shows

there is still some influence from boosting, its effect has been drastically reduced when compared with the individual flux-limited BLAST catalogues (see Fig. 11 in Patanchon et al. 2009). Below these levels the catalogue is clearly incomplete at 250 and 350 μm as the counts rapidly flatten. At 500 μm the catalogue counts have a similar qualitative shape, but lie below the $P(D)$ counts at all flux densities; the completeness is about 66% above 20 mJy. This result is expected given the more limited success we have had in identifying counterparts at 500 μm (see Table B1). Note that these approximate completeness estimates are consistent with the simulations described at the end of Section 4.2.

5 DISCUSSION

5.1 Redshifts

Many of the proposed counterparts have either optical spectroscopic or photometric redshifts in previously published catalogues (Wolf et al. 2004, 2008; Grazian et al. 2006; Brammer et al. 2008; Rowan-Robinson et al. 2008; Taylor et al. 2009). For those counterparts that do not, the IRAC colours may be used as a crude redshift estimator. We use the redshift catalogue from Pascale et al. (2009) which combines the various photometric and spectroscopic redshfts in the literature with the BLAST redshift survey of Eales et al. (2009), and then we add additional redshifts identified in more recent BLAST follow-up studies (Ivison et al. 2010; Dunlop et al. 2010; Casey et al. 2010). In Fig. E1, the redshifts are indicated with 's', 'p' or 'i', indicating spectroscopic, optical photometric, or IRAC-based photometric redshift measurements, respectively. In total, there are 76/118 sources with usable submm photometry. Of those, 69 have redshift estimates: 23 are optical spectroscopic redshifts; 35 are optical photometric redshifts; and 11 are IRAC photometric redshifts. The full list of redshifts that we have adopted is given in Table C6. We warn that the IRAC-based photometric redshifts are highly uncertain on an object-by-object basis, and are biased low for the higher-redshift ($z > 2$) sources (see Fig. 4 in Pascale et al. 2009).

In Fig. 4 we show the redshift distribution for these 69 sources, as well as sub-samples using flux density-limits in each of the BLAST bands corresponding roughly to the flux densities at which the counts begin to turn over significantly in Fig. 3 (as a rough proxy for the point at which completeness begins to drop). The median of the entire distribution is $z = 1.1$ with an interquartile range 0.3–1.9. Note that if we exclude the the IRAC-based photometric redshifts the median of the entire sample increases slightly to $z = 1.3$.

This redshift distribution is qualitatively similar to the deep 250 μm survey of Dunlop et al. (2010) in GOODS-S at the center of the ECDF-S, but shows a significantly greater tail of sources beyond $z = 2$ compared to the shallower survey of Dye et al. (2009). This latter discrepancy is probably due to a combination of increased depth in our submm catalogue, and better completeness in the high-redshift counterpart identifications.

The flux-limited distributions clearly show a trend from low to high redshift with increasing wavelength in Fig. 4: a median $z = 1.1$ with an interquartile range 0.2–1.9 at 250 μm; a median $z = 1.3$ with an interquartile range 0.6–2.1 at 350 μm; and a median $z = 1.6$ with an interquartile range 1.3–2.3 at 500 μm. This trend is consistent with the results from BLAST stacking analyses (Devlin et al. 2009; Marsden et al. 2009; Pascale et al. 2009) which show that the CIB is produced by higher-redshift galaxies with increasing wavelength.

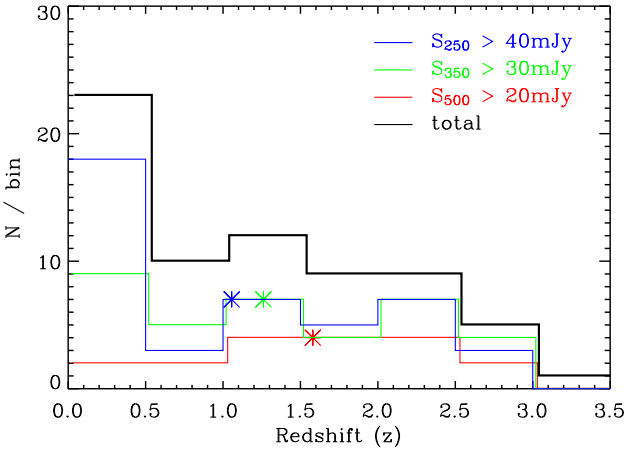

Figure 4. The redshift distribution for the 69 non-confused sources with redshift estimates. Also shown are the redshift distributions for flux-limited sub-samples, $S_{250} > 40$ mJy, $S_{350} > 30$ mJy, and $S_{500} > 20$ mJy, chosen to correspond approximately to where the counts in our catalogues flatten significantly compared to the total population – see Fig. 3. The asterisks indicate the medians of these sub-samples.

With redshift estimates for our proposed counterparts, we are also able to check whether clusters of sources contributing to single submm peaks lie at a single redshift, or at a range of redshifts. If, as we have asserted, most of our submm peaks are chance superpositions of un-related galaxies, we would expect most clumps of proposed counterparts to lie at different redshifts. On the other hand, clusters of proposed counterparts at the same redshift would be consistent with the clustering scenarios described in Section 4.4.

There are cases of what appear to be groups of proposed counterparts to single peaks at different redshifts. See, for example, sources 2–5 in Fig. D1. In this particular case there also appears to be a fifth significant source of emission in most of the submm maps that is not identified, this being west and slightly south of the main clump, perhaps coincident with a faint radio source that lies within the saturated source apparent in the 3.6 μm map. The clump of sources 13–15 is a similar example. Sources 52 and 53 form a more well-separated example, with the former peaking in the 250 μm map, the latter in the 500 μm map, and with a double peak in the 350 μm map. The two optical photometric redshifts appear to be significantly different (0.1 and 0.6, respectively). Some of these sources could also be examples of foreground galaxies lensing background sources, although this effect is more difficult to quantify without accurate spectroscopic redshifts for most of the sample, and lensing models for each case.

There are also examples of peaks that could plausibly be interacting pairs at the same redshift (case (i) from Section 4.2), more along the lines of radio-doubles detected in SCUBA surveys. The clearest example is the low-redshift interacting pair of sources 61 and 62 (also noted in Dunlop

et al. 2010). Some more possible examples are: 74 and 75; 76 and 77; 83 and 85; and 113 and 114.

5.2 Rest-frame SEDs

The SEDs for all 118 sources are shown in Fig. E1. For the 69 sources with redshift estimates and useful photometry, we convert the observed temperatures from the modified blackbody fits of Section 4 to rest-frame temperatures, allowing us to probe the cold dust SEDs of the sample. The distributions of these temperatures for the entire sample, and flux-limited sub-samples in each BLAST band are shown in Fig. 5. The total distribution has a median $T = 29\,\mathrm{K}$ and interquartile range 23–36 K. For reference, re-running the analysis with $\beta = 1.5$ increases the temperatures by about 5 K.

There is almost no variation in the temperatures of the different flux-limited sub-samples: a median $T = 30\,\mathrm{K}$ with an interquartile range 25–39 K at 250 µm; a median $T = 30\,\mathrm{K}$ with an interquartile range 23–35 K at 350 µm; and a median $T = 30\,\mathrm{K}$ with an interquartile range 22–38 K at 500 µm. The reason for this can be seen in the bottom panel of Fig. 5: even though the longer-wavelength channels tend to be biased to selecting higher-redshift (and hence more luminous and warmer) galaxies, the extra galaxies picked up at low redshift (and hence lower luminosity) by the short-wavelength channels are biased toward warmer temperatures in those volumes. We have also checked for biases in the total temperature distribution due to the IRAC-based photometric redshifts, but do not find a significant difference for the $z > 1.5$ galaxy temperatures when sources with these photometric redshifts are excluded.

We infer cold-dust temperatures that are generally *warmer* than the mean temperature of 23.4 K and $1\,\sigma$ width of 5.2 K (also assuming $\beta = 2.0$) reported for the robust, but shallower, BLAST sample in Dye et al. (2009). While this discrepancy may partly be due to the relative depths of the samples, there is also strong evidence that our treatment of confusion and the inclusion of LABOCA 870 µm data have resulted in less-biased temperatures.

The 870 µm data place a firm constraint on the Rayleigh-Jeans part of the SED. Since the longer-wavelength BLAST data are more confused (and hence more biased), there is a systematic preference for shallower spectra, or cooler apparent temperatures. However, the higher-resolution LESS data are less prone to this problem, and therefore greatly improve the fits (if a smooth SED model such as the modified blackbody is assumed). Sources 6, 23, 25, 34, 36, 44, 48, 67, 104, and 118 in Fig. E1 are more extreme examples that show this effect clearly. In all these cases, the SED model is a reasonable fit to the 250, 350, and 870 µm data points, but the 500 µm data lie above the model.

Restricting ourselves to the the 26 galaxies at $z \geqslant 1.5$ with usable submm photometry we find a median temperature of 36 K. This is in good agreement with Fig. 9 from Dunlop et al. (2010) which shows that their S_{250}/S_{870} data are consistent with a $\beta = 1.5$, $T = 40\,\mathrm{K}$ modified blackbody at these same redshifts (remembering that if we had chosen $\beta = 1.5$ instead of 2.0 our temperatures would be larger by about 5 K).

We also fit the star-forming galaxy SED templates of Dale et al. (2001) to the submm and FIR photometry (870–70 µm). Since these provide a fairly restricted range of SED shapes, they are only used to illustrate several basic features in the radio and mid/near-IR SEDs of our sample with respect to the rest-frame FIR peak (i.e., they should not be considered accurate fits beyond the 870–70 µm data). First, they give an indication of the location of the ~ 1.6 µm stellar bump that is redshifted into the IRAC bands for many of our sources (i.e., if the wavelength of the bump in the model corresponds to a local maximum in the IRAC data the redshift estimate is plausible). Also, since these are templates for star-forming galaxies, sources from our sample with large excesses in either the mid-IR or radio may harbour AGN. Of the 69 sources with usable submm photometry and redshifts, 6 clear examples (8%) seem to exhibit such excesses: source 6 (mid-IR excess); source 34 (radio excess); 49 (radio and mid-IR excess); 51 (mid-IR excess); and 52 (radio excess); and 67 (mid-IR excess). For the remaining 42 submm confused sources, we fit the Dale et al. (2001) SED templates to all of non-confused data (VLA and *Spitzer*) to illustrate what plausible values in the submm might be. Finally, we note that some of the sources with IRAC-based photometric redshifts have particularly poor SED fits in the near-IR when compared to these templates, such as sources 33, 46, 50, and 117, as well as particularly cool inferred rest-frame temperatures ($< 20\,\mathrm{K}$). It is quite likely that these photometric redshifts are biased low, resulting in under-estimates of the inferred temperatures, and luminosities.

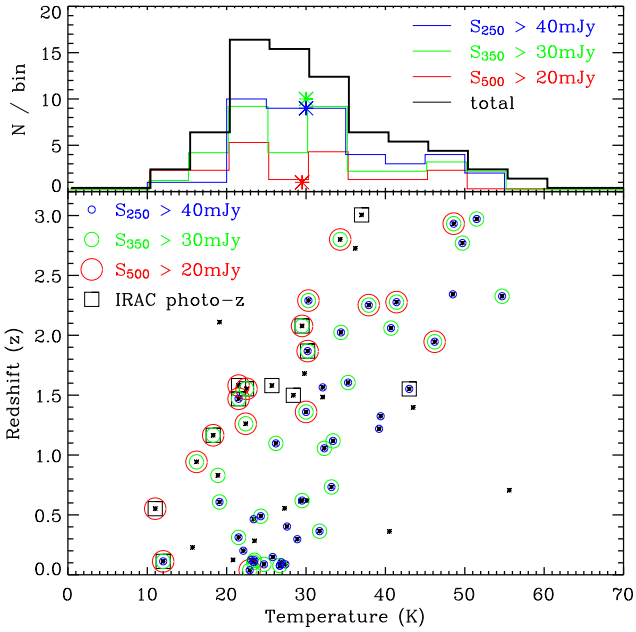

Figure 5. The dust temperature distribution, assuming $S_\nu \propto \nu^{2.0} B_\nu(T)$, for the 69 non-confused sources with redshift estimates. The bottom panel shows redshifts plotted against temperature, and the top panel collapses the redshift axis into a histogram. Similar to Fig. 4 we indicate the distributions for flux-limited sub-samples in each BLAST band, and indicate the medians with asterisks. We indicate the sources with IRAC-based photometric redshifts, as they are highly uncertain, and may be biased low. If these sources are at higher redshifts, they will move up and right in the lower panel. There is a negligible trend in rest-frame temperature for sources selected in different BLAST bands.

Next, we normalize each of the full radio–submm–IR SEDs by their total IR (TIR) 10–1000 μm luminosities using the modified blackbody fits. The sample is then plotted in bins of $L_{\rm TIR}$ in Fig. 6. This strategy minimizes scatter in the region of the SEDs probed by the submm photometry, and enables us to examine trends in the relative radio and mid/near-IR scatter as a function of luminosity. For reference, the same TIR-normalized SED from Dale et al. (2001) (with $\log_{10}(S_{60}/S_{100}) = -0.2$) is also plotted over each luminosity range to highlight differences. In the first instance this figure demonstrates that the vast majority of our proposed multi-wavelength counterparts are plausible: while there are a handful of significant outliers, the relative intensities of the radio and IR emission to the rest-frame FIR peak show reasonable consistency with each other, and with the models. It is clear that the radio–FIR correlation holds for most of the sample since the reference FIR-normalized star-forming galaxy SED has a radio spectrum that passes through most of the VLA data in each luminosity bin, regardless of the wavelength of the FIR peak (consistent with the findings of Ivison et al. 2010). On the other hand, the mid/near-IR SEDs exhibit significantly larger scatter; particularly in the range $11.5 < \log(L) < 12.8$ (a factor of ~ 100 peak-to-peak). Most of the sources mentioned previously with mid-IR excesses land in the two luminosity bins that span this range. While a correlation between AGN activity and FIR luminosity has been observed before (e.g. Takeuchi et al. 2003, 2004; Valiante et al. 2009), it is curious that our most luminous $12.8 < \log(L) < 13.5$ bin exhibits a more compact spread in SED properties consistent with pure star-formation. This result may not be significant, however, since this last luminosity bin has only 10 sources (whereas the next two fainter bins have 26 and 20 sources respectively). Fig. 6 also shows a strong correlation between luminosity and temperature: the least luminous sources peak at wavelengths $\lambda > 100$ μm, while the most luminous sources peak at wavelengths $\lambda < 100$ μm. Finally, this plot shows that the more luminous sources have a greater ratio of FIR luminosity to starlight (the 1.6 μm bump); the lowest-luminosity sources have SEDs more closely resembling normal star-forming galaxies than ULIRGs.

To explore the correlation between luminosity and temperature more fully, and the potential for its redshift evolution, we compare our sample with the local Universe. We use as our reference the distribution in integrated 42.5–122.5 μm FIR luminosity, and $C \equiv \log_{10}(S_{60}/S_{100})$ colour as measured by Chapin et al. (2009) based on *IRAS* data (an updated version of the analysis in Chapman et al. 2003). At redshift ~ 2.5 the entire BLAST 250–500 μm bandpass closely matches the 42.5–122.5 μm coverage from the *IRAS* 60 and 100 μm channels (see Fig. 6 in Chapin et al. 2009), so that tests for evolution at that redshift have only a minimal dependence on the SED model used to fit the data. However, at lower redshifts, the BLAST bandpass samples significantly longer wavelengths in the rest-frame. Since the modified blackbody models used to fit the submm data fall-off much faster in the mid/far-IR than for real galaxies (since the shorter wavelengths sample warmer and/or optically-thick dust), we have fit the submm and FIR data for our sample using the more realistic star-forming galaxy SED templates of Dale et al. (2001). In Fig. 7 we plot the colours and luminosities for our sample using these SED

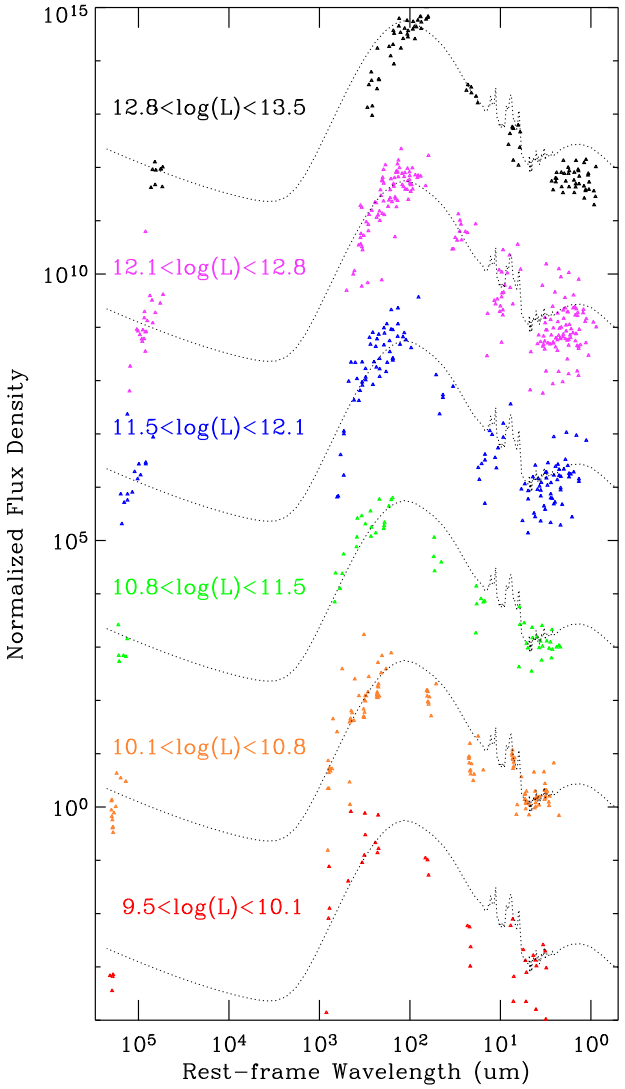

Figure 6. SEDs of the 69 galaxies with non-confused submm photometry and redshift estimates, normalized by the total infrared (TIR) 10–1000 μm luminosities of their modified blackbody fits. The SEDs are plotted in bins of $L_{\rm TIR}$ and offset by multiples of 10^3 for clarity. The SEDs of individual galaxies are shown in Fig. E1. A single $L_{\rm TIR}$-normalized SED template from Dale et al. (2001), for which $\log_{10}(S_{60}/S_{100}) = -0.2$, is shown as a dotted black line for reference in each bin. This comparison highlights several features: more luminous sources peak at shorter wavelengths (they are warmer); the radio-FIR correlation (the normalized model passes through the radio data irrespective of the FIR peak wavelength); the spread in the near/mid-IR SEDs (largest in the bins spanning $11.5 < \log(L) < 12.8$); and an increase in the size of the FIR peak with respect to stellar light (the 1.6 μm bump) with increasing luminosity.

fits. We colour-code the sources by redshift bin: $z < 0.5$ (blue crosses); $0.5 < z < 1.5$ (grey asterisks); $1.5 < z < 2.0$ (green triangles); and $2 < z < 42$ (red squares). Note that there is some quantization along the vertical axis for the sample since there are only 64 SED templates in the library, with colours ranging from about −0.55 to 0.26. Since this range is not quite as broad as that observed for the

real sources, there is also some clipping (mostly problematic for the coolest sources at the bottom of the plot which are simply assigned the template SED with the most negative colour). We then compare this distribution with the local-Universe measurement of Chapin et al. (2009), including the 1σ envelope (solid and dotted black lines respectively).

We find that the temperatures for our sample lie systematically toward cooler (more negative) values than in the local Universe. At low redshifts, the lower temperatures are expected, since the submm bands sample the Rayleigh-Jeans tail of the thermal emission and are therefore biased toward the detection of cooler sources for a given flux-density–limit. Similarly, observations on the shorter-wavelength side of the thermal emission peak (such as with *IRAS*) are biased toward the detection of warmer sources — an effect which was accounted for in Chapin et al. (2009) in order to infer the properties of the entire population. Selection effects alone may therefore explain much of the discrepancy in temperatures seen here, and for 850 μm (e.g., Kovács et al. 2006; Coppin et al. 2008) selected galaxy populations (see also the discussion in Section 4.3 of Dye et al. 2009).

To test this theory, we have used a simple simulation to explore the effects of our selection function on the temperatures and luminosities of galaxies in different redshift slices. We take the local FIR colour-luminosity distribution, $\Phi(L, C)$, from Chapin et al. (2009) and assume that it does not evolve with redshift. We then calculate the total number of objects as a function of L and C in a redshift slice $z_0 < z < z_1$ as $\int_{z_0}^{z_1} \Phi(L, C)(dV/dz)dz$, where dV/dz is the differential volume element, and then use the Dale et al. (2001) SED templates to extrapolate to the BLAST wavelengths, and hence estimate observed flux densities. While the relative numbers of galaxies in different redshift slices will be incorrect, since it is known that significant luminosity and/or density evolution in the local luminosity function is required to fit observed submm number counts (e.g., Rowan-Robinson 2001; Scott et al. 2002; Lagache et al. 2003; Valiante et al. 2009; Rowan-Robinson 2009; Wilman et al. 2010), this calculation should give a good idea of the selection function *within* a redshift slice (provided that evolution across the slice is negligible). We then apply flux density cuts of 40, 30 and 20 mJy at 250, 350, and 500 μm respectively to mimic our observational selection function. We show 90% confidence intervals for these model distributions in the $z < 0.5$ and $2.0 < z < 4.0$ redshift bins with solid blue and red contours in Fig. 7, showing that they extend significantly below the rest-frame colour-luminosity correlation. To illustrate how this selection happens, we show the effect of the BLAST flux limits in the colour-luminosity plane at a single fixed redshift $z = 0.5$ as a thick dashed line (sources at that redshift should only be observable to the right of the limit). The detected galaxies tend to pile-up against this limit, since there are many more galaxies at fainter luminosities than at brighter luminosities in a given volume. If this limit were a vertical line in the plot, we would then expect the observed luminosities and colours to cluster around the rest-frame correlation (solid and dotted lines). However, since the limit is *inclined*, a dis-proportionate number of objects are detected toward the lower-left (lower luminosities, and cooler temperatures). Despite the simplicity of the model, the large noise in the observed sample, and potential for incorrect redshifts, the general trends in the data are clearly reproduced. This result suggests that there is no significant evolution in the correlation between FIR luminosity and temperature at high redshifts, at least for the most luminous ($L_{\rm FIR} \gtrsim 10^{12}\,{\rm L}_{\odot}$) galaxies probed by our sample at $z \gtrsim 1$.

While the lack of evolution in our sample appears to be at odds with the evolution observed in the *stacked* SEDs with redshift described in Pascale et al. (2009), we note that our sample contains only ULIRGs at $z > 1.5$, whereas the stacked SEDs are dominated by significantly fainter galaxies. It is possible that 'normal' star-forming galaxies are generally warmer in the early Universe than in the present-day, while massive starburst galaxies do not differ appreciably. Another possible explanation is simply that the completeness to less luminous (and presumably cooler) galaxies drops off faster at high redshift than it does for the more luminous (and warmer) galaxies in Pascale et al. (2009) — resulting in a bias to warmer stacked temperatures.

Our finding may also have interesting consequences for recent studies which indicate that SMGs are generally more extended and cooler than local ULIRGs. These claims have been made based on a variety of observations, including resolved MERLIN radio morphologies (e.g. Chapman et al. 2004), *Spitzer* MIPS and IRAC SEDs (e.g. Hainline et al. 2009), and *Spitzer* IRS spectra (e.g. Menéndez-Delmestre et al. 2009). Such observations point to a systematic difference in the physical conditions of major-mergers which produce SMGs (e.g., see resolved molecular gas observations and discussion in Tacconi et al. 2008), compared to ULIRGs in the local Universe. We note that Chanial et al. (2007) found a positive FIR luminosity-size correlation with a similar form to the temperature-luminosity correlation that we have used here. It may therefore be the case that the low-temperature bias for submm samples has picked out galaxies that are also more extended.

5.3 Predictions for *Herschel*/SPIRE surveys

Will the techniques described in this paper be useful for the new generation of *Herschel*/SPIRE surveys? To address this question, we have again turned to simulations, creating realizations of sources with flux densities drawn from the BLAST $P(D)$ counts. These sources are assigned uniformly-distributed random positions covering the same area as the ECDF-S observations described in this paper, and then smoothed with the smaller 18, 25, and 36 arcsec FWHM Gaussians to approximate the SPIRE beams. We have chosen a pixel size of 6 arcsec, and added Gaussian noise with RMS 1.8, 2.3, and 5.0 mJy at 250, 350, and 500 μm, respectively. We find that the RMS due purely to point source confusion is 7.0, 6.8, and 6.6 mJy at 250, 350, and 500 μm respectively. This simulation is a reasonable approximation of the SPIRE Science Demonstration Phase observations of GOODS-N, taken as part of the *Herschel* Multi-tiered Extra-galactic Survey (HerMES). Initial number counts were shown to be consistent with the BLAST results in Oliver et al. (2010), and our instrumental and confusion noise estimates are close to those reported in Nguyen et al. (2010). A 0.1 deg × 0.1 deg subset of the simulated 250 μm data are shown in the left panel of Fig. 8.

Next, we produce match-filtered maps, following the prescription of Appendix A. The total noise (combining

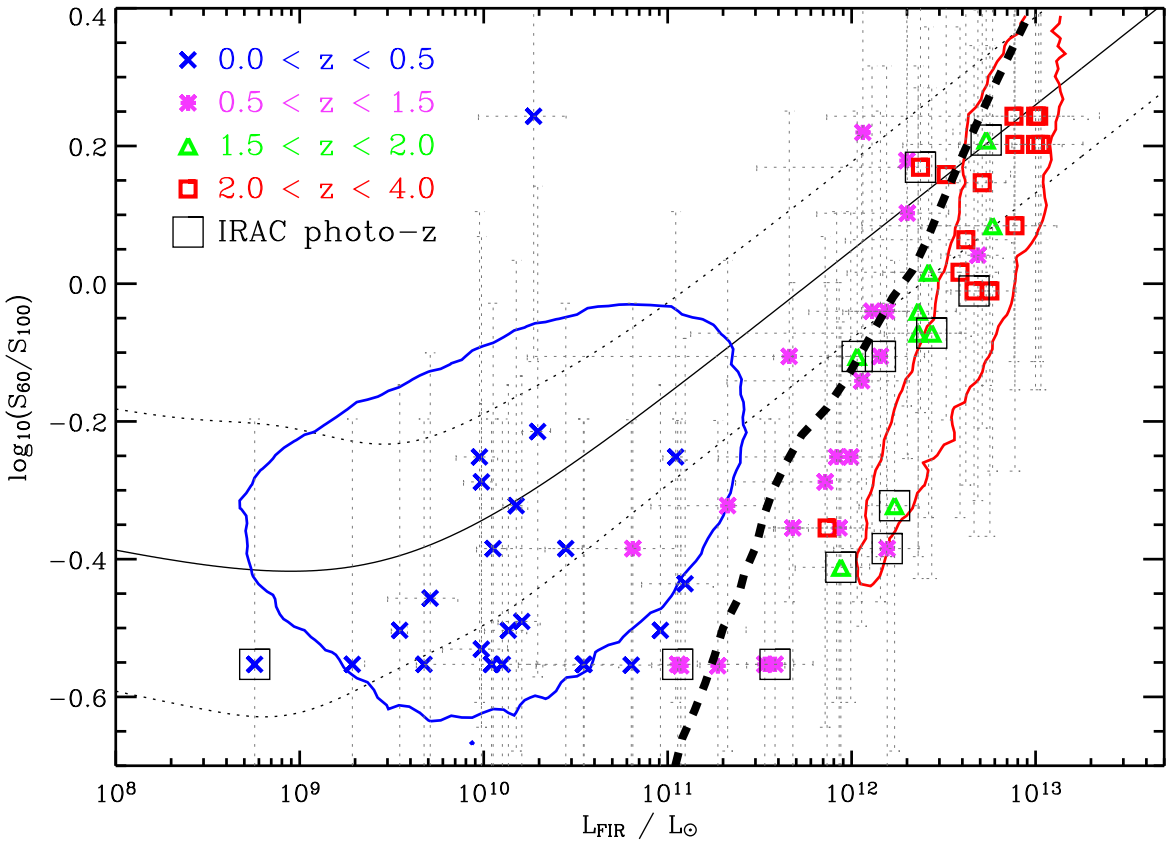

Figure 7. Rest-frame $\log_{10}(S_{60}/S_{100})$ colours vs. integrated 42.5–122.5 µm far-infrared (FIR) luminosities inferred from fits of Dale et al. (2001) SED templates to the submm and FIR photometry for our sample. The solid black line shows the local correlation derived from *IRAS* galaxies in Chapin et al. (2009), with the dotted black line its 68% confidence interval. The symbols are data points from our survey, divided into sources at $z < 0.5$, $0.5 < z < 1.5$, $1.5 < z < 2.0$, and $2.0 < z < 4.02$ (including the highest-redshift source in the sample). We indicate the sources with IRAC-based photometric redshifts as they are highly uncertain, and may be biased low. If these sources are at higher redshifts, they will move up and right in this plot. For comparison, we generated a realization of sources from a non-evolving FIR colour-luminosity distribution (Chapin et al. 2009), extrapolating to the BLAST wavelengths using the Dale et al. (2001) SED templates, and applying flux density cuts 40, 30, and 20 mJy at 250, 350, and 500 µm respectively. Sub-samples were then made for the $0.0 < z < 0.5$ and $2.0 < z < 4.0$ redshifts bins, and their 90% confidence intervals are shown as solid blue and red contours respectively. For further illustration we also show the BLAST selection function at $z = 0.5$ with a thick black dashed line. The reasonable agreement between the model contours and the sample demonstrates that the generally cooler (more negative) colours for our sample can be explained by selection effects, rather than evolution in the colour-luminosity correlation at high redshift.

white and confusion noise) is estimated to be 5.8, 5.6, and 5.7 mJy at 250, 350, and 500 mJy, respectively. We compare the 250 µm match-filtered map with the raw and PSF-filtered maps in Fig. 8. In all three cases we indicate submm peaks with brightnesses $S_{250} > 10$ mJy (which are $> 5\,\sigma$ detections with respect to instrumental noise), as well as the locations of the known input sources to the simulation. Clearly these data have a SNR (with respect to instrumental noise) significantly higher than the BLAST 250 µm data; therefore the improvement in the match-filtered results over the raw and PSF-filtered maps is more pronounced than for the BLAST data shown in Fig. 1.

We draw attention to the fact that the SPIRE peaks are obviously blends of multiple significant sources in most cases. To quantify the confusion we have repeated the radial excess counts following Appendix B1, using the known input source positions as the matching catalogue. At 250 µm, which we emphasize is the *least* confused SPIRE band, we find: $\sigma_r = 4.0$ arcsec (radial positional uncertainty) and $E = 1.8$ (average number of excess sources contributing to peak) in the raw maps; $\sigma_r = 2.3$ arcsec and $E = 1.3$ in the match-filtered maps; and $\sigma_r = 5.4$ arcsec and $E = 2.3$ in the PSF-filtered maps. In other words, peaks in the raw 250 µm maps are often blends of about two galaxies, while the matched-filter is able to significantly de-convolve the beam and improve the positional uncertainties. This example also clearly demonstrates that convolution with the full PSF is *the wrong* approach to take with deep SPIRE data.

We have repeated this procedure for the longer wavelengths (also using a limiting flux density of 10 mJy for the peak catalogues), and find for the match-filtered maps: $\sigma_r = 4.1$ arcsec and $E = 1.8$ at 350 µm; and $\sigma_r = 6.8$ arcsec and $E = 2.5$ for the match-filtered maps at 500 µm. Therefore, confusion is a significant issue, even in the match-filtered maps, at the longer wavelengths that are better suited to detecting the highest-redshift sources.

In summary, deep SPIRE data are considerably confused at levels that lie between the LABOCA and BLAST

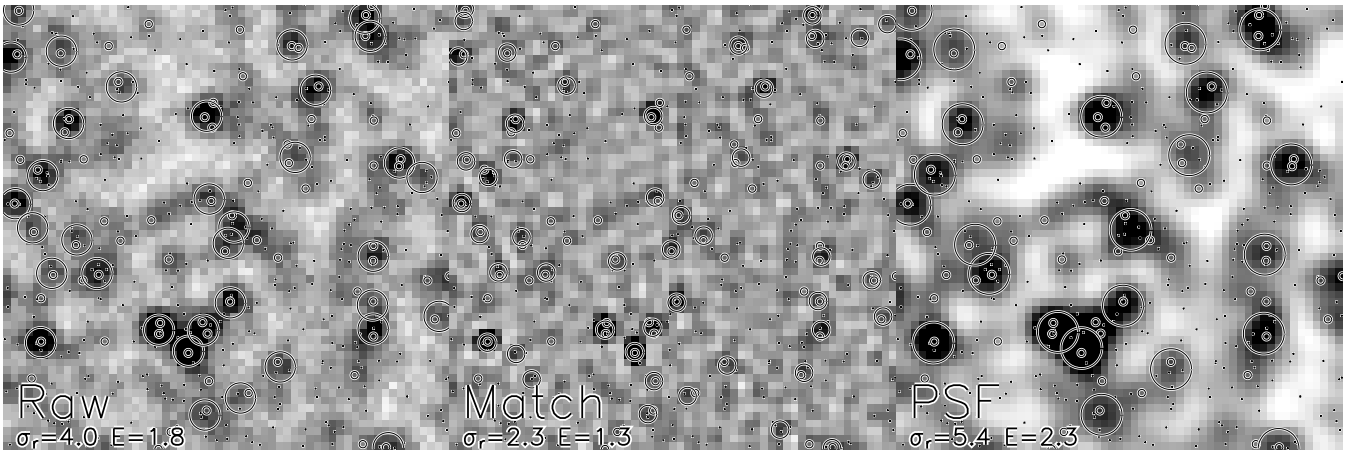

Figure 8. A simulated 0.1 deg×0.1 deg 250 μm SPIRE observation, with a depth similar to the real *Herschel* Science Demonstration Phase GOODS-N data taken as a part of *HerMES*. The palette is scaled from −15 mJy (white) to +20 mJy (black). The panels show, from left to right, the raw, match-filtered, and PSF-filtered maps. The large circles indicate submm peaks with flux densities $S_{250} > 10$ mJy, and their radii are $3\,\sigma_{\rm r}$, where σ_r is estimated as in Appendix B1 using a matching catalogue consisting of input sources with $S_{250} > 4$ mJy. The small circles and dots indicate input sources with flux densities $S_{250} > 10$ mJy, and 4 mJy $< S_{250} <$ 10 mJy, respectively. The match-filtered image is significantly less confused than the raw and PSF-filtered maps, but in many cases the submm peaks are still clearly blends of multiple sources.

data, as expected given the relative beam sizes. Matched-filtering has an even greater potential to de-blend and improve the positional uncertainty for SPIRE than for BLAST due to the improved SNR. However, SPIRE peak catalogues will still generally represent blends of multiple sources. It will therefore be necessary to identify multiple potential counterparts to each peak, and we advocate performing a simultaneous fit to the data as we have done to the BLAST data in order to produce the least-biased photometry. Finally, while not simulated here, the considerably larger catalogues of SPIRE peaks will enable estimates of priors for Likelihood Ratios (as in Section 3) with considerably smaller statistical errors. In fact, LRs have already been use to propose identifications for SPIRE sources in Smith et al. (2010). However, they have calculated counterpart reliabilities following Sutherland & Saunders (1992), which we suspect may be biased due to the impact of confusion (see discussion in Appendix B).

6 CONCLUSIONS

We have performed a deep multi-wavelength study of individual peaks from the BLAST 250, 350, and 500 μm survey within the Extended Chandra Deep Field South (ECDF-S). By comparing the BLAST data with LABOCA ECDFS Submm Survey (LESS) maps at 870 μm we have been able to greatly improve the positional uncertainties and longer-wavelength (Rayleigh-Jeans tail) SEDs for our sample. Compared to the earlier BLAST studies of Dye et al. (2009), Ivison et al. (2010) and Dunlop et al. (2010), our methodology for identifying counterparts and measuring flux densities differ in several key respects:

• It is recognized that peaks in the submm maps (particularly the BLAST bands) are generally blends of several unrelated sources. It is therefore important to search for *multiple* counterparts to each peak in a matching catalogue, whereas earlier BLAST catalogue-based studies tended to focus on *single* counterparts.

• We use a new 'matched filter' that compensates for source confusion when searching for submm sources. For the BLAST bands, in which the contribution to the total noise by source confusion is roughly a factor of two larger than the instrumental noise, there is a significant improvement in SNR of approximately 15–20%. In contrast, there is only a minimal improvement of about 5% for the LESS data since the confusion and instrumental noise components are approximately the same.

• Identifications in our combined radio/IR matching catalogue have been made using Likelihood Ratios that incorporate more prior information than traditional 'P' statistics. With a threshold spurious ID rate set at 10%, we find 52, 50, and 31 matches to 64, 67, and 55 submm peak positions at 250, 350, and 500 μm, respectively. This is a significant improvement compared to the match rates obtained using 10% cuts on P giving 45, 31, and 12 matches in the 24 μm catalogue, and 51, 35, and 17 matches in 1.4 GHz catalogue. Most of the gain is at 500 μm where the beam is so large that any additional information to help the process clearly makes a large difference. Combining the identifications made independently in each band, approximately 75% of the BLAST selected peaks have at least one potential counterpart.

• We obtain submm photometry for the 118 unique identifications in the matching catalogue by performing a simultaneous fit of the submm PSFs at the precise ID locations in each of the four original (un-smoothed) submm maps. This procedure results in useful measurements for 76 sources; the remaining 42 sources are too close to one another to reliably disentangle the flux densities produced by each of the contributing objects. In order to make further progress in such cases, prior information for the SEDs will likely be needed (see, for example, the work of Roseboom et al. 2009).

• Our procedure for identifying counterparts and measuring their flux densities has compensated for much of the 'flux-boosting' present in the original flux-limited submm

peak lists. Comparing the number counts of our final catalogue in the BLAST bands with the $P(D)$ counts from Patanchon et al. (2009) we find good agreement above 40 mJy at 250 μm, 30 mJy at 350 μm and with somewhat lower completeness reaching a maximum of $\sim$ 66% above 20 mJy at 500 μm.

We then proceeded to identify redshifts for the counterparts, and hence probe the rest-frame properties of our sample:

• Of the 76 sources with usable submm photometry, 69 counterparts have redshifts: 23 are optical spectroscopic redshifts; 35 are optical photometric redshifts; and 11 are IRAC photometric redshifts. The median of the entire distribution is $z = 1.1$ with an interquartile range 0.3–1.9. Restricting ourselves to sub-samples above the flux-density limits mentioned previously shows a clear trend in increasing redshift with observed wavelength: a median $z = 1.1$ with an interquartile range 0.2–1.9 at 250 μm; a median $z = 1.3$ with an interquartile range 0.6–2.1 at 350 μm; and a median $z = 1.6$ with an interquartile range 1.3–2.3 at 500 μm. In general, there is a higher-redshift tail for our sample than in the earlier study of Dye et al. (2009) which we believe is due to the fainter flux densities probed.

• Fitting modified blackbody SEDs of the form $S_\nu \propto \nu^{2.0} B_\nu(T)$ to the 69 sources with useable submm photometry and redshifts, we establish rest-frame cold-dust temperatures. The total distribution has a median $T = 29$ K and interquartile range 23–36 K. There is almost no variation in the temperatures of the different flux-limited sub-samples: a median $T = 30$ K with an interquartile range 25–39 K at 250 μm; a median $T = 30$ K with an interquartile range 23–35 K at 350 μm; and a median $T = 30$ K with an interquartile range 22–38 K at 500 μm. These temperatures are systematically warmer by about 7 K than those inferred in Dye et al. (2009). While this discrepancy may be partly caused by the relative depths of the samples, we believe it is mostly due to improved compensation for confusion (which reduces the estimated flux densities at longer BLAST wavelengths more than at shorter wavelengths), and the inclusion of higher-resolution 870 μm data from LESS.

• The primary improvement over earlier catalogue-based BLAST studies is the characterization of submm SEDs for the fainter, but higher-redshift ($z \gtrsim 1$) and more-luminous galaxies. Even though the earlier analyses typically considered single counterparts to the BLAST peaks, these counterparts *are* probably significant submm emitters (although the measured flux densities were typically high, especially in the most confused 500 μm band). Therefore the measured properties of the optical counterparts (approximate redshift distributions, galaxy types etc.), and even the FIR temperatures and luminosities of the brighter, lower-redshift galaxies are generally correct.

• We have also fit star-forming galaxy SED templates from the library of Dale et al. (2001) (which span the radio–near-IR) to the submm and FIR photometry of our sample. Generally speaking there is good correspondence between these models and the photometry in the radio and near/mid-IR, confirming that most of the emission is probably powered by star-formation. However, about 8% of the sample exhibits a significant excess in either (or both) of these wavelength regimes, which could indicate AGN activity. We note that these features are restricted to sources with luminosities primarily in the range $11.5 < \log(L_{\rm FIR}) < 12.8$, near the bright end of our sample.

• We compare the distribution of luminosity and cold dust temperature in our sample with the local-Universe measurement of Chapin et al. (2009). While the submm colours of our sources appear systematically cooler at all luminosities compared to the local distribution, we have determined that the distribution is consistent with selection effects in our survey. We therefore find no evidence for evolution in the temperature-luminosity correlation out to $z \sim 2.5$.

• Finally, we investigate the utility of the methods described in this paper for the new generation of *Herschel*/SPIRE surveys. Using a simple simulation we show that these new surveys are significantly confused, despite a factor of $\sim$2 improvement in angular resolution over BLAST. We find that the matched-filter will yield a *greater* improvement in the detection of point sources than for BLAST due to the significantly lower instrumental noise of SPIRE. However, even with these improvements, peaks in SPIRE maps will be confused, and we advocate the use of Likelihood Ratios to identify the expected multiple counterparts.

7 ACKNOWLEDGEMENTS

BLAST acknowledges the support of NASA through grant numbers NAG5-12785, NAG5-13301, and NNGO-6GI11G, the NSF Office of Polar Programs, the Canadian Space Agency, the Natural Sciences and Engineering Research Council (NSERC) of Canada, and STFC. This paper contains data obtained by APEX, which is operated by the Max-Planck-Institut für Radioastronomie, the European Southern Observatory, and the Onsala Space Observatory. LESS is a joint MPI-ESO collaboration and the data were obtained during the following ESO observing runs: 078.F-9028(A), 079.F-9500(A), 080.A-3023(A), and 081.F-9500(A). This work is based in part on observations made with the Spitzer Space Telescope, which is operated by the Jet Propulsion Laboratory, California Institute of Technology under a contract with NASA. IRS and KEKC acknowledge support from STFC. JSD acknowledges the support of the Royal Society through a Wolfson Research Merit Award. EC thanks John Peacock and Seb Oliver for useful discussions regarding Likelihood Ratios.

REFERENCES

Aretxaga I., Hughes D. H., Chapin E. L., Gaztañaga E., Dunlop J. S., Ivison R. J., 2003, MNRAS, 342, 759

Austermann J. E., Dunlop J. S., Perera T. A., Scott K. S., Wilson G. W., Aretxaga I., Hughes D. H., Almaini O., Chapin E. L., Chapman S. C., Cirasuolo M., Clements D. L., Coppin K. E. K., Dunne L., 2010, MNRAS, 401, 160

Barger A. J., Cowie L. L., Sanders D. B., Fulton E., Taniguchi Y., Sato Y., Kawara K., Okuda H., 1998, Nature, 394, 248

Barnard V. E., Vielva P., Pierce-Price D. P. I., Blain A. W., Barreiro R. B., Richer J. S., Qualtrough C., 2004, MNRAS, 352, 961

Barreiro R. B., Sanz J. L., Herranz D., Martínez-González E., 2003, MNRAS, 342, 119
Baugh C. M., Lacey C. G., Frenk C. S., Granato G. L., Silva L., Bressan A., Benson A. J., Cole S., 2005, MNRAS, 356, 1191
Blain A. W., Smail I., Ivison R. J., Kneib J.-P., Frayer D. T., 2002, PhR, 369, 111
Borys C., Chapman S., Halpern M., Scott D., 2003, MNRAS, 344, 385
Brammer G. B., van Dokkum P. G., Coppi P., 2008, ApJ, 686, 1503
Casey C. M., Chapman S. C., Smail I., Alaghband-Zadeh S., Bothwell M. S., Swinbank A. M., 2010, ArXiv e-prints
Chanial P., Flores H., Guiderdoni B., Elbaz D., Hammer F., Vigroux L., 2007, A&A, 462, 81
Chapin E. L., Ade P. A. R., Bock J. J., Brunt C., Devlin M. J., Dicker S., Griffin M., Gundersen J. O., Halpern M., Hargrave P. C., Hughes D. H., 2008, ApJ, 681, 428
Chapin E. L., Hughes D. H., Aretxaga I., 2009, MNRAS, 393, 653
Chapin E. L., Pope A., Scott D., Aretxaga I., Austermann J. E., Chary R., Coppin K., Halpern M., Hughes D. H., Lowenthal J. D., Morrison G. E., Perera T. A., Scott K. S., Wilson G. W., Yun M. S., 2009, MNRAS, 398, 1793
Chapman S. C., Blain A. W., Ivison R. J., Smail I. R., 2003, Nature, 422, 695
Chapman S. C., Blain A. W., Smail I., Ivison R. J., 2005, ApJ, 622, 772
Chapman S. C., Helou G., Lewis G. F., Dale D. A., 2003, ApJ, 588, 186
Chapman S. C., Smail I., Windhorst R., Muxlow T., Ivison R. J., 2004, ApJ, 611, 732
Chary R., Pope A., 2010, ArXiv e-prints
Clements D., Eales S., Wojciechowski K., Webb T., Lilly S., Dunne L., Ivison R., McCracken H., Yun M., James A., Brodwin M., Le Fèvre O., Gear W., 2004, MNRAS, 351, 447
Coppin K., Chapin E. L., Mortier A. M. J., Scott S. E., Borys C., Dunlop J. S., Halpern M., Hughes D. H., Pope A., Scott D., Serjeant S., Wagg J., Alexander D. M., 2006, MNRAS, 372, 1621
Coppin K., Halpern M., Scott D., Borys C., Chapman S., 2005, MNRAS, 357, 1022
Coppin K., Halpern M., Scott D., Borys C., Dunlop J., Dunne L., Ivison R., Wagg J., Aretxaga I., Battistelli E., Benson A., Blain A., Chapman S., Clements D., Dye S., Farrah D., Hughes D., Jenness T., 2008, MNRAS, 384, 1597
Coppin K. E. K., Smail I., Alexander D. M., Weiss A., Walter F., Swinbank A. M., Greve T. R., Kovacs A., De Breuck C., Dickinson M., Ibar E., Ivison R. J., Reddy N., Spinrad H., Stern D., Brandt W. N., Chapman S. C., Dannerbauer H., 2009, MNRAS, 395, 1905
Cowie L. L., Barger A. J., Kneib J.-P., 2002, Astron. J., 123, 2197
Dale D. A., Helou G., Contursi A., Silbermann N. A., Kolhatkar S., 2001, ApJ, 549, 215
Dannerbauer H., Lehnert M. D., Lutz D., Tacconi L., Bertoldi F., Carilli C., Genzel R., Menten K. M., 2004, ApJ, 606, 664
Devlin M. J., Ade P. A. R., Aretxaga I., Bock J. J., Chapin E. L., Griffin M., Gundersen J. O., Halpern M., Hargrave P. C., Hughes D. H., Klein J., Marsden G., Martin P. G., Mauskopf P., Moncelsi L., Netterfield C. B., 2009, Nature, 458, 737
Downes A. J. B., Peacock J. A., Savage A., Carrie D. R., 1986, MNRAS, 218, 31
Dunlop J. S., Ade P. A. R., Bock J. J., Chapin E. L., Cirasuolo M., Coppin K. E. K., Devlin M. J., Griffin M., Greve T. R., Gundersen J. O., 2010, MNRAS, pp 1354–+
Dye S., Ade P. A. R., Bock J. J., Chapin E. L., Devlin M. J., Dunlop J. S., Eales S. A., Griffin M., Gundersen J. O., Halpern M., Hargrave P. C., Hughes D. H., Klein J., 2009, ApJ, 703, 285
Eales S., Chapin E. L., Devlin M. J., Dye S., Halpern M., Hughes D. H., Marsden G., Mauskopf P., Moncelsi L., Netterfield C. B., Pascale E., Patanchon G., Raymond G., Rex M., Scott D., Semisch C., Siana B., Truch M. D. P., Viero M. P., 2009, ApJ, 707, 1779
Fixsen D. J., Dwek E., Mather J. C., Bennett C. L., Shafer R. A., 1998, ApJ, 508, 123
Fox M. J., Efstathiou A., Rowan-Robinson M., Dunlop J. S., Scott S., Serjeant S., Mann R. G., Oliver S., Ivison R. J., Blain A., Almaini O., Hughes D., Willott C. J., Longair M., Lawrence A., Peacock J. A., 2002, MNRAS, 331, 839
Gawiser E., van Dokkum P. G., Herrera D., Maza J., Castander F. J., Infante L., Lira P., Quadri R., Toner R., Treister E., Urry C. M., Altmann M., Assef R., Christlein D., 2006, ApJS, 162, 1
Grazian A., Fontana A., de Santis C., Nonino M., Salimbeni S., Giallongo E., Cristiani S., Gallozzi S., Vanzella E., 2006, A&A, 449, 951
Greve T. R., Ivison R. J., Bertoldi F., Stevens J. A., Dunlop J. S., Lutz D., Carilli C. L., 2004, MNRAS, 354, 779
Güsten R., Nyman L. Å., Schilke P., Menten K., Cesarsky C., Booth R., 2006, A&A, 454, L13
Hainline L. J., Blain A. W., Smail I., Frayer D. T., Chapman S. C., Ivison R. J., Alexander D. M., 2009, ApJ, 699, 1610
Holland W. S., Robson E. I., Gear W. K., Cunningham C. R., Lightfoot J. F., Jenness T., Ivison R. J., Stevens J. A., Ade P. A. R., Griffin M. J., Duncan W. D., Murphy J. A., Naylor D. A., 1999, MNRAS, 303, 659
Hughes D. H., Serjeant S., Dunlop J., Rowan-Robinson M., Blain A., Mann R. G., Ivison R., Peacock J., Efstathiou A., Gear W., Oliver S., Lawrence A., Longair M., Goldschmidt P., Jenness T., 1998, Nature, 394, 241
Iono D., Peck A. B., Pope A., Borys C., Scott D., Wilner D. J., Gurwell M., Ho P. T. P., Yun M. S., Matsushita S., Petitpas G. R., Dunlop J. S., Elvis M., Blain A., Le Floc'h E., 2006, ApJL, 640, L1
Ivison R. J., Alexander D. M., Biggs A. D., Brandt W. N., Chapin E. L., Coppin K. E. K., Devlin M. J., Dickinson M., Dunlop J., Dye S., Eales S. A., Frayer D. T., Halpern M., 2010, MNRAS, 402, 245
Ivison R. J., Greve T. R., Dunlop J. S., Peacock J. A., Egami E., Smail I., Ibar E., van Kampen E., Aretxaga I., Babbedge T., Biggs A. D., Blain A. W., Chapman S. C., Clements D. L., 2007, MNRAS, 380, 199
Ivison R. J., Greve T. R., Serjeant S., Bertoldi F., Egami E., Mortier A. M. J., Alonso-Herrero A., Barmby P., Bei L., Dole H., Engelbracht C. W., Fazio G. G., Frayer D. T., 2004, ApJS, 154, 124

Ivison R. J., Greve T. R., Smail I., Dunlop J. S., Roche N. D., Scott S. E., Page M. J., Stevens J. A., Almaini O., Blain A. W., Willott C. J., Fox M. J., Gilbank D. G., Serjeant S., Hughes D. H., 2002, MNRAS, 337, 1

Khan S. A., Shafer R. A., Serjeant S., Willner S. P., Pearson C. P., Benford D. J., Staguhn J. G., Moseley S. H., Sumner T. J., Ashby M. L. N., Borys C. K., Chanial P., Clements D. L., Dowell C. D., Dwek E., Fazio G. G., Kovács A., Le Floc'h E., Silverberg R. F., 2007, ApJ, 665, 973

Klaas U., Haas M., Müller S. A. H., Chini R., Schulz B., Coulson I., Hippelein H., Wilke K., Albrecht M., Lemke D., 2001, A&A, 379, 823

Kovács A., Chapman S. C., Dowell C. D., Blain A. W., Ivison R. J., Smail I., Phillips T. G., 2006, ApJ, 650, 592

Lagache G., Dole H., Puget J.-L., 2003, MNRAS, 338, 555

Laurent G. T., Aguirre J. E., Glenn J., Ade P. A. R., Bock J. J., Edgington S. F., Goldin A., Golwala S. R., Haig D., Lange A. E., Maloney P. R., Mauskopf P. D., Nguyen H., Rossinot P., Sayers J., Stover P., 2005, ApJ, 623, 742

Lutz D., Dunlop J. S., Almaini O., Andreani P., Blain A., Efstathiou A., Fox M., Genzel R., Hasinger G., Hughes D., 2001, A&A, 378, 70

Magnelli B., Elbaz D., Chary R. R., Dickinson M., Le Borgne D., Frayer D. T., Willmer C. N. A., 2009, A&A, 496, 57

Mann R. G., Oliver S. J., Serjeant S. B. G., Rowan-Robinson M., Baker A., Eaton N., Efstathiou A., Goldschmidt P., Mobasher B., Sumner T. J., 1997, MNRAS, 289, 482

Marsden G., Ade P. A. R., Bock J. J., Chapin E. L., Devlin M. J., Dicker S. R., Griffin M., Gundersen J. O., Halpern M., Hargrave P. C., Hughes D. H., Klein J., Mauskopf P., Magnelli B., Moncelsi L., Netterfield C. B., Ngo H., 2009, ApJ, 707, 1729

Menéndez-Delmestre K., Blain A. W., Smail I., Alexander D. M., Chapman S. C., Armus L., Frayer D., Ivison R. J., Teplitz H., 2009, ApJ, 699, 667

Miller N. A., Fomalont E. B., Kellermann K. I., Mainieri V., Norman C., Padovani P., Rosati P., Tozzi P., 2008, ApJS, 179, 114

Mo H. J., White S. D. M., 1996, MNRAS, 282, 347

Moncelsi L., Ade P. A. R., Chapin E. L., Cortese L., Devlin M. J., Dye S., Eales S., Griffin M., Halpern M., Hargrave P. C., Marsden G., Mauskopf P., Netterfield C. B., Pascale E., Scott D., Truch M. D. P., Tucker C., Viero M., Wiebe D., 2010, ArXiv e-prints

Nguyen H. T., Schulz B., Levenson L., Amblard A., Arumugam V., Aussel H., Babbedge T., Blain A., Bock J., Boselli A., Buat V., Castro-Rodriguez N., Cava A., Chanial P., Chapin E., 2010, A&A, 518, L5+

Oliver S. J., Wang L., Smith A. J., Altieri B., Amblard A., Arumugam V., Auld R., Aussel H., Babbedge T., Blain A., Bock J., Boselli A., Buat V., Burgarella D., 2010, A&A, 518, L21+

Pascale E., Ade P. A. R., Bock J. J., Chapin E. L., Chung J., Devlin M. J., Dicker S., Griffin M., Gundersen J. O., Halpern M., Hargrave P. C., Hughes D. H., Klein J., MacTavish C. J., 2008, ApJ, 681, 400

Pascale E., Ade P. A. R., Bock J. J., Chapin E. L., Devlin M. J., Dye S., Eales S. A., Griffin M., Gundersen J. O., Halpern M., Hargrave P. C., Hughes D. H., Klein J., 2009, ApJ, 707, 1740

Patanchon G., Ade P. A. R., Bock J. J., Chapin E. L., Devlin M. J., Dicker S., Griffin M., Gundersen J. O., Halpern M., Hargrave P. C., Hughes D. H., Klein J., Marsden G., Martin P. G., 2008, ApJ, 681, 708

Patanchon G., Ade P. A. R., Bock J. J., Chapin E. L., Devlin M. J., Dicker S. R., Griffin M., Gundersen J. O., Halpern M., Hargrave P. C., Hughes D. H., Klein J., Marsden G., Mauskopf P., 2009, ApJ, 707, 1750

Perera T. A., Chapin E. L., Austermann J. E., Scott K. S., Wilson G. W., Halpern M., Pope A., Scott D., Yun M. S., Lowenthal J. D., Morrison G., Aretxaga I., Bock J. J., Coppin K., Crowe M., Frey L., Hughes D. H., Kang Y., Kim S., Mauskopf P. D., 2008, MNRAS, 391, 1227

Pope A., Scott D., Dickinson M., Chary R.-R., Morrison G., Borys C., Sajina A., Alexander D. M., Daddi E., Frayer D., MacDonald E., Stern D., 2006, MNRAS, 370, 1185

Pope E. A., 2007, PhD thesis, The University of British Columbia (Canada

Puget J., Abergel A., Bernard J., Boulanger F., Burton W. B., Desert F., Hartmann D., 1996, A&A, 308, L5+

Roseboom I. G., Oliver S., Parkinson D., Vaccari M., 2009, MNRAS, 400, 1062

Rowan-Robinson M., 2001, ApJ, 549, 745

Rowan-Robinson M., 2009, MNRAS, 394, 117

Rowan-Robinson M., Babbedge T., Oliver S., Trichas M., Berta S., Lonsdale C., Smith G., Shupe D., Surace J., Arnouts S., 2008, MNRAS, 386, 697

Rutledge R. E., Brunner R. J., Prince T. A., Lonsdale C., 2000, ApJS, 131, 335

Sanders D. B., Mirabel I. F., 1996, ARAA, 34, 749

Sawicki M., 2002, Astron. J., 124, 3050

Scott K. S., Austermann J. E., Perera T. A., Wilson G. W., Aretxaga I., Bock J. J., Hughes D. H., Kang Y., Kim S., Mauskopf P. D., Sanders D. B., Scoville N., Yun M. S., 2008, MNRAS, 385, 2225

Scott S. E., Fox M. J., Dunlop J. S., Serjeant S., Peacock J. A., Ivison R. J., Oliver S., Mann R. G., Lawrence A., Efstathiou A., Rowan-Robinson M., Hughes D. H., Archibald E. N., Blain A., Longair M., 2002, MNRAS, 331, 817

Serjeant S., Dunlop J. S., Mann R. G., Rowan-Robinson M., Hughes D., Efstathiou A., Blain A., Fox M., Ivison R. J., Jenness T., Lawrence A., Longair M., Oliver S., Peacock J. A., 2003, MNRAS, 344, 887

Simpson C., Eisenhardt P., 1999, PASP, 111, 691

Siringo G., Kreysa E., Kovács A., Schuller F., Weiß A., Esch W., Gemünd H., Jethava N., Lundershausen G., Colin A., Güsten R., Menten K. M., Beelen A., Bertoldi F., Beeman J. W., Haller E. E., 2009, A&A, 497, 945

Smail I., Ivison R. J., Blain A. W., 1997, ApJL, 490, L5+

Smail I., Ivison R. J., Owen F. N., Blain A. W., Kneib J., 2000, ApJ, 528, 612

Smith D. J. B., Dunne L., Maddox S. J., Eales S., Bonfield D. G., Jarvis M. J., Sutherland W., Fleuren S., Rigby E. E., 2010, ArXiv e-prints

Stetson P. B., 1987, Publ. Astron. Soc. Pac., 99, 191

Sutherland W., Saunders W., 1992, MNRAS, 259, 413

Tacconi L. J., Genzel R., Smail I., Neri R., Chapman S. C., Ivison R. J., Blain A., Cox P., Omont A., Bertoldi F., Greve T., 2008, ApJ, 680, 246

Takeuchi T. T., Yoshikawa K., Ishii T. T., 2003, ApJL, 587, L89

Takeuchi T. T., Yoshikawa K., Ishii T. T., 2004, ApJL, 606, L171
Taylor E. N., Franx M., van Dokkum P. G., Quadri R. F., Gawiser E., Bell E. F., Barrientos L. F., Blanc G. A., Castander F. J., Damen M., Gonzalez-Perez V., Hall P. B., Herrera D., Hildebrandt H., 2009, ApJS, 183, 295
Tegmark M., de Oliveira-Costa A., 1998, ApJL, 500, L83+
Truch M. D. P., Ade P. A. R., Bock J. J., Chapin E. L., Devlin M. J., Dicker S. R., Griffin M., Gundersen J. O., Halpern M., Hargrave P. C., Hughes D. H., Klein J., Marsden G., 2009, ApJ, 707, 1723
Väisänen P., Kotilainen J. K., Juvela M., Mattila K., Efstathiou A., Kahanpää J., 2010, MNRAS, 401, 1587
Valiante E., Lutz D., Sturm E., Genzel R., Chapin E. L., 2009, ApJ, 701, 1814
Viero M. P., Ade P. A. R., Bock J. J., Chapin E. L., Devlin M. J., Griffin M., Gundersen J. O., Halpern M., Hargrave P. C., Hughes D. H., Klein J., MacTavish C. J., Marsden G., 2009, ApJ, 707, 1766
Vio R., Andreani P., Wamsteker W., 2004, A&A, 414, 17
Wang W., Cowie L. L., Barger A. J., 2006, ApJ, 647, 74
Webb T. M., Eales S. A., Lilly S. J., Clements D. L., Dunne L., Gear W. K., Ivison R. J., Flores H., Yun M., 2003, ApJ, 587, 41
Weiss A., Kovacs A., Coppin K., Greve T. R., Walter F., Smail I., Dunlop J. S., Knudsen K. K., Alexander D. M., Bertoldi F., Brandt W. N., Chapman S. C., Cox P., 2009, ArXiv e-prints
Wiebe D. V., Ade P. A. R., Bock J. J., Chapin E. L., Devlin M. J., Dicker S., Griffin M., Gundersen J. O., Halpern M., Hargrave P. C., Hughes D. H., Klein J., Marsden G., Martin P. G., 2009, ApJ, 707, 1809
Wilman R. J., Jarvis M. J., Mauch T., Rawlings S., Hickey S., 2010, ArXiv e-prints
Wilson G. W., Austermann J. E., Perera T. A., Scott K. S., Ade P. A. R., Bock J. J., Glenn J., Golwala S. R., Kim S., Kang Y., Lydon D., Mauskopf P. D., Predmore C. R., Roberts C. M., Souccar K., Yun M. S., 2008, MNRAS, 386, 807
Wolf C., Hildebrandt H., Taylor E. N., Meisenheimer K., 2008, A&A, 492, 933
Wolf C., Meisenheimer K., Kleinheinrich M., Borch A., Dye S., Gray M., Wisotzki L., Bell E. F., Rix H., Cimatti A., Hasinger G., Szokoly G., 2004, A&A, 421, 913
Younger J. D., Fazio G. G., Huang J., Yun M. S., Wilson G. W., Ashby M. L. N., Gurwell M. A., Lai K., Peck A. B., Petitpas G. R., Wilner D. J., Iono D., Kohno K., Kawabe R., 2007, ApJ, 671, 1531
Yun M. S., Aretxaga I., Ashby M. L. N., Austermann J., Fazio G. G., Giavalisco M., Huang J.-S., Hughes D. H., Kim S., Lowenthal J. D., Perera T., Scott K., Wilson G., Younger J. D., 2008, MNRAS, 389, 333

APPENDIX A: MATCHED FILTER

Here we describe a filter for identifying point sources in maps containing significant contributions of both instrumental noise and confusion due to blending of other point sources (see e.g. Tegmark & de Oliveira-Costa 1998; Barreiro et al. 2003; Vio et al. 2004, for related studies of point sources in maps of the Cosmic Microwave Background). We formulate the problem as follows: we wish to find the 'matched filter', F, that maximizes the SNR one would obtain when cross-correlating F with the signal of interest, S – in our case, a point source whose shape is identical to the PSF – in the presence of noise, N. We proceed by expressing the total SNR resulting from this operation, ϕ, in Fourier space,

$$\phi \equiv \frac{\text{Signal}}{\text{Noise}} = \frac{\sum_k \hat{F}_k^T \hat{S}_k}{\left(\sum_k |\hat{F}_k^T \hat{N}_k|^2\right)^{1/2}}. \quad \text{(A1)}$$

In this expression the carets denote discrete Fourier transforms, and the index k runs over all elements in the spatial frequency domain. The superscript 'T' indicates that we use the transpose of F in the expression.[5] Taking the partial derivatives of ϕ with respect to each mode j in the filter, $\hat{F}_j^T$, and setting them to 0, one can solve for the filter that maximizes the SNR:

$$0 = \frac{\partial \phi}{\partial \hat{F}_j^T} \quad \text{(A2)}$$

$$= \frac{\hat{S}_j}{\left(\sum_k |\hat{F}_k^T \hat{N}_k|^2\right)^{1/2}} - \hat{F}_j^T |\hat{N}_j|^2 \left(\frac{\sum_k \hat{F}_k^T \hat{S}_k}{\left(\sum_k |\hat{F}_k^T \hat{N}_k|^2\right)^{3/2}} \right)$$

$$\Rightarrow \hat{F}_j^T = \frac{\hat{S}_j}{|\hat{N}_j|^2} \left(\frac{\sum_k |\hat{F}_k^T \hat{N}_k|^2}{\sum_k \hat{F}_k^T \hat{S}_k} \right) \propto \frac{\hat{S}_j}{|\hat{N}_j|^2}. \quad \text{(A3)}$$

In other words, in Fourier space the matched filter is simply the PSF weighted by the inverse noise variance at each spatial frequency. In the case of an isolated point source in a field of white noise, this expression results in the PSF, since $\hat{N}$ is constant. This is the well-known result (e.g. Stetson 1987) that the best way to find point sources in a noisy map is to convolve with the PSF. However, this procedure is only optimal if the noise is white. For our submm maps we consider two components of noise: instrumental white noise, $N_{\rm w}$, and the confusion noise caused by other point sources, $N_{\rm c}$.

For the case at hand we estimate $N_{\rm w}$ (constant at all spatial frequencies) assuming typical noise values at the centres of each submm ECDF-S map: 32, 29, 27, and 2 mJy[6] at 250, 350, 500, and 870 μm, respectively (Devlin et al. 2009; Weiss et al. 2009). For the confusion noise, $N_{\rm c}$, we use the counts inferred using $P(D)$ analyses from Patanchon et al. (2009) and Weiss et al. (2009), and knowledge of the PSF. In the absence of noise (and assuming no spatial clustering of sources), the sky can be thought of as a random superposition of PSF shapes with different amplitudes (i.e., δ functions smoothed by the PSF and scaled by the point source flux densities). We therefore approximate the Fourier transform of the map using a white noise distribution[7] multiplied

[5] The cross-correlation of the filter with the signal is equivalent to convolving the signal with the complex conjugate transpose of the filter. Since we are dealing with real-valued signals this operations reduces to a transpose. The convolution is then a simple product in Fourier space between the two transformed quantities.
[6] These are the noise values in the raw *un-smoothed* maps at each wavelength.
[7] In practice, even if the angular locations of galaxies are unclustered, the δ function map power spectrum is not perfectly white because the flux densities of galaxies are drawn from the number counts rather than a Gaussian distribution.

by the Fourier transform of the transpose of the PSF (by the convolution theorem); in other words the power spectrum of confusion noise rolls off in the same way as the PSF, but with a different normalization. To determine how the power spectrum of the PSF should be scaled we simulate maps in each band as described above, and use the ratios of the standard deviations of these noise realizations to the standard deviations of the PSFs.

As an example of this procedure, the estimated noise power spectrum at 500 μm, and resulting matched filter in real space (both azimuthally averaged) are shown in Fig. A1. One sees that the matched filter is somewhat narrower than the PSF filter (which has been used in most previous SMG studies) and has ringing at larger angular scales, giving it similar properties to the 'Mexican hat' kernel (see for example discussion and references within Barnard et al. 2004). In this particular case, the first large negative ring effectively removes a local baseline estimated at radii ~ 50 arcsec, and hence corrects the flux density slightly for other nearby blended sources. The matched filter is also qualitatively similar to the filter used to detect sources in deep AzTEC maps (e.g., Scott et al. 2008; Perera et al. 2008). However, in those cases only sources of atmospheric and instrumental noise are considered, since the spatial noise power spectrum is estimated using 'jackknife maps' (produced by differencing alternating portions of the data), which explicitly removes the contribution of astronomical sources. We emphasize that here we are using such a filter to optimally extract sources in a *confused* background. Note also that in a language familiar in other fields, our filter is essentially a Wiener filter which includes source confusion explicitly as a noise term.

In addition to the calculation we describe here, we also convolved simulated maps (containing both point sources and instrumental noise) with Gaussian filters of different widths, and determined the FWHMs that optimized the SNR of point sources. These simple tests gave results comparable to the more detailed calculation above, although the SNR was slightly lower due to the lack of ringing to compensate for the noise at larger angular scales.

It should be noted that in the development of our filter we have assumed that the instrumental noise is constant across the map. Of course, in general this is not true, and one could in principle derive a different filter at each position. For the BLAST maps under discussion, a separate filter should certainly be used to detect sources in BGS-Wide and BGS-Deep, but for the present study the noise was close to uniform across the ECDF-S, and hence we used a single filter for the whole map.

As a consequence of Eq. A3, the peak SNR for an isolated point source in a field of white noise (for which $\hat{N}_k$ is constant) is obtained by convolution with a Gaussian of the same FWHM as the instrumental PSF. In the opposite extreme, for a map of confused point sources with no instrumental noise, the optimal filter is the inverse of the PSF in Fourier space, i.e., the map is *de*-convolved by the beam. For real data in which instrumental noise and confusion are both present, the degree to which the map is actually de-convolved depends on the relative amplitudes of the two noise components (see left panel of Fig. A1). The source confusion depends on the number counts (and therefore the SEDs and redshift distribution) of galaxies in the observed band, and beam size, and the instrumental noise depends on the detector sensitivity and integration time. For the data described here, these two contributions are comparable, since the submm surveys of the ECDF-S were designed to be *just* confusion-limited. The bottom-line is that in the BLAST bands, considering both noise terms, convolving with kernels that are *smaller* than the instrumental PSFs can give approximately 15–20% improvement in the SNR — quite significant considering the majority of the sources under discussion have instrumental SNR of about 4σ (see Table 1)! The improvement is less impressive in the LESS 870 μm image, since the instrumental noise dominates the RMS resulting from confusion. Most previous studies of SMGs in the regime where confusion is important have extracted sources using the PSF, and our results show that they have smoothed away some of the point source information in the maps.

APPENDIX B: LIKELIHOOD RATIOS

Here we describe our formulation of Likelihood Ratios (LR) as a means for identifying counterparts to submm peaks. The matching catalogue for which we estimate priors is described in Section 2.2. To begin, we make two basic assumptions: (i) that the radial offset of a potential ID is uncorrelated with its other properties; and (ii) that the submm flux density is uncorrelated with its other properties. The first assumption is fairly standard and uncontroversial, although the latter could be considered problematic. For example, the brightest peaks at 250 μm are known to be low-luminosity *IRAS* galaxies, whereas the fainter sources are thought to be a mixture of both low- and high-redshift galaxies. However, for now we take the practical route and choose not to make any distinction based on these properties so that we can estimate priors with reasonable SNR given the data. We then express the differential density *of true counterparts* to submm peaks as a function of their offsets, r, flux densities, S (both at 24 μm and 1.4 GHz), and colour c (IRAC $[3.6]-[4.5]$):

$$n_{\rm c}(S,c,r)dS\,dc\,dr = q(S,c)f(r)dS\,dc\,dr, \qquad \text{(B1)}$$

where $q(S,c)$ is the distribution of counterpart flux densities and colours (in the matching catalogue), and $f(r)$ is the positional probability distribution as a function of radial offset r. We assume a symmetric Gaussian probability distribution as a function of orthogonal positional coordinates which results in the Rayleigh radial probability distribution,

$$f(r) = \frac{r}{\sigma_{\rm r}^2} e^{-r^2/2\sigma_{\rm r}^2}. \qquad \text{(B2)}$$

The normalization is chosen so that $\int_0^\infty f(r)dr = 1$. Following Sutherland & Saunders (1992) $q(S,c)$ is normalized so that it integrates to *the average expected number of counterparts per submm peak*. However, while those authors assumed that this number is in the range 0–1 (i.e., the emission is produced by a *single* source, which may or may not be present in the matching catalogue), we consider cases in which the number of counterparts may be greater than this.

We can also estimate the differential density of background sources as a function of these same properties

$$n_{\rm b}(S,c,r)dS\,dc\,dr = 2\pi r\rho(S,c)dS\,dc\,dr, \qquad \text{(B3)}$$

where $\rho(S,c)$ is the surface density of background sources as

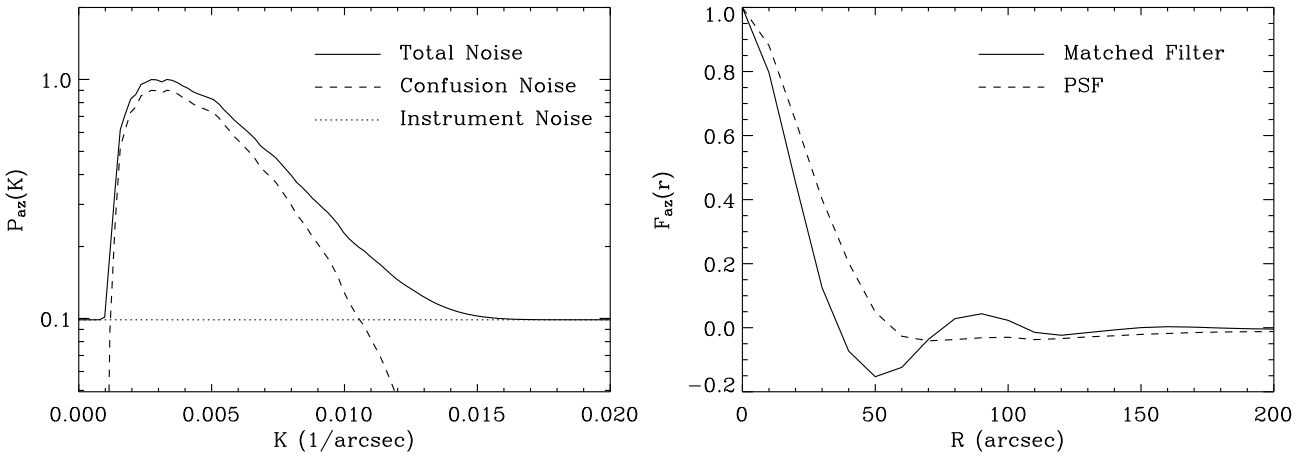

Figure A1. *left:* The peak-normalized total azimuthally averaged 500 μm angular noise power spectrum (solid line) and its two components: instrumental (white) noise (dotted line), and confusion from point sources (dashed line). The latter function has the same shape as the PSF, since point sources are modelled as a spatially unclustered collection of point sources smoothed by the PSF. The roll-off at $K < 0.003$ in the PSF is a result of the spatial whitening filter that has been applied to the BLAST maps (Devlin et al. 2009). *right:* The azimuthally averaged 500 μm matched filter (solid line) compared with the PSF (dashed line), now in angular rather than frequency space. The matched filter is obtained by dividing the power spectrum of the PSF (same shape as the dashed line in the left-hand plot) by the noise power spectrum (solid line in the left-hand plot), and taking the inverse Fourier Transform. For the noise sources considered here, this procedure augments high-frequency components of the PSF, resulting in a narrower central profile, while introducing ringing at angular scales $\gtrsim 50$ arcsec.

a function of S and c, and multiplying by $2\pi r$ converts this quantity to the infinitesimal number density of sources at a distance r from the submm peak.

Therefore, given S, c and r for the jth candidate counterpart to the ith submm peak, the relative number of expected true counterparts to background sources is the LR:

$$L_{i,j} = \frac{n_{\rm c}}{n_{\rm b}} = \frac{q(S_j, c_j) e^{-r_{i,j}^2/2\sigma_{\rm r}^2}}{2\pi\sigma_{\rm r}^2 \rho(S_j, c_j)}. \quad \text{(B4)}$$

Candidates with large values of $L_{i,j}$ are more likely to be associated with the submm emission.

Note that while the LR contains all of the information about the potential identification, it is not itself a probability distribution. In the case that only a single source in the matching catalogue is believed to correspond to the submm peak, and where $q(S, c)$, $\rho(S, c)$, and σ are all known precisely, it is possible to calculate the reliability R, the probability that the candidate is *the unique counterpart*, following Sutherland & Saunders (1992). Using this technique on a case for which there are multiple strong candidate matches, for example, the reliability is divided among them in such a way that their sum does not exceed 1. For the case at hand, since we consider the possibility of multiple real counterparts to a single submm peak, and since our estimates of the priors are ultimately quite noisy, Eq. 5 from Sutherland & Saunders (1992) does not apply. Instead we will take the approach of using Monte Carlo simulations to establish a threshold LR that will provide candidates with a desired false identification rate.

B1 Background Counts and Positional Uncertainties

We estimate priors directly from the data themselves. First, $\rho(S, c)$, the background number counts, are determined by binning the entire matching catalogue (Section 2.2) as a function of the two flux densities and colour, and dividing by the survey area. This should give a good estimate for the average properties of the background sources since the entire catalogue contains 9216 entries, whereas there are only of order ~ 60 submm peaks in each band.

The positional uncertainty parameter, $\sigma_{\rm r}$, is more difficult to estimate from the data. We proceed by counting the number of catalogue sources around submm peaks, and checking for statistically significant excesses compared to the background counts predicted by $\rho(S, c)$, as a function of search radius. The expectation, if each submm peak were produced by a single source in the matching catalogue, is that the cumulative excess would grow from 0 at a search radius of 0, and converge to 1 at large radii.

We show the differential excess distribution (calculated in annuli of different sizes) for each submm band in Fig. B1. Uncertainties for each data point are estimated from Poisson counting statistics (considering both the number of objects in the full catalogue for the uncertainties in the background counts, and the number of objects in the measurement annulus). We fit the Rayleigh radial offset distribution to the excess counts, multiplying the single-parameter expression for $f(r)$ in Eq. B2 by a second parameter, E, giving the integrated excess number of sources around submm peaks (note that $E = \int\int q(S, c)\, dS\, dc$). The smooth models are shown as solid lines in the differential excess plots. In addition, the solid histograms show the models integrated across the same bins as the data, giving the model predictions used to calculate χ^2. Clearly, E is significantly larger than 1 in each submm band, demonstrating that the submm peaks from our survey are typically blends of several sources in the matching catalogue. One could use this approach to determine a criterion which might be called 'counterpart confusion' – for a given source map and catalogue (in a different

waveband) one could conclude that the source identification process will be relatively straightforward if $E < 2$ (say), but significantly complicated by confusion if $E \geqslant 2$.

B2 Flux density and colour priors

Next we estimate the joint distribution of flux density and colour for counterparts, $q(S, c)$. Since we assume that these properties are un-correlated with their distance from the submm centroid, we first identify the search radius within which the SNR of the excess counts is highest, $r_{\rm s}$. As this radius is increased from 0, the background counts grow as $r_{\rm s}^2$, but the counts around submm positions grow even faster as the counterparts are included. The ratio of the difference (the excess), compared to the Poisson uncertainty in the difference, therefore increases until the number of new counterparts drops significantly. We find that for our matching catalogue and submm peaks lists the maximum excess SNR are achieved at 23, 23, 35 and 15 arcsec for 250, 350, 500 and 870 μm, respectively. Using these search radii, we then compare the normalized histogram of 24 μm and 1.4 GHz flux densities for the entire matching catalogues with the normalized histogram of excess sources around submm peaks, $p(S_{24})$ and $p(S_{\rm r})$, in Figs. B2 and B3. This operation shows that the extra sources around submm peaks tend to be *brighter* at 24 μm and 1.4 GHz on average than the entire populations in the BLAST bands.

In a similar way we compare the $\log_{10}(S_{3.6}/S_{4.5})$ colour of the background population to the excess around submm positions. This IRAC colour was chosen because it is the primary discriminator for redshift used in Devlin et al. (2009), Marsden et al. (2009), and Pascale et al. (2009) – with the trend that smaller ratios (i.e. redder colours) correlate with higher redshifts. Earlier studies have also used IRAC colours as a crude redshift estimator (e.g., Pope et al. 2006; Yun et al. 2008; Wilson et al. 2008). The normalized excess colour distribution, $p(c)$ (Fig. B4) agrees with this expectation. There is a trend from bluer colours starting at 250 μm (submm excess and background colours nearly indistinguishable), to significantly redder colours at 500 and 870 micron.

Individually, $p(S_{24})$, $p(S_{\rm r})$, and $p(c)$ give normalized estimates of $q(S_{24}, S_{\rm r}, c)$ marginalized over the remaining variables. If they were completely independent of one another, we could estimate $q(S, c)$ as

$$q(S, c) \simeq E \times p(S_{24})p(S_{\rm r})p(c), \tag{B5}$$

where E is the total excess measured in Fig. B1. Ideally we would like to bin the excess counts in cubes of S_{24}, $S_{\rm r}$, and c simultaneously. Unfortunately, given the sample size, it is not possible to obtain a statistically significant measurement of this distribution. Similarly, we approximate the background counts

$$\rho(S, c) \simeq \rho(S_{24})\rho(S_{\rm r})\rho(c). \tag{B6}$$

We proceed under the assumption that these quantities are independent, but in the next section use Monte Carlo simulations to establish a reasonable threshold for this approximate LR to obtain counterparts.

B3 Normalized LR

Since each submm peak appears to be produced by a blend of several matching catalogue sources, we cannot use the Sutherland & Saunders (1992) reliability, R, as a normalized probability that a given candidate is *the single* counterpart. Furthermore, its absolute normalization depends on precise measurements of $\sigma_{\rm r}$, $\rho(S, c)$ and $q(S, c)$, all of which have moderate uncertainties for this sample (especially $q(S, c)$, as noted in the previous section).

Instead, we compare the LRs for all potential candidate matches to submm peaks, with the distribution of LRs for false matches to 10,000 random positions. This procedure enables us to select a threshold LR that gives an acceptable rate of false-positives, which we set to 10%. This approach to identifying the threshold LR is similar to that of Mann et al. (1997). The results of our calculation are shown in Fig. B5. The solid histogram is the distribution of LR for all matching catalogue sources out to 60 arcsec (this maximum search radius easily contains > 99% of the true counterparts) from each submm position. The dotted histograms show the 'background' distribution obtained by searching for counterparts around random positions. As expected, for large values of the LR, there are more sources around submm peaks than random positions. Also, unsurprisingly, the distinction between the two curves is greatest at 870 μm (which has the smallest positional uncertainties), and progressively worse across the BLAST bands to longer wavelengths.

A threshold in the LR is chosen such that the fraction of sources with *larger* LRs for the simulation (random positions) is 10%. This cut is indicated as a vertical dashed line in Fig. B5. For convenience, we normalize the LRs by these threshold values, so that potential counterparts have values that are greater than 1. Also, noting the ratio of the density of sources around submm and random positions, a candidate counterpart at this threshold is about three times more likely to be real than spurious (this value does *not*, however, reflect on the *absolute* probability that the source is either real or spurious).

The results of applying this cut to potential identifications around submm positions are given in Table B1. For each band the total number of expected counterparts is the product of the number of submm positions with the average excess of matching catalogue sources around each spot. The estimated number of true IDs found is then the number of sources detected above the cut on the LR, after subtracting the 10% spurious fraction. This test shows that as many as 32% of the individual matching catalogue sources contributing to the 870 μm peaks have been identified, and as few as 13% at 500 μm. The trend of this result is certainly expected, due to the increased confusion caused by larger beams. However, the extent of the problem of identifying confused sources is larger than some would have expected.

APPENDIX C: DATA TABLES

The following data tables are provided in this Appendix: the match-filtered submm peak lists in the BLAST bands (Tables C1-C3), as well as the LESS peaks from Weiss et al. (2009) that land within the region that was analyzed (Table C4); the correspondence between the matching catalogue

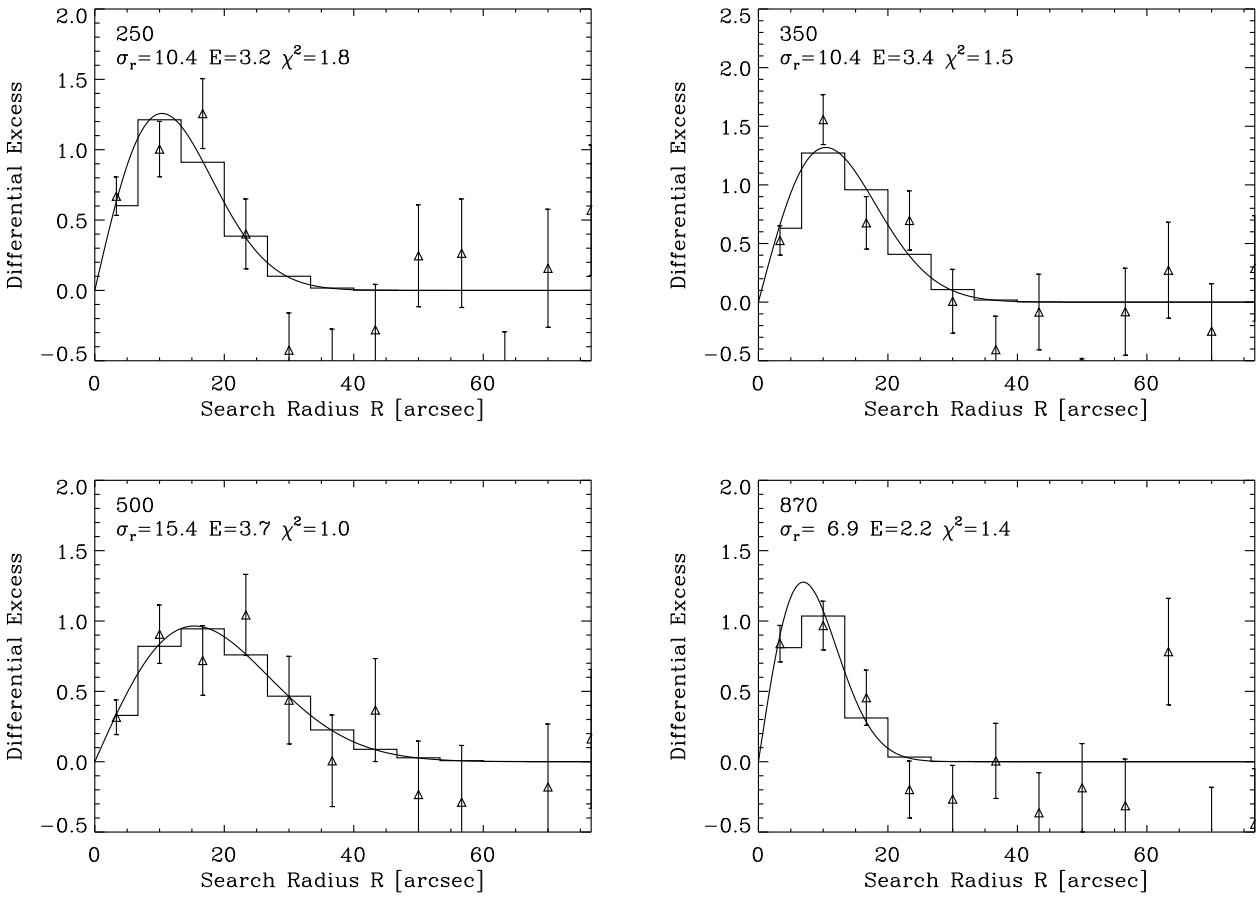

Figure B1. Excess source counts in annuli around submm peaks compared to the expected background as a function of search radius. Poisson uncertainties are plotted. The solid lines are fits of a Gaussian radial probability density function $p(r) = (Er/\sigma_r)\exp(-r^2/2\sigma_r^2)$, where the scale factor E is the total excess counts encountered on average (fit values are indicated in each panel). This function is fit to the differential excess counts (since the uncertainties are uncorrelated). The histograms in the differential plots show the smooth model integrated across each bin (giving the actual predicted model values used to calculate χ_r^2).

Table B1. Excess count and ID statistics. The number of peaks are from the BLAST and LESS catalogues, using 3.75σ and 3.72σ thresholds, respectively. The excess counts per source and σ_r are the best-fit positional uncertainty model parameters (with χ_r^2 giving the reduced chi-squared in each case) – see Section B1. The fact that the excesses are greater than 1 is an indication of how confused the data are, and a warning that finding single counterparts is challenging. Expected numbers of IDs are calculated from the product of the number of submm peaks with the average excesses per source. 'Found IDs' are the total number of potential counterparts with false-identification rates of 10% in the matching catalogue. The 'Real ID' rate subtracts the expected number of false IDs for the list (10% of the number of submm peaks; see discussion of threshold LR values in Section 3), and also expresses that quantity as a percentage of the total expected.

λ (μm)	Peaks (#)	Excess (per peak)	σ_r (arcsec)	χ_r^2	Expected IDs (#)	Found IDs (#)	Real IDs (#)
250	64	3.2	10.4	1.8	204.8	52	45.6 (22%)
350	67	3.4	10.4	1.5	227.8	50	43.3 (19%)
500	55	3.7	15.4	1.0	203.5	31	25.5 (13%)
870	81†	2.2	6.9	1.8	178.2	66	57.9 (32%)

†There are 81 peaks from LESS that land in the region of coverage considered here, but only 42 peaks are cross-matched to the BLAST peak lists. The full list of 81 peaks is used to estimate priors even though we only discuss the properties of the smaller subset of cross-matched peaks in this paper.

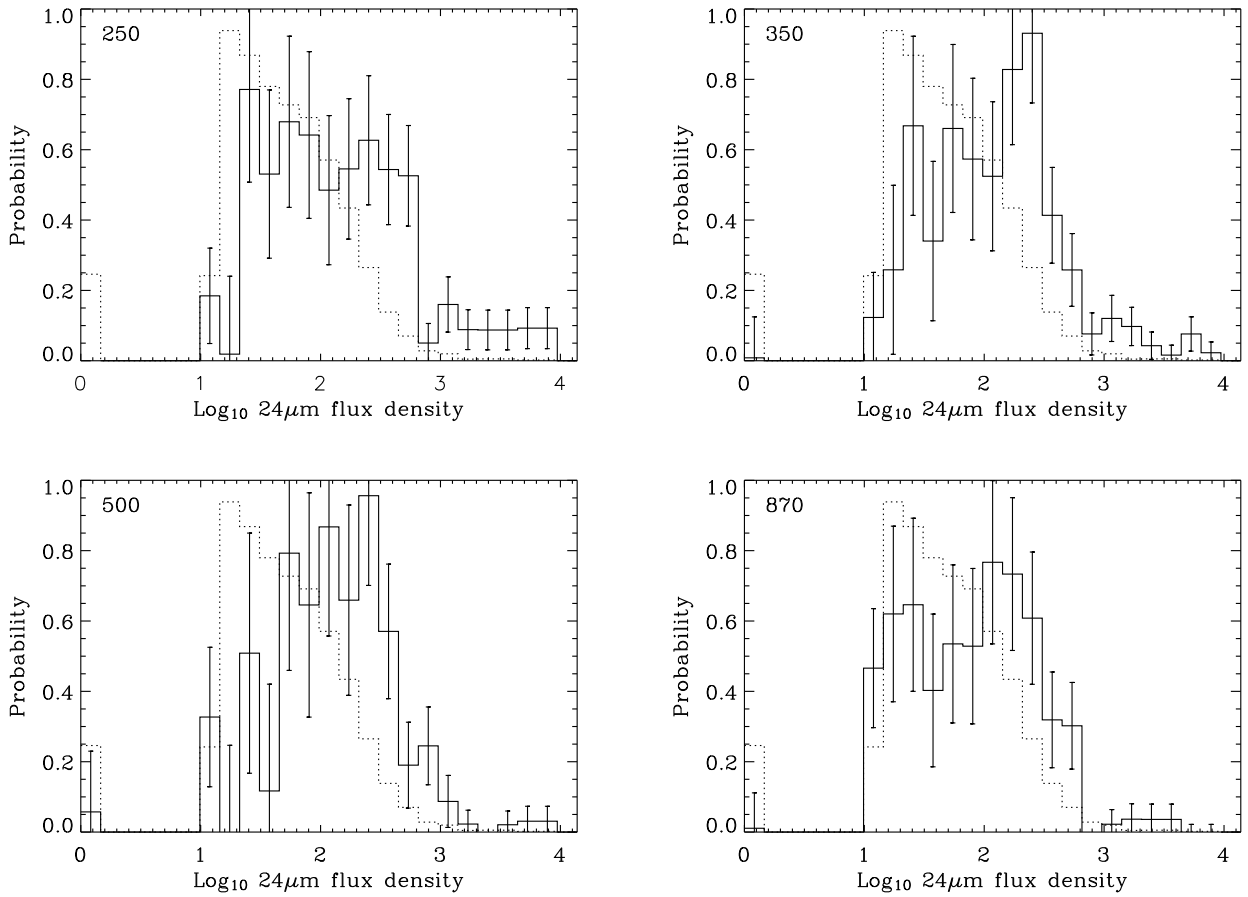

Figure B2. MIPS 24 μm flux density distributions of excess sources around submm peaks in all four bands (solid histogram with Poisson uncertainties), our estimate of $p(S_{24})$, compared to the general population (dotted histogram), our estimate of $\rho(S_{24})$. The bin at 0 contains all radio sources that are not present in the FIDEL 24 μm catalogue. Galaxies selected near submm positions are on average brighter at 24 μm than galaxies selected randomly, and this is true for all four bands.

and each of the submm lists (Tables C5); and the properties of the matched sources (re-measured submm flux densities, SED fits and redshifts, Table C6).

APPENDIX D: POSTAGE STAMPS

This Appendix contains submm, IRAC and radio postage stamps for all 118 proposed identifications to the submm peaks (Fig. D1).

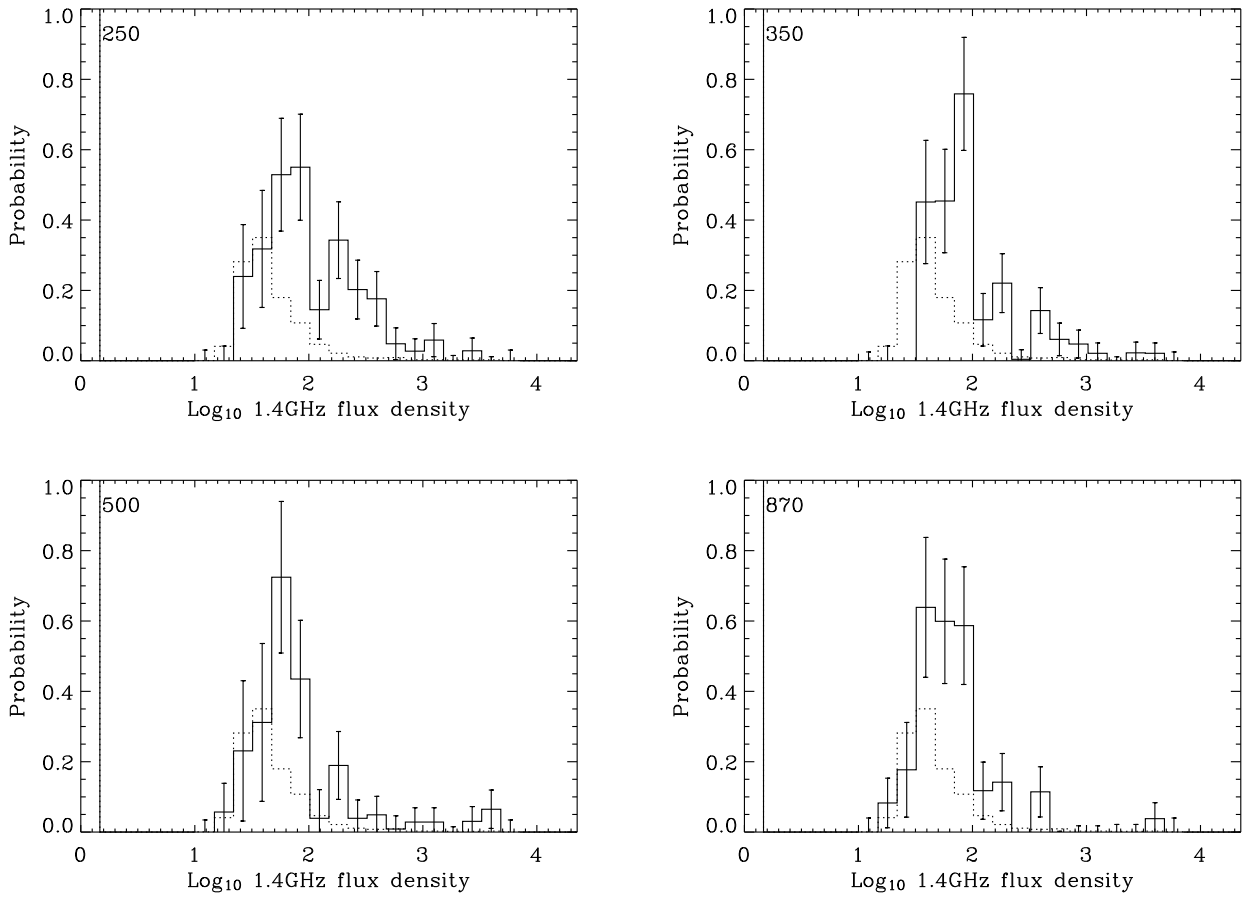

Figure B3. VLA 1.4 GHz flux density distributions of excess sources around submm peaks in all four bands (solid histogram with Poisson uncertainties), our estimate of $p(S_{1.4})$, compared to the general population (dotted histogram), our estimate of $\rho(S_{1.4})$. The bin at 0 contains all 24 μm FIDEL sources that do not exhibit significant radio flux. Galaxies selected near submm positions are on average brighter at 1.4 GHz than galaxies selected randomly, and this is true for all four bands. We also note that many more of the radio sources with 24 μm emission are found near submm positions than random radio sources. Many of these radio sources without 24 μm emission could be spurious given the low significance cut on the catalogue that has been used (see Section 2.2.2). Our prior estimation procedure will give much greater weight to potential radio identifications that also exhibit 24 μm emission.

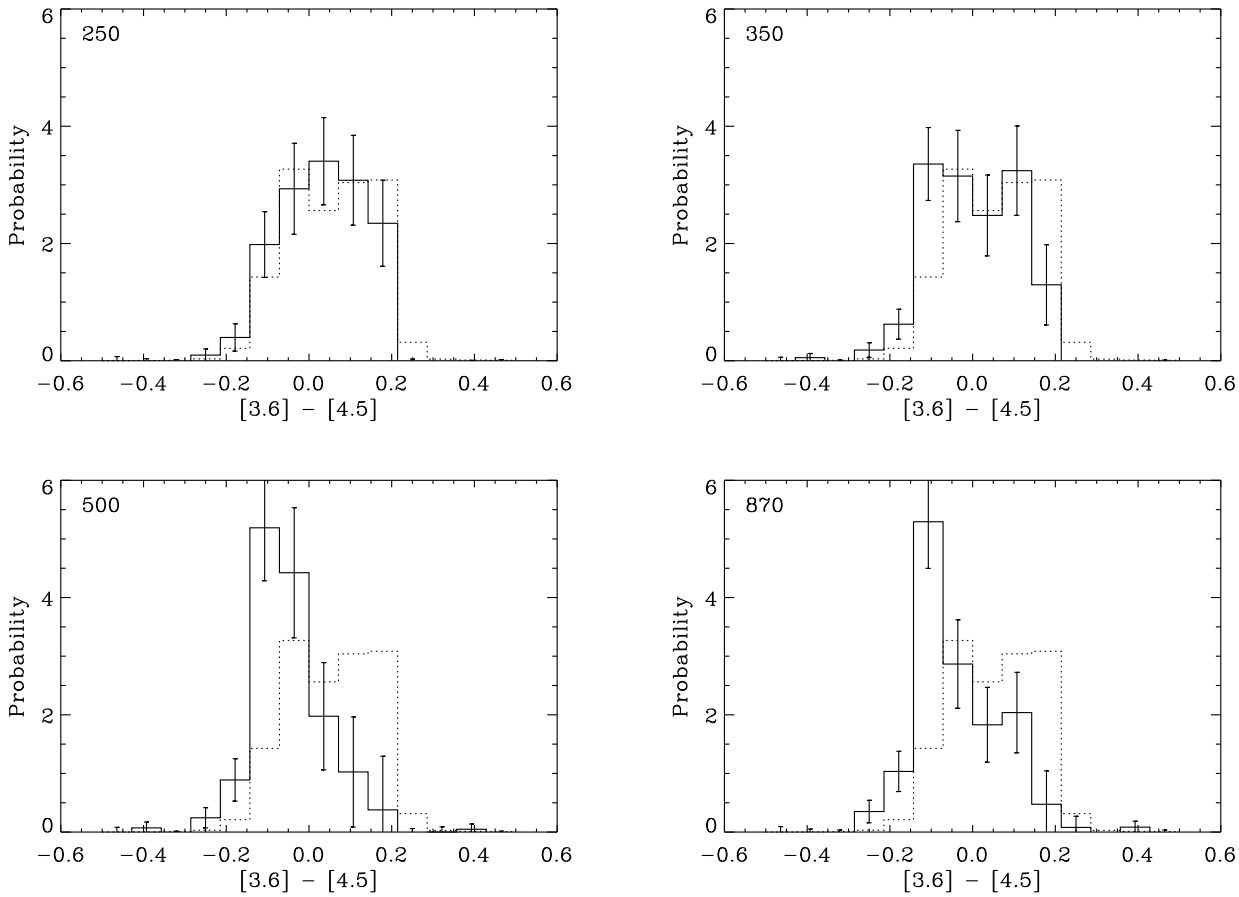

Figure B4. IRAC $\log_{10}(S_{3.6}/S_{4.5})$ colour distributions of excess matching catalogue sources around submm positions in all four bands (solid histogram with Poisson uncertainties), our estimate of $p(c)$, compared to the general population (dotted histogram), our estimate of $\rho(c)$. There is a clear trend of redder colours in the IRAC bands for galaxies selected at longer submm wavelengths.

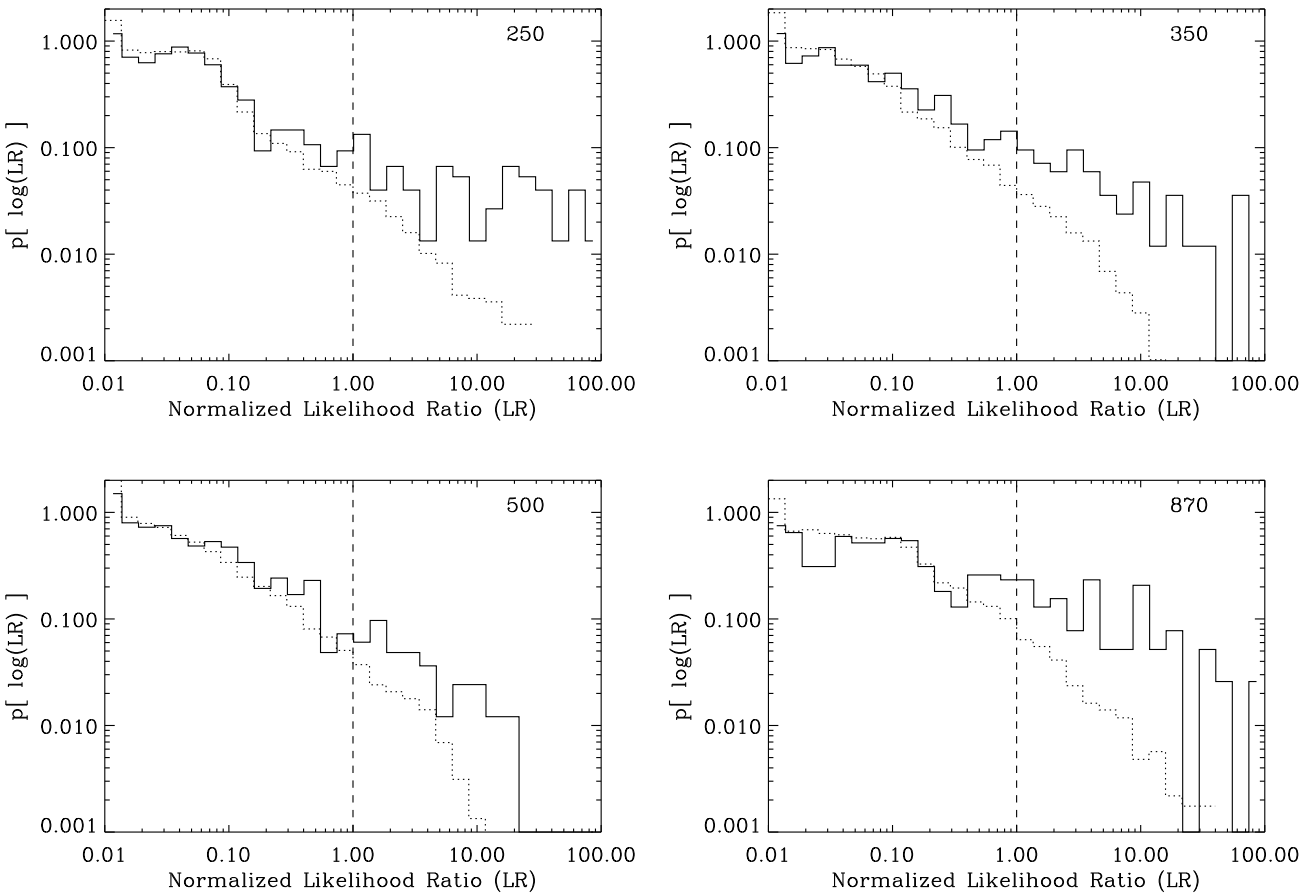

Figure B5. Distribution of likelihood ratios (LR) for potential counterparts in the matching catalogue out to 60 arcsec from submm peak positions (solid histograms) compared to random positions (dotted histograms). Thresholds for identifying potential counterparts are given by the vertical dashed lines, such that the integrated tail of the distribution for random positions gives a false positive rate of 10%. All LRs are normalized to this value (i.e., potential IDs with LR > 1.00 have less than a 10% chance of being false).

Table C1. 250 μm peak list produced from matched-filtered maps that land within the coverage of the matching catalogue (Figure 2). On average, each of these peaks is a blend of 3.2 sources from our matching catalogue. The 'Previously Published Name' is taken from the supplement to Devlin et al. (2009) when available (new peaks have no entry in this column), but the short submm 'SID' is used throughout this paper. The 'Match' column refers to IDs in Table C5. The positions are centroids of the submm peaks. The flux densities are raw values from the maps (with no correction for flux boosting), and the noises and SNR refer to instrumental noise only (excluding source confusion).

SID 250	Previously Published Name	Match ID	R.A. (h m s)	Dec. (° ′ ″)	Flux Density (mJy)	SNR
3	BLAST J033235−275530 (250μm)	66	03 32 34.99	−27 55 31.1	196 ± 14	13.93
5	BLAST J033229−274414 (250μm)	61,62	03 32 29.66	−27 44 16.3	162 ± 13	11.62
16	BLAST J033129−275722 (250μm)	10,11	03 31 29.94	−27 57 24.1	112 ± 14	7.93
17	BLAST J033249−275842 (250μm)	86	03 32 49.32	−27 58 41.5	104 ± 14	7.41
24	BLAST J033246−275744 (250μm)	81	03 32 46.05	−27 57 45.0	99 ± 14	7.11
27	BLAST J033258−274322 (250μm)	92	03 32 58.31	−27 43 24.9	97 ± 14	6.79
32	BLAST J033145−274635 (250μm)	26	03 31 45.37	−27 46 36.6	87 ± 14	6.21
36	BLAST J033145−275730 (250μm)	27	03 31 45.86	−27 57 29.0	84 ± 14	5.96
38	BLAST J033217−275905 (250μm)	52,53	03 32 17.07	−27 59 06.9	83 ± 14	5.91
45	BLAST J033221−275630 (250μm)	57	03 32 21.77	−27 56 26.0	79 ± 14	5.65
51	BLAST J033152−273931 (250μm)	34,35	03 31 52.57	−27 39 33.1	76 ± 14	5.40
52	BLAST J033308−274805 (250μm)	100,101,102	03 33 08.62	−27 48 04.5	74 ± 13	5.37
54	BLAST J033318−274610 (250μm)	111,112	03 33 17.83	−27 46 08.5	74 ± 14	5.32
57	BLAST J033145−274205 (250μm)	25	03 31 44.99	−27 42 06.4	74 ± 14	5.19
58	BLAST J033218−275216 (250μm)	55,56	03 32 18.01	−27 52 18.7	72 ± 14	5.16
59	BLAST J033149−274335 (250μm)	30	03 31 49.74	−27 43 34.7	72 ± 14	5.14
60	BLAST J033241−273818 (250μm)	74,75	03 32 41.87	−27 38 17.9	72 ± 14	5.06
67	BLAST J033319−275423 (250μm)	116	03 33 19.03	−27 54 23.7	70 ± 14	4.98
69	BLAST J033237−273527 (250μm)	70,71	03 32 37.78	−27 35 43.6	69 ± 14	4.95
70	BLAST J033135−273933 (250μm)	12	03 31 35.75	−27 39 44.2	70 ± 14	4.94
72	BLAST J033316−275043 (250μm)	109	03 33 16.20	−27 50 39.6	68 ± 13	4.94
75	BLAST J033205−274645 (250μm)	43	03 32 05.14	−27 46 45.6	68 ± 14	4.91
78		1	03 31 27.89	−27 44 49.5	68 ± 14	4.86
80	BLAST J033128−273916 (250μm)	4,5	03 31 29.06	−27 39 05.2	68 ± 14	4.81
82	BLAST J033243−273919 (250μm)	78	03 32 43.61	−27 39 20.5	67 ± 14	4.79
85	BLAST J033141−274439 (250μm)	19,20	03 31 41.15	−27 44 38.0	67 ± 14	4.75
91	BLAST J033223−273642 (250μm)	59	03 32 22.81	−27 36 43.4	66 ± 14	4.72
92	BLAST J033140−275633 (250μm)	18	03 31 40.33	−27 56 36.3	66 ± 14	4.70
93	BLAST J033211−275859 (250μm)		03 32 11.86	−27 59 00.8	66 ± 14	4.70
97	BLAST J033222−280019 (250μm)	58	03 32 22.14	−28 00 21.1	65 ± 13	4.66
99	BLAST J033129−275910 (250μm)	9	03 31 29.19	−27 59 11.1	66 ± 14	4.64
111	BLAST J033130−275604 (250μm)	7,8	03 31 29.99	−27 56 02.1	63 ± 14	4.53
112		63	03 32 29.95	−27 43 14.4	64 ± 14	4.52
113	BLAST J033235−274932 (250μm)	67	03 32 35.24	−27 49 28.2	62 ± 13	4.51
121	BLAST J033230−275905 (250μm)	64	03 32 30.17	−27 59 05.9	63 ± 14	4.44
130	BLAST J033259−273535 (250μm)	93	03 32 59.71	−27 35 33.4	61 ± 14	4.37
146	BLAST J033151−274431 (250μm)	31,32	03 31 51.13	−27 44 38.1	60 ± 13	4.29
151	BLAST J033147−274147 (250μm)		03 31 47.89	−27 41 41.2	60 ± 14	4.27
154			03 32 06.88	−27 38 00.7	60 ± 14	4.25
178	BLAST J033232−275304 (250μm)		03 32 33.03	−27 53 04.8	59 ± 14	4.18
185	BLAST J033317−274118 (250μm)	110	03 33 17.38	−27 41 12.5	59 ± 14	4.15
188	BLAST J033154−274406 (250μm)	37	03 31 54.28	−27 44 04.2	58 ± 14	4.15
210	BLAST J033135−274705 (250μm)		03 31 35.03	−27 47 09.1	57 ± 14	4.09
222	BLAST J033200−280234 (250μm)		03 32 00.67	−28 02 32.1	57 ± 14	4.06
226			03 31 29.94	−27 39 41.9	58 ± 14	4.05
235	BLAST J033156−280306 (250μm)		03 31 56.85	−28 03 09.4	57 ± 14	4.03
244		17	03 31 39.58	−27 41 29.5	56 ± 14	4.00
246	BLAST J033211−280242 (250μm)	45	03 32 11.14	−28 02 42.6	56 ± 14	4.00
250	BLAST J033251−274530 (250μm)		03 32 51.55	−27 45 33.3	56 ± 14	3.99
255	BLAST J033144−275521 (250μm)	24	03 31 44.76	−27 55 19.5	55 ± 13	3.98

SID 250	Previously Published Name	Match ID	R.A. (h m s)	Dec. (° ′ ″)	Flux Density (mJy)	SNR
279	BLAST J033311−274313 (250μm)		03 33 11.13	−27 43 12.0	56 ± 14	3.93
289	BLAST J033217−275054 (250μm)	54	03 32 17.43	−27 50 55.7	54 ± 13	3.91
298	BLAST J033243−275146 (250μm)	79,80	03 32 43.50	−27 51 45.6	54 ± 14	3.89
312	BLAST J033228−273545 (250μm)		03 32 28.66	−27 35 53.0	54 ± 14	3.86
316	BLAST J033238−275651 (250μm)	72	03 32 37.99	−27 56 57.6	53 ± 13	3.86
325	BLAST J033225−273822 (250μm)	60	03 32 24.97	−27 38 22.2	54 ± 14	3.84
328	BLAST J033205−280054 (250μm)	42	03 32 05.54	−28 00 54.2	53 ± 13	3.84
348	BLAST J033150−275100 (250μm)		03 31 50.24	−27 51 11.0	53 ± 13	3.81
354	BLAST J033248−274443 (250μm)		03 32 47.55	−27 44 58.3	53 ± 14	3.80
358	BLAST J033210−274253 (250μm)	47	03 32 10.51	−27 42 55.3	53 ± 14	3.80
369		87	03 32 49.09	−27 36 19.7	53 ± 14	3.78
378	BLAST J033131−274601 (250μm)		03 31 31.77	−27 46 05.1	52 ± 14	3.76
381	BLAST J033311−275226 (250μm)		03 33 11.65	−27 52 27.0	52 ± 13	3.76
389	BLAST J033251−275936 (250μm)	88	03 32 51.85	−27 59 40.9	53 ± 14	3.75

Table C2. 350 μm peak list produced from matched-filtered maps. Columns have the same meaning as in Table C1. On average, each of these peaks is a blend of 3.4 sources from our matching catalogue.

SID 350	Previously Published Name	Match ID	R.A. (h m s)	Dec. (° ′ ″)	Flux Density (mJy)	SNR
3	BLAST J033234−275531 (350μm)	66	03 32 34.88	−27 55 31.3	89 ± 10	8.24
7	BLAST J033249−275833 (350μm)	86	03 32 49.49	−27 58 33.8	79 ± 10	7.36
8	BLAST J033229−274414 (350μm)	61,62	03 32 29.37	−27 44 16.4	74 ± 10	6.95
10	BLAST J033220−275647 (350μm)		03 32 20.15	−27 56 45.4	73 ± 10	6.82
11	BLAST J033258−274328 (350μm)	92	03 32 58.39	−27 43 25.0	72 ± 10	6.73
12	BLAST J033229−274305 (350μm)	63	03 32 29.49	−27 43 03.4	71 ± 10	6.72
14	BLAST J033328−275700 (350μm)	118	03 33 27.65	−27 57 03.4	72 ± 10	6.66
16	BLAST J033129−275722 (350μm)	10,11	03 31 29.61	−27 57 22.6	70 ± 11	6.41
19	BLAST J033204−274650 (350μm)	43	03 32 04.59	−27 46 51.7	67 ± 10	6.35
20	BLAST J033207−275815 (350μm)	44	03 32 07.34	−27 58 18.1	68 ± 10	6.30
22	BLAST J033128−273927 (350μm)	2,3,4	03 31 28.02	−27 39 32.2	71 ± 11	6.25
31	BLAST J033311−274135 (350μm)	105	03 33 11.16	−27 41 32.5	64 ± 10	5.95
34	BLAST J033247−274224 (350μm)	83	03 32 47.24	−27 42 31.9	62 ± 10	5.86
35	BLAST J033150−274333 (350μm)	30	03 31 49.77	−27 43 28.2	63 ± 10	5.84
37	BLAST J033140−274435 (350μm)	19,20	03 31 40.71	−27 44 36.9	62 ± 10	5.76
42	BLAST J033138−274122 (350μm)	17	03 31 39.04	−27 41 22.3	60 ± 10	5.67
43	BLAST J033318−274606 (350μm)	111,112	03 33 18.39	−27 46 13.4	60 ± 10	5.64
45	BLAST J033210−275206 (350μm)	46	03 32 11.53	−27 52 03.8	61 ± 10	5.62
47	BLAST J033151−274428 (350μm)	31,32	03 31 51.20	−27 44 33.4	59 ± 10	5.56
49	BLAST J033135−275448 (350μm)	13,14,15	03 31 35.44	−27 54 47.5	60 ± 10	5.56
52	BLAST J033252−273756 (350μm)		03 32 52.12	−27 37 47.9	58 ± 10	5.36
58	BLAST J033321−275513 (350μm)	117	03 33 21.74	−27 55 13.1	56 ± 10	5.19
64	BLAST J033302−275640 (350μm)	95	03 33 02.20	−27 56 43.7	54 ± 10	5.05
65	BLAST J033218−275207 (350μm)	55,56	03 32 18.12	−27 52 12.5	54 ± 10	5.03
69	BLAST J033237−273541 (350μm)	70,71	03 32 37.62	−27 35 42.4	54 ± 11	4.96
79	BLAST J033307−275833 (350μm)		03 33 06.98	−27 58 35.5	52 ± 10	4.84
80	BLAST J033217−275906 (350μm)	53	03 32 17.78	−27 59 20.2	52 ± 10	4.83
84	BLAST J033318−274131 (350μm)		03 33 19.72	−27 41 38.7	52 ± 10	4.79
85	BLAST J033230−275905 (350μm)	64	03 32 30.00	−27 59 02.4	51 ± 10	4.79
88	BLAST J033211−273731 (350μm)	49	03 32 11.34	−27 37 24.1	51 ± 10	4.76
90	BLAST J033253−280107 (350μm)	89	03 32 53.05	−28 01 11.3	51 ± 10	4.76
91	BLAST J033321−273908 (350μm)		03 33 21.00	−27 39 10.0	51 ± 10	4.75
92	BLAST J033308−275130 (350μm)	104	03 33 08.61	−27 51 29.3	50 ± 10	4.74
93	BLAST J033153−274952 (350μm)	36	03 31 54.84	−27 49 37.7	51 ± 10	4.73
95	BLAST J033152−280325 (350μm)	33	03 31 53.14	−28 03 35.7	51 ± 10	4.72
98		108	03 33 15.41	−27 45 32.9	50 ± 10	4.69
108	BLAST J033215−273929 (350μm)	51	03 32 15.25	−27 39 31.8	50 ± 10	4.62
112	BLAST J033316−275056 (350μm)	109	03 33 17.16	−27 50 55.7	48 ± 10	4.60
115	BLAST J033305−274414 (350μm)	96	03 33 06.26	−27 44 14.1	49 ± 10	4.59
116	BLAST J033245−275739 (350μm)	81	03 32 46.04	−27 57 35.2	49 ± 10	4.59
117	BLAST J033134−274629 (350μm)		03 31 34.56	−27 46 25.9	49 ± 10	4.57
124	BLAST J033153−273931 (350μm)	34,35	03 31 52.62	−27 39 29.9	49 ± 10	4.54
128	BLAST J033243−275509 (350μm)	76,77	03 32 42.86	−27 55 13.1	48 ± 10	4.51
137	BLAST J033217−275906 (350μm)	52	03 32 17.89	−27 58 46.5	47 ± 10	4.44
144	BLAST J033152−275035 (350μm)		03 31 51.22	−27 50 41.8	46 ± 10	4.40
145	BLAST J033308−274813 (350μm)	100,101,103	03 33 08.49	−27 48 16.5	47 ± 10	4.40
152	BLAST J033145−274153 (350μm)		03 31 44.98	−27 41 50.5	46 ± 10	4.32
154	BLAST J033238−274620 (350μm)		03 32 38.52	−27 46 18.5	46 ± 10	4.32
161	BLAST J033212−275459 (350μm)		03 32 12.74	−27 54 59.1	45 ± 10	4.29
169	BLAST J033225−273810 (350μm)	60	03 32 24.93	−27 38 17.3	46 ± 10	4.25

SID 350	Previously Published Name	Match ID	R.A. (^{h} ^{m} ^{s})	Dec. ($^\circ$ $'$ $''$)	Flux Density (mJy)	SNR
170	BLAST J033201−274142 (350μm)	41	03 32 02.02	−27 41 38.0	45 ± 10	4.25
177	BLAST J033129−275911 (350μm)	9	03 31 29.63	−27 59 09.1	46 ± 10	4.22
184			03 32 10.66	−27 58 56.9	45 ± 10	4.21
187	BLAST J033141−275529 (350μm)	23	03 31 41.76	−27 55 28.4	44 ± 10	4.18
188	BLAST J033147−274755 (350μm)	28	03 31 47.60	−27 47 52.9	45 ± 10	4.18
199	BLAST J033217−275407 (350μm)		03 32 17.92	−27 54 08.0	44 ± 10	4.13
235	BLAST J033127−274430 (350μm)	1	03 31 27.90	−27 44 32.8	43 ± 10	4.04
259	BLAST J033235−280135 (350μm)	68,69	03 32 35.90	−28 01 48.7	42 ± 10	3.97
264	BLAST J033210−275612 (350μm)		03 32 11.27	−27 56 12.1	42 ± 10	3.96
273	BLAST J033234−280043 (350μm)		03 32 34.46	−28 00 36.3	42 ± 10	3.94
276	BLAST J033313−273709 (350μm)		03 33 13.26	−27 37 14.9	43 ± 10	3.93
291	BLAST J033136−274933 (350μm)		03 31 36.08	−27 49 40.9	41 ± 10	3.89
298	BLAST J033312−275611 (350μm)	106,107	03 33 13.37	−27 56 04.2	41 ± 10	3.88
317			03 32 29.08	−28 01 53.8	41 ± 10	3.84
322	BLAST J033148−280212 (350μm)	29	03 31 48.41	−28 02 20.9	41 ± 10	3.83
340	BLAST J033132−274314 (350μm)		03 31 32.37	−27 43 16.5	41 ± 10	3.80
362			03 33 04.96	−27 37 26.0	40 ± 10	3.76

Table C3. 500 μm peak list produced from matched-filtered maps. Columns have the same meaning as in Table C1. On average, each of these peaks is a blend of 3.7 sources from our matching catalogue.

SID 500	Previously Published Name	Match ID	R.A. (h m s)	Dec. (° ′ ″)	Flux Density (mJy)	SNR
5	BLAST J033328−275659 (500μm)	118	03 33 28.17	−27 56 57.0	62 ± 8	7.43
7	BLAST J033311−275610 (500μm)	106	03 33 11.77	−27 56 11.2	56 ± 8	6.81
8	BLAST J033207−275811 (500μm)	44	03 32 08.12	−27 58 05.0	53 ± 8	6.51
9	BLAST J033129−275545 (500μm)	6,7,8	03 31 29.24	−27 55 49.0	53 ± 8	6.41
11	BLAST J033128−275713 (500μm)	10,11	03 31 29.51	−27 57 22.0	53 ± 8	6.28
12	BLAST J033258−274325 (500μm)	92	03 32 58.68	−27 43 27.9	52 ± 8	6.26
13	BLAST J033215−275027 (500μm)		03 32 15.44	−27 50 30.6	49 ± 8	6.08
14	BLAST J033153−273921 (500μm)	34,35	03 31 52.05	−27 39 21.8	50 ± 8	6.08
17	BLAST J033128−273942 (500μm)	2,3,4	03 31 28.18	−27 39 42.3	53 ± 8	6.01
20	BLAST J033256−280102 (500μm)	91	03 32 56.40	−28 01 05.4	48 ± 8	5.84
21	BLAST J033217−275212 (500μm)	55,56	03 32 18.29	−27 52 12.7	47 ± 8	5.74
23	BLAST J033321−275510 (500μm)	117	03 33 22.24	−27 55 14.4	47 ± 8	5.70
24	BLAST J033318−274926 (500μm)	113,114,115	03 33 17.67	−27 49 26.6	46 ± 8	5.67
26		70,71	03 32 37.60	−27 35 31.5	46 ± 8	5.61
31	BLAST J033220−275631 (500μm)	57	03 32 20.86	−27 56 26.3	43 ± 8	5.27
33	BLAST J033212−275558 (500μm)	50	03 32 13.11	−27 56 03.4	43 ± 8	5.24
35	BLAST J033156−274511 (500μm)		03 31 58.33	−27 45 13.5	42 ± 8	5.20
37	BLAST J033249−274227 (500μm)	83,84,85	03 32 47.94	−27 42 25.3	43 ± 8	5.14
41	BLAST J033253−273759 (500μm)	90	03 32 52.93	−27 37 59.7	41 ± 8	5.05
43	BLAST J033301−275625 (500μm)		03 33 00.48	−27 56 08.5	41 ± 8	5.05
44	BLAST J033309−275125 (500μm)	104	03 33 09.35	−27 51 20.1	41 ± 8	5.05
48	BLAST J033135−275448 (500μm)	13,14,15,16	03 31 36.29	−27 54 42.9	41 ± 8	4.99
53	BLAST J033229−274426 (500μm)	61,62	03 32 29.05	−27 44 30.6	41 ± 8	4.96
56	BLAST J033235−275518 (500μm)	66	03 32 35.23	−27 55 14.6	41 ± 8	4.91
57		108	03 33 14.92	−27 45 32.0	40 ± 8	4.90
58	BLAST J033210−273725 (500μm)	49	03 32 10.34	−27 37 20.0	40 ± 8	4.87
64	BLAST J033129−275918 (500μm)	9	03 31 29.49	−27 59 14.7	41 ± 8	4.77
68	BLAST J033211−275210 (500μm)	46	03 32 10.34	−27 51 54.0	39 ± 8	4.74
84	BLAST J033253−274459 (500μm)		03 32 54.41	−27 44 52.3	37 ± 8	4.58
88	BLAST J033153−274943 (500μm)		03 31 52.34	−27 49 27.5	38 ± 8	4.57
91	BLAST J033213−274302 (500μm)	48	03 32 13.32	−27 43 01.3	38 ± 8	4.55
103			03 32 34.40	−27 50 17.3	36 ± 8	4.43
104	BLAST J033229−274314 (500μm)	63	03 32 29.47	−27 43 08.2	36 ± 8	4.42
109	BLAST J033256−274539 (500μm)		03 32 56.26	−27 45 49.6	35 ± 8	4.37
128	BLAST J033318−274115 (500μm)		03 33 19.16	−27 41 15.3	35 ± 8	4.28
133	BLAST J033238−275638 (500μm)	72	03 32 38.87	−27 56 44.9	35 ± 8	4.26
137	BLAST J033323−274900 (500μm)		03 33 23.47	−27 48 53.7	35 ± 8	4.26
144		86	03 32 49.97	−27 58 33.2	35 ± 8	4.24
156	BLAST J033137−273743 (500μm)		03 31 37.89	−27 37 30.7	36 ± 8	4.16
157	BLAST J033157−275930 (500μm)	40	03 31 56.89	−27 59 26.3	34 ± 8	4.15
162	BLAST J033143−274817 (500μm)	22	03 31 43.92	−27 48 19.2	33 ± 8	4.14
176	BLAST J033300−274852 (500μm)	94	03 32 59.71	−27 48 53.8	32 ± 8	4.06
177		29	03 31 48.34	−28 02 03.3	34 ± 8	4.06
191			03 32 13.32	−27 59 08.4	33 ± 8	4.03
199	BLAST J033247−275415 (500μm)	82	03 32 47.54	−27 54 14.0	33 ± 8	4.01
200		98	03 33 06.56	−28 00 46.8	33 ± 8	4.01
202	BLAST J033154−275343 (500μm)	38,39	03 31 54.94	−27 53 35.8	33 ± 8	4.00
203	BLAST J033215−275901 (500μm)	52	03 32 17.57	−27 58 46.5	33 ± 8	4.00
205	BLAST J033153−274943 (500μm)	36	03 31 54.51	−27 49 43.2	33 ± 8	3.99
210		42	03 32 06.41	−28 01 07.1	32 ± 8	3.97
222	BLAST J033309−275347 (500μm)	97	03 33 09.20	−27 54 00.5	32 ± 8	3.94
223	BLAST J033222−274555 (500μm)		03 32 22.75	−27 45 52.9	31 ± 8	3.93
248	BLAST J033145−274148 (500μm)		03 31 46.11	−27 41 44.2	31 ± 8	3.87
250	BLAST J033235−274931 (500μm)	67	03 32 35.56	−27 49 04.7	32 ± 8	3.87
253	BLAST J033307−274001 (500μm)		03 33 07.81	−27 39 36.2	32 ± 8	3.86
261	BLAST J033148−280315 (500μm)		03 31 49.06	−28 03 13.2	31 ± 8	3.84
267	BLAST J033243−273914 (500μm)	78	03 32 43.67	−27 39 38.1	31 ± 8	3.83

Table C4. 870 μm peaks from Weiss et al. (2009) that land within the coverage of the matching catalogue. The columns have the same meaning as in Table C1, although the SNR is measured with respect to the combined instrumental and confusion noise. On average, each of these peaks is a blend of 2.2 sources in our matching catalogue. In addition, the 33 peaks marked with an asterisk in the 'Match ID' column have no matches in any of the BLAST peak catalogues (Tables C1-C3). These peaks are used to measure priors, but are not otherwise analyzed in this paper.

SID 870	Previously Published Name	Match ID	R.A. (h m s)	Dec. (° ′ ″)	Flux Density (mJy)	SNR
1	LESS J033314.3−275611	107	03 33 14.26	−27 56 11.2	14.7 ± 1.2	12.48
2	LESS J033302.5−275643	95	03 33 02.50	−27 56 43.6	12.2 ± 1.2	10.31
3	LESS J033321.5−275520	117	03 33 21.51	−27 55 20.2	11.9 ± 1.2	10.12
4	LESS J033136.0−275439	13,14,15	03 31 36.01	−27 54 39.2	11.2 ± 1.1	9.72
5	LESS J033129.5−275907	9	03 31 29.46	−27 59 07.3	10.1 ± 1.2	8.45
6	LESS J033257.1−280102	91	03 32 57.14	−28 01 02.1	9.8 ± 1.2	8.16
7	LESS J033315.6−274523	108	03 33 15.55	−27 45 23.6	9.4 ± 1.2	7.89
9	LESS J033211.3−275210	46	03 32 11.29	−27 52 10.4	9.4 ± 1.2	7.71
10	LESS J033219.0−275219	56	03 32 19.02	−27 52 19.4	9.3 ± 1.2	7.60
11	LESS J033213.6−275602	50	03 32 13.58	−27 56 02.5	9.2 ± 1.2	7.58
12	LESS J033248.1−275414	82	03 32 48.12	−27 54 14.7	8.9 ± 1.2	7.24
13	LESS J033249.2−274246	84,85	03 32 49.23	−27 42 46.6	8.9 ± 1.2	7.21
14	LESS J033152.6−280320	33	03 31 52.64	−28 03 20.4	9.5 ± 1.3	7.19
16	LESS J033218.9−273738	*	03 32 18.89	−27 37 38.7	8.2 ± 1.2	6.87
17	LESS J033207.6−275123	*	03 32 07.59	−27 51 23.0	7.8 ± 1.2	6.36
18	LESS J033205.1−274652	43	03 32 05.12	−27 46 52.1	7.7 ± 1.2	6.30
19	LESS J033208.1−275818	44	03 32 08.10	−27 58 18.7	7.5 ± 1.2	6.19
20	LESS J033316.6−280018	*	03 33 16.56	−28 00 18.8	7.5 ± 1.2	6.15
25	LESS J033157.1−275940	40	03 31 57.05	−27 59 40.8	7.0 ± 1.2	5.83
26	LESS J033136.9−275456	15,16	03 31 36.90	−27 54 56.1	6.8 ± 1.2	5.80
28	LESS J033302.9−274432	*	03 33 02.92	−27 44 32.6	7.0 ± 1.2	5.62
31	LESS J033150.0−275743	*	03 31 49.96	−27 57 43.9	6.7 ± 1.2	5.51
32	LESS J033243.6−274644	*	03 32 43.57	−27 46 44.0	6.8 ± 1.2	5.46
33	LESS J033149.8−275332	*	03 31 49.78	−27 53 32.9	6.8 ± 1.2	5.46
34	LESS J033217.6−275230	55	03 32 17.64	−27 52 30.3	6.8 ± 1.2	5.40
36	LESS J033149.2−280208	29	03 31 49.15	−28 02 08.7	6.9 ± 1.3	5.36
38	LESS J033310.2−275641	*	03 33 10.20	−27 56 41.5	6.4 ± 1.2	5.22
40	LESS J033246.7−275120	*	03 32 46.74	−27 51 20.9	6.4 ± 1.2	5.18
42	LESS J033231.0−275858	65	03 32 31.02	−27 58 58.1	6.4 ± 1.2	5.13
43	LESS J033307.0−274801	99,100	03 33 07.00	−27 48 01.0	6.4 ± 1.3	5.12
45	LESS J033225.7−275228	*	03 32 25.71	−27 52 28.5	6.3 ± 1.2	5.10
49	LESS J033124.5−275040	*	03 31 24.45	−27 50 40.9	6.6 ± 1.3	5.05
50	LESS J033141.2−274441	19,20	03 31 41.15	−27 44 41.5	6.1 ± 1.2	5.02
51	LESS J033144.8−274425	*	03 31 44.81	−27 44 25.1	6.2 ± 1.2	5.01
52	LESS J033128.5−275601	7	03 31 28.51	−27 56 01.3	6.2 ± 1.2	4.94
53	LESS J033159.1−275435	*	03 31 59.12	−27 54 35.5	6.2 ± 1.2	4.93
55	LESS J033302.2−274033	*	03 33 02.20	−27 40 33.6	6.1 ± 1.2	4.90
56	LESS J033153.2−273936	35	03 31 53.17	−27 39 36.1	6.0 ± 1.2	4.89
57	LESS J033152.0−275329	*	03 31 51.97	−27 53 29.7	6.1 ± 1.3	4.87
59	LESS J033303.9−274412	*	03 33 03.87	−27 44 12.2	6.0 ± 1.2	4.77
60	LESS J033317.5−275121	*	03 33 17.47	−27 51 21.5	5.8 ± 1.2	4.75
61	LESS J033245.6−280025	*	03 32 45.63	−28 00 25.3	5.9 ± 1.2	4.73
63	LESS J033308.5−280044	98	03 33 08.46	−28 00 44.3	6.0 ± 1.3	4.71
64	LESS J033201.0−280025	*	03 32 01.00	−28 00 25.6	5.8 ± 1.2	4.70
65	LESS J033252.4−273527	*	03 32 52.40	−27 35 27.7	5.9 ± 1.3	4.67
67	LESS J033243.3−275517	76,77	03 32 43.28	−27 55 17.9	5.9 ± 1.3	4.67
68	LESS J033233.4−273918	*	03 32 33.44	−27 39 18.5	5.8 ± 1.2	4.65
69	LESS J033134.3−275934	*	03 31 34.26	−27 59 34.3	5.7 ± 1.2	4.65
70	LESS J033144.0−273832	*	03 31 43.97	−27 38 32.5	5.7 ± 1.2	4.64
72	LESS J033240.4−273802	73	03 32 40.40	−27 38 02.5	5.7 ± 1.2	4.63

SID 870	Previously Published Name	Match ID	R.A. (h m s)	Dec. (° ′ ″)	Flux Density (mJy)	SNR
73	LESS J033229.3−275619	*	03 32 29.33	−27 56 19.3	5.8 ± 1.2	4.63
74	LESS J033309.3−274809	101,102,103	03 33 09.34	−27 48 09.9	5.8 ± 1.3	4.62
75	LESS J033126.8−275554	6	03 31 26.83	−27 55 54.6	5.8 ± 1.3	4.61
77	LESS J033157.2−275633	*	03 31 57.23	−27 56 33.2	5.5 ± 1.2	4.42
79	LESS J033221.3−275623	57	03 32 21.25	−27 56 23.5	5.5 ± 1.2	4.40
80	LESS J033142.2−274834	21,22	03 31 42.23	−27 48 34.4	5.4 ± 1.2	4.38
81	LESS J033127.5−274440	1	03 31 27.45	−27 44 40.4	5.7 ± 1.3	4.38
82	LESS J033253.8−273810	90	03 32 53.77	−27 38 10.9	5.3 ± 1.2	4.35
84	LESS J033154.2−275109	*	03 31 54.22	−27 51 09.8	5.5 ± 1.3	4.33
88	LESS J033155.2−275345	38,39	03 31 55.19	−27 53 45.3	5.4 ± 1.3	4.28
89	LESS J033248.4−280023	*	03 32 48.44	−28 00 23.8	5.3 ± 1.2	4.25
90	LESS J033243.7−273554	*	03 32 43.65	−27 35 54.1	5.4 ± 1.3	4.23
91	LESS J033135.3−274033	*	03 31 35.25	−27 40 33.7	5.3 ± 1.3	4.22
92	LESS J033138.4−274336	*	03 31 38.36	−27 43 36.0	5.2 ± 1.2	4.22
94	LESS J033307.3−275805	*	03 33 07.27	−27 58 05.0	5.3 ± 1.2	4.20
95	LESS J033241.7−275846	*	03 32 41.74	−27 58 46.1	5.2 ± 1.2	4.18
96	LESS J033313.0−275556	106	03 33 13.03	−27 55 56.8	5.2 ± 1.2	4.18
97	LESS J033313.7−273803	*	03 33 13.65	−27 38 03.4	5.1 ± 1.2	4.16
98	LESS J033130.2−275726	10,11	03 31 30.22	−27 57 26.0	5.1 ± 1.2	4.11
99	LESS J033251.5−275536	*	03 32 51.45	−27 55 36.0	5.3 ± 1.3	4.11
101	LESS J033151.5−274552	*	03 31 51.47	−27 45 52.1	5.1 ± 1.3	4.08
104	LESS J033258.5−273803	*	03 32 58.46	−27 38 03.0	4.9 ± 1.2	4.05
106	LESS J033140.1−275631	18	03 31 40.09	−27 56 31.4	4.9 ± 1.2	4.03
107	LESS J033130.9−275150	*	03 31 30.85	−27 51 50.9	5.0 ± 1.2	4.02
108	LESS J033316.4−275033	109	03 33 16.42	−27 50 33.1	5.0 ± 1.2	4.02
113	LESS J033236.4−275845	*	03 32 36.42	−27 58 45.9	5.0 ± 1.3	3.94
114	LESS J033150.8−274438	31,32	03 31 50.81	−27 44 38.5	4.9 ± 1.3	3.90
116	LESS J033154.4−274525	*	03 31 54.42	−27 45 25.5	4.9 ± 1.3	3.84
117	LESS J033128.0−273925	2,3,4	03 31 28.02	−27 39 25.2	5.0 ± 1.3	3.83
120	LESS J033328.5−275655	118	03 33 28.45	−27 56 55.9	4.9 ± 1.3	3.79
122	LESS J033139.6−274120	17	03 31 39.62	−27 41 20.4	4.7 ± 1.2	3.77

Table C5. Matches between the external catalogue with each of the 4 submm peak lists. The first column gives a unique short ID that is used throughout this paper. Since all radio sources and the FIDEL catalogue use the SIMPLE survey (*Spitzer* IRAC/MUSYC Public Legacy in ECDF-S; Gawiser et al. 2006) as a positional prior, the SIMPLE IDs for each source are given in column two. The only exceptions are 870 µm peaks with no identification in the matching catalogue; these peaks have simply been added to the catalogue with the SIMPLE ID replaced by the 870 µm SID referring to Table C4 (in boldface brackets). The third and fourth columns give the IRAC J2000 coordinates of each source (or the 870 µm position when unavailable). There are then 4 blocks of 5 columns for each submm band giving: the submm SID for each respective submm peak list to which the source was matched (Tables C1-C4); the radial separation in arcsec; the likelihood ratio; and finally the 24 µm and 1.4 GHz P values when available.

ID	SIMPLE	R.A.	Dec.	250 µm					350 µm					500 µm					870 µm				
		(h m s)	(° ′ ″)	SID 250	Δr (″)	LR	P_{24}	$P_{\rm R}$	SID 350	Δr (″)	LR	P_{24}	$P_{\rm R}$	SID 500	Δr (″)	LR	P_{24}	$P_{\rm R}$	SID 870	Δr (″)	LR	P_{24}	$P_{\rm R}$
1	37075	03 31 27.53	−27 44 39.3	78	11.2	14.4	0.098	0.058	235	8.2	11.2	0.061	0.035	...	...	...	...	...	81	1.5	43.1	0.003	0.002
2	45028	03 31 27.58	−27 39 27.6	...	...	...	...	...	22	7.4	1.7	0.215	0.066	...	...	...	...	...	117	6.3	2.2	0.168	0.048
3	45037	03 31 27.95	−27 39 36.4	...	...	...	...	...	22	4.4	3.7	0.076	0.038	17	6.6	1.6	0.141	0.075	117	11.3	1.2	...	...
4	45195	03 31 28.81	−27 39 17.0	...	...	...	...	...	...	...	...	...	...	...	...	...	...	...	117	13.3	1.0	...	...
5	45836	03 31 28.86	−27 39 04.1	80	2.9	1.3	0.013	0.051	...	...	...	...	...	...	...	...	...	...	...	...	...	...	...
6	18957	03 31 27.18	−27 55 51.0	...	...	...	...	...	...	...	...	...	...	9	27.4	2.5	...	...	...	...	...	...	...
7	18523	03 31 28.87	−27 56 07.8	...	...	...	...	...	...	...	...	...	...	...	...	...	...	...	52	8.1	1.7	0.206	0.492
8	17966	03 31 30.06	−27 56 02.2	111	0.8	16.9	0.001	0.001	...	...	...	...	...	...	...	...	...	...	...	...	...	...	...
9	**(5)**	03 31 29.46	−27 59 07.3	99	5.2	...	...	...	177	2.8	...	...	...	64	7.4	...	...	...	...	...	...	...	...
10	16359	03 31 29.89	−27 57 22.4	16	1.8	8.0	0.014	0.003	16	3.8	13.7	0.052	0.012	11	5.1	9.9	0.082	0.020	98	5.6	16.9	0.092	0.022
11	15753	03 31 30.74	−27 57 33.8	16	14.4	1.2	0.615	0.056	...	...	...	...	...	...	...	...	...	...	...	...	...	...	...
12	44643	03 31 36.10	−27 39 40.6	70	5.8	3.0	0.031	0.029	...	...	...	...	...	...	...	...	...	...	...	...	...	...	...
13	21125	03 31 35.50	−27 54 35.4	...	...	...	...	...	49	12.1	5.0	0.336	0.146	48	12.9	3.3	0.359	0.163	4	7.8	10.2	0.198	0.073
14	20735	03 31 35.91	−27 54 43.3	...	...	...	...	...	49	7.5	1.1	0.201	0.549	...	...	...	...	...	4	4.3	4.6	0.090	0.355
15	20560	03 31 36.15	−27 54 49.6	...	...	...	...	...	49	9.7	2.3	0.197	0.162	48	7.0	4.2	0.128	0.105	26	11.8	2.7	...	...
16	19870	03 31 36.94	−27 55 10.6	...	...	...	...	...	...	...	...	...	...	...	...	...	...	...	26	14.5	1.3	...	...
17	42263	03 31 39.53	−27 41 19.4	244	10.1	41.3	0.023	0.050	42	7.1	70.1	0.013	0.028	...	...	...	...	...	122	1.5	79.8	0.001	0.002
18	18083	03 31 40.17	−27 56 22.4	92	14.1	1.7	0.221	0.198	...	...	...	...	...	...	...	...	...	...	106	9.1	8.1	0.120	0.102
19	37304	03 31 40.97	−27 44 34.9	85	3.9	5.2	0.038	0.031	37	4.0	9.7	0.040	0.033	...	...	...	...	...	50	7.0	15.2	0.094	0.076
20	36814	03 31 41.37	−27 44 46.7	...	...	...	...	...	...	...	...	...	...	...	...	...	...	...	50	6.0	1.6	0.129	0.078
21	31008	03 31 41.63	−27 48 30.3	...	...	...	...	...	...	...	...	...	...	...	...	...	...	...	80	9.0	1.1	0.235	0.501
22	30829	03 31 42.80	−27 48 36.7	...	...	...	...	...	...	...	...	...	...	...	...	...	...	...	80	7.9	1.1	0.399	0.165
23	19031	03 31 41.77	−27 55 37.8	...	...	...	...	...	187	9.3	1.4	0.280	0.105	...	...	...	...	...	...	...	...	...	...
24	18659	03 31 43.58	−27 55 28.1	255	17.9	1.1	...	...	...	...	...	...	...	...	...	...	...	...	...	...	...	...	...
25	40970	03 31 44.46	−27 42 12.0	57	9.0	1.7	0.098	0.061	...	...	...	...	...	...	...	...	...	...	...	...	...	...	...
26	**(125)**	03 31 46.02	−27 46 21.2	32	17.6	...	...	...	...	...	...	...	...	...	...	...	...	...	125	0.0	...	...	...
27	16076	03 31 46.56	−27 57 34.8	36	10.9	21.2	0.033	0.035	...	...	...	...	...	...	...	...	...	...	...	...	...	...	...
28	31651	03 31 48.03	−27 48 01.7	...	...	...	...	...	188	10.5	6.2	0.113	0.117	...	...	...	...	...	...	...	...	...	...
29	10254	03 31 48.95	−28 02 13.6	...	...	...	...	...	322	10.2	2.7	0.211	0.183	177	13.0	3.7	0.283	0.252	36	5.6	11.1	0.090	0.074
30	38757	03 31 49.73	−27 43 26.1	59	8.6	10.5	0.030	0.042	35	2.2	4.4	0.003	0.004	...	...	...	...	...	...	...	...	...	...
31	37046	03 31 50.30	−27 44 46.8	...	...	...	...	...	...	...	...	...	...	...	...	...	...	...	114	10.7	1.5	...	...
32	36827	03 31 51.09	−27 44 37.0	146	1.3	8.1	0.003	0.003	47	4.0	9.7	0.019	0.023	...	...	...	...	...	114	3.9	30.6	0.019	0.021
33	8829	03 31 52.48	−28 03 18.6	...	...	...	...	...	95	19.2	1.0	...	...	...	...	...	...	...	14	2.8	17.4	0.112	0.012
34	45260	03 31 52.07	−27 39 26.6	51	9.3	5.9	0.109	0.013	124	8.1	16.4	0.087	0.010	14	4.8	14.1	0.038	0.004	...	...	...	...	...
35	45144	03 31 53.11	−27 39 37.3	51	8.3	1.1	0.166	0.169	124	9.8	2.3	0.208	0.211	14	21.0	1.9	0.451	0.458	56	1.4	11.5	0.010	0.010
36	28865	03 31 54.67	−27 49 44.4	...	...	...	...	...	93	7.0	1.5	0.193	0.144	205	2.5	1.9	0.040	0.029	...	...	...	...	...
37	37463	03 31 54.98	−27 44 10.5	188	11.2	1.2	0.431	0.052	...	...	...	...	...	...	...	...	...	...	...	...	...	...	...
38	22221	03 31 54.82	−27 53 41.0	...	...	...	...	...	...	...	...	...	...	...	...	...	...	...	88	6.6	5.7	0.109	0.042
39	22204	03 31 55.76	−27 53 47.5	...	...	...	...	...	...	...	...	...	...	...	...	...	...	...	88	7.9	2.5	0.207	0.224
40	13515	03 31 56.86	−27 59 39.0	...	...	...	...	...	...	...	...	...	...	157	12.7	3.4	0.317	0.196	25	3.1	17.3	0.044	0.022
41	41664	03 32 02.14	−27 41 28.5	...	...	...	...	...	170	9.6	2.6	0.220	0.132	...	...	...	...	...	...	...	...	...	...
42	11649	03 32 04.66	−28 00 57.6	328	12.1	2.0	0.375	0.071	...	...	...	...	...	...	...	...	...	...	...	...	...	...	...
43	33160	03 32 04.87	−27 46 47.3	75	3.9	4.7	0.016	0.015	19	5.8	3.2	0.032	0.028	...	...	...	...	...	18	5.8	11.8	0.032	0.028
44	15657	03 32 08.24	−27 58 13.9	...	...	...	...	...	...	...	...	...	...	8	9.0	1.2	0.447	0.181	19	5.1	3.9	0.251	0.075
45	9589	03 32 10.99	−28 02 36.0	246	6.8	1.2	0.162	0.134	...	...	...	...	...	...	...	...	...	...	...	...	...	...	...
46	24758	03 32 11.35	−27 52 13.0	...	...	...	...	...	...	...	...	...	...	...	...	...	...	...	9	2.7	3.5	0.091	0.041
47	40039	03 32 10.49	−27 43 08.8	358	13.5	2.0	0.146	0.313	...	...	...	...	...	...	...	...	...	...	...	...	...	...	...
48	39690	03 32 12.54	−27 43 06.0	...	...	...	...	...	...	...	...	...	...	91	11.4	3.6	0.280	0.248	...	...	...	...	...
49	47577	03 32 11.63	−27 37 25.9	...	...	...	...	...	88	4.3	64.1	0.005	0.001	58	18.2	20.1	0.055	0.012	...	...	...	...	...
50	18807	03 32 13.85	−27 55 59.9	...	...	...	...	...	...	...	...	...	...	33	10.4	1.8	0.455	0.183	11	4.4	7.4	0.181	0.048
51	44585	03 32 16.19	−27 39 30.3	...	...	...	...	...	108	12.6	35.7	0.032	0.190	...	...	...	...	...	...	...	...	...	...
52	14672	03 32 17.04	−27 58 46.5	...	...	...	...	...	...	...	...	...	...	203	7.0	1.8	0.398	0.004	...	...	...	...	...
53	13333	03 32 17.05	−27 59 16.6	38	9.7	30.3	0.019	0.054	80	10.2	24.3	0.021	0.059	...	...	...	...	...	...	...	...	...	...
54	25701	03 32 17.87	−27 50 59.0	289	6.7	5.1	0.017	0.060	...	...	...	...	...	...	...	...	...	...	...	...	...	...	...
55	24159	03 32 17.18	−27 52 20.5	58	11.2	1.3	0.259	0.113	65	14.8	1.5	0.351	0.168	...	...	...	...	...	...	...	...	...	...
56	24739	03 32 19.05	−27 52 14.5	...	...	...	...	...	65	12.6	2.6	0.450	0.139	21	10.3	1.6	0.384	0.106	10	5.0	10.9	0.161	0.032
57	17994	03 32 21.60	−27 56 23.3	45	3.5	2.9	0.014	0.048	...	...	...	...	...	31	10.2	1.0	0.085	0.232	79	4.7	4.1	0.023	0.072
58	11555	03 32 22.59	−28 00 23.4	97	6.3	8.4	0.006	0.011	...	...	...	...	...	...	...	...	...	...	...	...	...	...	...
59	48158	03 32 23.67	−27 36 48.2	91	12.4	64.5	0.006	0.056	...	...	...	...	...	...	...	...	...	...	...	...	...	...	...
60	46695	03 32 25.04	−27 38 22.4	325	1.0	1.6	0.003	0.001	169	5.3	1.1	0.044	0.024	...	...	...	...	...	...	...	...	...	...
61	35317	03 32 29.86	−27 44 24.2	5	8.4	87.8	0.002	0.010	8	10.1	4.2	0.003	0.014	53	12.6	1.3	0.005	0.021	...	...	...	...	...
62	37400	03 32 29.98	−27 44 04.8	5	12.2	60.8	0.010	0.038	8	14.2	19.9	0.013	0.048	...	...	...	...	...	...	...	...	...	...
63	39003	03 32 29.93	−27 43 01.0	...	...	...	...	...	12	6.4	1.2	0.142	0.091	104	9.5	1.4	0.240	0.164	...	...	...	...	...
64	13126	03 32 30.55	−27 59 11.3	121	7.5	124.9	0.004	0.017	85	11.5	69.4	0.008	0.036	...	...	...	...	...	...	...	...	...	...
65	14440	03 32 31.45	−27 58 51.5	...	...	...	...	...	85	22.1	1.0	...	...	...	...	...	...	...	42	8.7	8.6	0.176	0.103
66	17925	03 32 35.07	−27 55 32.6	3	1.9	28.1	0.000	0.001	3	2.9	17.8	0.001	0.002	...	...	...	...	...	...	...	...	...	...
67	29372	03 32 35.71	−27 49 15.9	113	13.8	3.4	0.131	0.186	...	...	...	...	...	250	11.5	2.7	0.100	0.147	...	...	...	...	...
68	10608	03 32 36.05	−28 01 37.9	...	...	...	...	...	259	10.9	1.4	0.320	0.132	...	...	...	...	...	...	...	...	...	...
69	10758	03 32 36.43	−28 01 51.0	...	...	...	...	...	259	7.4	2.0	0.294	0.092	...	...	...	...	...	...	...	...	...	...
70	50164	03 32 37.47	−27 35 47.8	69	5.9	4.3	0.038	0.067	69	5.7	3.6	0.036	0.064	...	...	...	...	...	...	...	...	...	...
71	50104	03 32 37.89	−27 35 49.9	69	6.5	4.7	0.046	0.050	69	8.2	3.4	0.068	0.074	...	...	...	...	...	...	...	...	...	...
72	16640	03 32 38.92	−27 57 00.3	316	12.5	27.7	0.016	0.082	...	...	...	...	...	133	15.5	6.9	0.023	0.114	...	...	...	...	...
73	46989	03 32 40.05	−27 38 08.6	...	...	...	...	...	...	...	...	...	...	...	...	...	...	...	72	7.6	1.2	0.057	0.199
74	46485	03 32 42.58	−27 38 25.9	60	12.3	20.6	0.030	0.072	...	...	...	...	...	...	...	...	...	...	...	...	...	...	...
75	46947	03 32 42.87	−27 38 17.1	60	13.2	1.1	0.516	0.021	...	...	...	...	...	...	...	...	...	...	...	...	...	...	...
76	19784	03 32 43.19	−27 55 14.4	...	...	...	...	...	128	4.5	9.5	0.024	0.030	...	...	...	...	...	67	3.7	31.1	0.017	0.022
77	19900	03 32 43.75	−27 55 16.2	...	...	...	...	...	...	...	...	...	...	...	...	...	...	...	67	6.4	2.5	0.277	0.154
78	44806	03 32 43.49	−27 39 29.1	82	8.7	1.9	0.087	0.190	...	...	...	...	...	...	...	...	...	...	...	...	...	...	...
79	25546	03 32 44.04	−27 51 43.3	298	7.6	21.0	0.048	0.025	...	...	...	...	...	...	...	...	...	...	...	...	...	...	...
80	25673	03 32 44.25	−27 51 41.1	298	10.9	67.0	0.003	0.040	...	...	...	...	...	...	...	...	...	...	...	...	...	...	...
81	15411	03 32 45.96	−27 57 45.3	24	1.3	30.2	0.000	0.001	116	10.1	3.7	0.017	0.050	...	...	...	...	...	...	...	...	...	...
82	21056	03 32 47.96	−27 54 16.3	...	...	...	...	...	...	...	...	...	...	...	...	...	...	...	12	2.6	1.9	0.137	0.035
83	40193	03 32 47.88	−27 42 32.9	...	...	...	...	...	...	...	...	...	...	37	7.6	1.7	0.023	0.028	...	...	...	...	...
84	40147	03 32 48.93	−27 42 51.3	...	...	...	...	...	...	...	...	...	...	...	...	...	...	...	13	6.1	3.9	0.478	0.210
85	40166	03 32 49.42	−27 42 35.3	...	...	...	...	...	...	...	...	...	...	...	...	...	...	...	13	11.6	1.7	...	...
86	14647	03 32 49.33	−27 58 45.0	17	3.5	12.8	0.033	0.008	7	11.4	6.8	0.195	0.055	144	14.6	7.6	0.263	0.082	...	...	...	...	...
87	48957	03 32 49.40	−27 36 36.1	369	17.0	1.1	...	...	...	...	...	...	...	...	...	...	...	...	...	...	...	...	...
88	12980	03 32 51.79	−27 59 56.2	389	15.2	1.2	0.145	0.166	...	...	...	...	...	...	...	...	...	...	...	...	...	...	...
89	11316	03 32 53.05	−28 01 17.8	...	...	...	...	...	90	6.5	2.9	0.102	0.106	...	...	...	...	...	...	...	...	...	...
90	**(82)**	03 32 53.77	−27 38 10.9	...	...	...	...	...	52	31.8	...	...	...	41	15.8	...	...	...	5	0.0	...	...	...

ID	SIMPLE	R.A.	Dec.	250 μm					350 μm					500 μm					870 μm				
		(h m s)	(° ′ ″)	SID	Δr (″)	LR	P_{24}	$P_{\rm r}$	SID	Δr (″)	LR	P_{24}	$P_{\rm r}$	SID	Δr (″)	LR	P_{24}	$P_{\rm r}$	SID	Δr (″)	LR	P_{24}	$P_{\rm r}$
91	**(6)**	03 32 57.14	−28 01 02.1	...	...	...	...	...	...	...	...	...	...	20	10.3	...	...	...	...	...	...	...	...
92	38977	03 32 57.63	−27 43 18.0	27	11.4	2.4	0.100	0.136	...	...	...	...	...	...	...	...	...	...	...	...	...	...	...
93	50259	03 32 59.32	−27 35 34.1	130	5.3	21.0	0.030	0.019	...	...	...	...	...	...	...	...	...	...	...	...	...	...	...
94	29432	03 32 59.32	−27 48 58.6	...	...	...	...	...	...	...	...	...	...	176	7.0	10.2	0.029	0.094	...	...	...	...	...
95	17004	03 33 01.59	−27 56 49.4	...	...	...	...	...	64	9.9	2.5	0.240	0.142	...	...	...	...	...	...	...	...	...	...
96	37597	03 33 06.16	−27 44 15.3	...	...	...	...	...	115	1.8	1.3	0.011	0.016	...	...	...	...	...	...	...	...	...	...
97	21942	03 33 07.78	−27 53 51.3	...	...	...	...	...	...	...	...	...	...	222	20.9	1.4	0.226	0.335	...	...	...	...	...
98	**(63)**	03 33 08.46	−28 00 44.3	...	...	...	...	...	...	...	...	...	...	200	25.2	...	...	...	...	...	...	...	...
99	31482	03 33 06.63	−27 48 02.0	...	...	...	...	...	...	...	...	...	...	...	...	...	...	...	43	5.0	2.6	0.099	0.396
100	30926	03 33 07.25	−27 48 08.4	...	...	...	...	...	...	...	...	...	...	...	...	...	...	...	43	8.1	1.1	0.074	0.189
101	31537	03 33 09.15	−27 48 16.8	...	...	...	...	...	145	8.7	1.4	0.278	0.169	...	...	...	...	...	74	7.4	4.9	0.222	0.126
102	30714	03 33 09.71	−27 48 01.6	52	14.7	27.5	0.031	0.052	145	22.0	2.6	...	...	...	...	...	...	...	74	9.7	11.3	0.015	0.025
103	30905	03 33 09.77	−27 48 21.0	...	...	...	...	...	...	...	...	...	...	...	...	...	...	...	74	12.5	2.2	...	...
104	26260	03 33 10.12	−27 51 24.8	...	...	...	...	...	...	...	...	...	...	44	11.3	1.3	0.263	0.237	...	...	...	...	...
105	41860	03 33 11.79	−27 41 38.4	...	...	...	...	...	31	10.2	6.5	0.256	0.035	...	...	...	...	...	...	...	...	...	...
106	18562	03 33 12.62	−27 55 51.7	...	...	...	...	...	298	15.9	2.1	...	...	...	...	...	...	...	96	7.5	1.2	0.024	0.073
107	**(1)**	03 33 14.26	−27 56 11.2	...	...	...	...	...	298	13.8	...	...	...	7	32.9	...	...	...	1	0.0	...	...	...
108	35704	03 33 15.42	−27 45 24.0	...	...	...	...	...	98	8.8	2.4	0.113	0.113	57	10.3	1.6	0.142	0.144	7	1.8	4.4	0.009	0.009
109	26283	03 33 16.51	−27 50 39.4	72	4.2	39.5	0.002	0.007	...	...	...	...	...	...	...	...	...	...	108	6.4	4.2	0.004	0.015
110	41704	03 33 16.93	−27 41 21.4	185	10.7	27.3	0.017	0.039	...	...	...	...	...	...	...	...	...	...	...	...	...	...	...
111	34567	03 33 17.78	−27 46 05.9	54	2.6	7.9	0.012	0.011	43	11.1	5.9	0.122	0.115	...	...	...	...	...	...	...	...	...	...
112	34104	03 33 17.78	−27 46 23.6	...	...	...	...	...	43	12.9	1.8	0.294	0.150	...	...	...	...	...	...	...	...	...	...
113	28590	03 33 17.43	−27 49 48.7	...	...	...	...	...	...	...	...	...	...	24	22.3	2.7	0.300	0.177	...	...	...	...	...
114	29761	03 33 17.81	−27 49 10.4	...	...	...	...	...	...	...	...	...	...	24	16.3	1.1	0.538	0.375	...	...	...	...	...
115	28465	03 33 18.69	−27 49 40.1	...	...	...	...	...	...	...	...	...	...	24	19.2	2.0	0.549	0.128	...	...	...	...	...
116	20681	03 33 18.90	−27 54 33.5	67	9.9	1.9	0.129	0.141	...	...	...	...	...	...	...	...	...	...	...	...	...	...	...
117	19773	03 33 21.48	−27 55 20.3	...	...	...	...	...	...	...	...	...	...	...	...	...	...	...	3	0.4	2.4	0.010	0.015
118	17028	03 33 28.56	−27 56 54.1	...	...	...	...	...	14	15.2	1.0	0.273	0.313	5	5.9	5.0	0.075	0.093	120	2.3	11.2	0.015	0.019

Table C6. Maximum-likelihood submm photometry, SED model fits and redshifts. Uncertainties in flux densities have the estimated confusion noise (Tables 1) added in quadrature to the instrumental noise. The temperatures, $T_{\rm obs}$ and 10-1000 μm total infrared (TIR) fluxes, $S_{\rm TIR}$ are for *observed-frame* modified blackbody fits of the form $S_\nu \propto \nu^{2.0} B_\nu(T_{\rm obs})$ (rest-frame values shown in Fig. E1). The fractional uncertainties in the TIR fluxes, $\Delta S_{\rm TIR}/S_{\rm TIR}$, are produced from the same Monte Carlo simulation used to measure uncertainties in the temperatures. SED fits are not provided for confused sources (see SEDs with 'C' indicated in Fig. E1). When redshifts are available, the TIR luminosity, $L_{\rm TIR}$, is also calculated, but integrating in the *rest-frame*, and using a more realistic SED fit from the library of Dale et al. (2001) in order to estimate emission in the mid/far-IR (fits shown in Fig. E1). Redshifts in boldface are optical spectroscopic measurements, redshifts in regular face are optical photometric estimates, and redshifts in brackets are IRAC-based photometric estimates. The superscripts indicate where the redshifts were found: 'P' from the composite catalogue of Pascale et al. (2009); 'I' from Ivison et al. (2010); 'D' from Dunlop et al. (2010); and 'C' from Casey et al. (2010).

ID	S_{250} (mJy)	S_{350} (mJy)	S_{500} (mJy)	S_{870} (mJy)	$T_{\rm obs}$ (K)	$S_{\rm TIR}$ ($\log_{10}$ W m^{-2})	$\Delta S_{\rm TIR}/S_{\rm TIR}$	$L_{\rm TIR}$ ($\log_{10}$ L$_\odot$)	Redshift (z)
1	38±18	41±15	9±13	5.1±1.2	10.5±1.1	-15.3	0.36	12.4	(1.9)$^{\rm P}$
2	17±33	-40±30	-92±31	1.2±2.2	...	...	...	...	1.1$^{\rm P}$
3	40±31	95±29	131±30	2.3±2.1	...	...	...	...	0.8$^{\rm P}$
4	26±32	-2±30	0±31	2.1±1.5	...	...	...	...	1.7$^{\rm P}$
5	62±30	56±29	29±30	2.2±1.4	...	...	...	...	2.6$^{\rm P}$
6	13±21	30±19	42±18	3.6±1.2	9.7±1.0	-15.5	0.35	12.6	2.7$^{\rm P}$
7	-20±34	-7±33	-28±39	4.1±1.3	...	...	...	...	(1.9)$^{\rm P}$
8	93±30	29±29	49±31	-0.2±1.3	...	...	...	...	**0.677**$^{\rm I}$
9	69±18	47±15	51±13	9.6±1.2	9.9±0.7	-15.1	0.24	...	...
10	109±24	85±20	60±18	3.3±1.2	...	...	...	...	**1.482**$^{\rm C}$
11	-14±24	-25±20	-14±18	2.8±1.2	...	...	...	...	0.4$^{\rm P}$
12	68±18	40±15	22±13	-0.4±1.2	17.7±0.5	-14.8	0.15	12.4	1.2$^{\rm P}$
13	-39±47	-19±52	29±50	4.1±1.8	...	...	...	...	...
14	31±85	57±101	-5±101	2.9±2.5	...	...	...	...	(1.2)$^{\rm P}$
15	16±58	20±68	18±67	6.3±1.8	...	...	...	...	0.1$^{\rm P}$
16	24±22	-8±20	14±19	4.4±1.2	6.1±1.9	-16.2	0.72	11.6	2.1$^{\rm P}$
17	41±18	43±15	24±13	4.2±1.2	11.4±1.8	-15.2	0.48	12.6	**2.024**$^{\rm P}$
18	55±18	20±15	13±13	3.6±1.2	13.0±4.5	-15.1	0.90	13.1	3.0$^{\rm P}$
19	32±29	51±26	51±23	2.5±1.3	...	...	...	...	(0.6)$^{\rm P}$
20	28±29	-2±26	-23±23	3.9±1.3	...	...	...	...	0.4$^{\rm P}$
21	21±27	13±23	24±22	2.9±1.3	...	...	...	...	1.2$^{\rm P}$
22	-9±27	4±23	3±22	3.2±1.3	...	...	...	...	(2.2)$^{\rm P}$
23	21±19	37±16	28±15	2.5±1.2	11.4±2.1	-15.4	0.67	12.1	(1.5)$^{\rm P}$
24	28±19	25±16	0±15	1.7±1.2	21.6±1.3	-14.7	0.19	9.9	**0.095**$^{\rm P}$
25	65±18	33±15	30±13	1.4±1.2	15.7±1.0	-14.9	0.24	12.2	1.1$^{\rm I}$
26	77±18	22±15	22±13	3.9±1.2	14.4±3.7	-14.9	0.90	...	...
27	78±18	45±15	22±13	0.4±1.2	23.2±0.9	-14.3	0.09	11.6	**0.364**$^{\rm P}$
28	40±18	38±15	13±13	3.6±1.2	11.9±1.8	-15.2	0.63	11.3	0.6$^{\rm P}$
29	35±18	39±15	30±13	6.5±1.2	9.6±1.1	-15.3	0.41	12.5	(2.1)$^{\rm P}$
30	84±18	53±15	33±13	3.2±1.2	18.2±0.4	-14.5	0.08	12.0	**0.620**$^{\rm P}$
31	18±22	-11±20	25±19	1.7±1.2	9.2±2.9	-16.0	0.90	12.2	(3.0)$^{\rm P}$
32	57±23	79±20	15±19	3.4±1.2	13.5±1.8	-14.9	0.42	12.6	**1.605**$^{\rm C}$
33	29±18	33±15	22±13	8.1±1.3	8.4±1.0	-15.4	0.33	11.7	(1.2)$^{\rm P}$
34	42±19	29±17	25±15	1.1±1.2	14.5±1.4	-15.1	0.45	12.8	**2.342**$^{\rm C}$
35	74±20	50±17	38±15	5.2±1.2	12.3±1.2	-14.9	0.37	13.2	2.9$^{\rm P}$
36	60±18	60±15	47±13	3.2±1.2	...	...	...	...	(2.1)$^{\rm P}$
37	54±18	43±15	24±13	2.6±1.2	...	...	...	...	0.6$^{\rm P}$
38	30±27	35±24	49±22	1.7±1.3	...	...	...	...	...
39	14±27	5±24	-15±22	3.4±1.3	...	...	...	...	1.8$^{\rm P}$
40	11±18	31±15	26±13	6.1±1.2	8.3±0.9	-15.6	0.33	11.9	(1.6)$^{\rm P}$
41	17±18	31±15	0±13	1.3±1.2	18.5±1.4	-15.0	0.30	9.9	0.1$^{\rm P}$
42	30±18	12±15	11±13	2.0±1.2	12.8±6.0	-15.4	0.90	10.1	0.2$^{\rm P}$
43	68±18	58±15	20±13	6.3±1.2	11.7±1.0	-15.0	0.32	12.9	**2.252**$^{\rm C}$
44	55±18	60±15	65±13	6.0±1.2	10.8±0.7	-15.1	0.29	9.7	(0.1)$^{\rm P}$
45	37±18	5±15	5±13	-0.1±1.2	32.6±7.8	-14.1	0.59	12.5	0.7$^{\rm P}$
46	22±18	55±15	43±13	8.5±1.2	8.8±0.6	-15.3	0.32	12.2	(1.6)$^{\rm P}$
47	42±18	-15±16	-10±14	1.7±1.2	17.5±1.3	-15.2	0.24	11.2	0.6$^{\rm P}$
48	15±18	38±16	43±14	2.0±1.2	11.1±3.0	-15.4	0.90	12.1	1.7$^{\rm D}$
49	30±18	52±15	32±13	2.1±1.2	12.5±1.4	-15.2	0.53	12.3	**1.565**$^{\rm P}$
50	16±18	10±15	35±13	8.1±1.2	7.1±1.3	-15.7	0.52	10.7	(0.6)$^{\rm P}$

ID	S_{250} (mJy)	S_{350} (mJy)	S_{500} (mJy)	S_{870} (mJy)	$T_{\rm obs}$ (K)	$S_{\rm TIR}$ ($\log_{10}$ W m^{-2})	$\Delta S_{\rm TIR}/S_{\rm TIR}$	$L_{\rm TIR}$ ($\log_{10}$ L$_\odot$)	Redshift (z)
51	48±18	55±15	12±13	-0.6±1.2	17.0±0.5	-14.9	0.21	12.4	**1.324**$^{\rm P}$
52	33±19	33±16	21±14	0.2±1.2	18.2±5.1	-14.9	0.90	11.6	0.6$^{\rm P}$
53	74±19	51±16	17±14	2.1±1.2	21.0±0.7	-14.4	0.11	10.5	0.1$^{\rm P}$
54	56±18	26±15	17±13	1.5±1.2	20.5±0.9	-14.6	0.15	10.3	**0.124**$^{\rm D}$
55	46±19	24±16	30±14	3.0±1.2	12.5±2.1	-15.2	0.56	11.9	**1.097**$^{\rm D}$
56	35±19	50±17	25±15	8.2±1.2	9.2±1.1	-15.3	0.40	12.6	2.3$^{\rm D}$
57	69±18	32±15	37±13	4.4±1.2	12.6±2.9	-15.0	0.89	12.9	**2.277**$^{\rm C}$
58	51±18	18±15	-5±13	-0.3±1.2	25.2±1.4	-14.4	0.14	10.1	0.1$^{\rm P}$
59	48±18	26±15	19±13	1.0±1.2	24.4±1.2	-14.4	0.13	10.3	0.1$^{\rm P}$
60	69±18	42±15	34±13	1.8±1.2	15.7±2.1	-14.8	0.38	12.3	1.1$^{\rm P}$
61	97±20	42±18	33±16	1.9±1.2	24.8±0.8	-14.1	0.08	10.4	**0.077**$^{\rm I}$
62	65±21	36±18	1±16	0.1±1.2	24.8±1.1	-14.3	0.12	10.1	**0.076**$^{\rm P}$
63	64±18	73±15	43±13	4.0±1.2	12.7±2.0	-14.9	0.56	12.4	1.4$^{\rm P}$
64	51±19	26±16	6±14	2.5±1.2	...	...	...	...	**0.125**$^{\rm P}$
65	27±18	4±16	-10±14	4.2±1.2	...	...	...	...	(2.3)$^{\rm P}$
66	185±18	78±15	35±13	0.1±1.2	22.1±0.4	-14.1	0.05	9.7	**0.038**$^{\rm D}$
67	54±18	35±15	40±13	2.7±1.2	13.2±1.4	-15.1	0.25	13.1	2.8$^{\rm P}$
68	20±20	27±18	13±16	-1.3±1.2	...	...	...	...	0.6$^{\rm P}$
69	26±20	10±18	-3±16	1.6±1.2	...	...	...	...	(2.2)$^{\rm P}$
70	102±29	67±26	95±23	-1.4±1.8	...	...	...	...	(1.8)$^{\rm P}$
71	-31±29	-11±26	-53±23	2.7±1.8	...	...	...	...	0.2$^{\rm P}$
72	47±18	29±15	28±13	-1.6±1.2	22.3±0.8	-14.6	0.10	11.1	**0.297**$^{\rm P}$
73	30±18	35±15	21±13	4.4±1.2	10.3±2.0	-15.3	0.66	11.4	**0.830**$^{\rm P}$
74	6±29	58±26	49±25	3.1±1.8	...	...	...	...	**0.250**$^{\rm P}$
75	43±29	-42±26	-42±25	-1.1±1.8	...	...	...	...	0.1$^{\rm P}$
76	79±27	41±24	24±22	1.8±1.5	...	...	...	...	**2.123**$^{\rm C}$
77	-24±27	13±24	1±22	3.8±1.5	...	...	...	...	2.8$^{\rm P}$
78	65±18	34±15	21±13	1.3±1.2	19.2±6.7	-14.6	0.90	12.1	**0.733**$^{\rm P}$
79	55±27	33±23	8±22	0.4±1.9	...	...	...	...	**0.279**$^{\rm P}$
80	-10±27	0±23	-1±22	0.4±1.9	...	...	...	...	**0.279**$^{\rm P}$
81	94±18	52±15	21±13	2.3±1.2	21.2±0.7	-14.3	0.11	10.4	**0.104**$^{\rm P}$
82	45±18	24±15	27±13	7.7±1.2	9.0±2.1	-15.4	0.69	12.8	2.8$^{\rm D\dagger}$
83	67±21	70±18	32±16	2.4±1.2	...	...	...	...	**0.981**$^{\rm P}$
84	-28±21	-38±18	-22±16	7.3±1.2	...	...	...	...	(1.9)$^{\rm P}$
85	10±20	7±18	34±16	2.8±1.2	...	...	...	...	**0.981**$^{\rm P}$
86	98±18	68±15	21±13	2.3±1.2	16.4±0.8	-14.6	0.22	13.3	**2.326**$^{\rm C}$
87	10±18	-22±15	3±13	0.7±1.2	29.7±11.3	-15.6	0.34	10.3	0.4$^{\rm P}$
88	33±18	16±15	16±13	1.6±1.2	18.6±1.3	-14.9	0.24	11.6	**0.620**$^{\rm P}$
89	-5±18	43±15	8±13	1.8±1.2	10.0±1.8	-15.7	0.41	11.8	(1.6)$^{\rm P}$
90	52±18	51±15	42±13	4.6±1.2	11.6±1.8	-15.1	0.35	...	...
91	18±18	40±15	39±13	8.9±1.2	8.2±0.8	-15.4	0.30	...	...
92	90±18	54±15	38±13	2.8±1.2	15.7±1.7	-14.7	0.33	13.0	1.9$^{\rm P}$
93	58±18	25±15	7±13	0.9±1.2	18.4±0.8	-14.8	0.17	10.6	0.2$^{\rm P}$
94	43±18	13±15	29±13	1.3±1.2	16.0±6.0	-15.0	0.90	11.2	0.5$^{\rm P}$
95	25±18	39±15	32±13	4.7±1.2	9.9±1.4	-15.4	0.46	11.9	1.3$^{\rm P}$
96	51±18	52±15	15±13	0.2±1.2	19.7±4.8	-14.6	0.90	11.4	0.4$^{\rm P}$
97	36±18	9±15	29±13	1.9±1.2	12.9±2.2	-15.3	0.50	12.1	1.5$^{\rm P}$
98	-35±18	-7±15	13±13	5.2±1.2	4.4±1.3	-16.5	0.66	...	...
99	-30±29	48±28	4±33	3.0±1.3	...	...	...	...	(3.0)$^{\rm P}$
100	70±31	-27±30	35±41	3.0±1.3	...	...	...	...	**0.531**$^{\rm P}$

†Source 82 has an optical photometric redshift limit $z > 2.8$ from Dunlop et al. (2010). Since this limit is significantly larger than its IRAC-based photometric redshift $z_{\rm i} = 1.6$ we use the limit as the best estimate for this source.

ID	S_{250} (mJy)	S_{350} (mJy)	S_{500} (mJy)	S_{870} (mJy)	$T_{\rm obs}$ (K)	$S_{\rm TIR}$ ($\log_{10}$ W m^{-2})	$\Delta S_{\rm TIR}/S_{\rm TIR}$	$L_{\rm TIR}$ ($\log_{10}$ L$_\odot$)	Redshift (z)
101	24±43	100±42	-16±49	3.6±1.9	...	...	...	...	(2.2)$^{\rm P}$
102	38±32	-14±30	-11±28	2.0±1.2	...	...	...	...	**0.180**$^{\rm I}$
103	0±27	-51±25	45±27	-0.5±2.0	...	...	...	...	(1.4)$^{\rm P}$
104	53±18	36±15	35±13	0.9±1.2	16.9±4.7	-14.8	0.90	12.6	(1.6)$^{\rm P}$
105	21±18	44±15	9±13	0.9±1.2	18.3±1.4	-14.9	0.22	10.8	0.3$^{\rm P}$
106	34±19	28±16	41±14	3.9±1.2	16.4±1.0	-14.8	0.17	11.0	0.3$^{\rm P}$
107	27±19	34±16	9±14	14.1±1.2	6.4±1.8	-15.6	0.55	...	...
108	19±18	46±15	31±13	8.8±1.2	8.4±0.9	-15.4	0.33	11.5	0.9$^{\rm P}$
109	76±18	25±15	0±13	4.0±1.2	22.8±0.8	-14.3	0.09	10.3	**0.087**$^{\rm P}$
110	48±18	49±15	23±13	1.9±1.2	22.5±0.9	-14.4	0.11	10.6	**0.148**$^{\rm P}$
111	63±21	44±18	13±16	3.9±1.2	13.3±1.6	-15.0	0.36	12.8	2.1$^{\rm C}$
112	26±21	29±18	31±16	-0.1±1.2	18.2±3.2	-15.0	0.72	12.4	1.4$^{\rm P}$
113	-6±23	18±20	-7±19	3.3±1.2	...	...	...	...	(1.9)$^{\rm P}$
114	26±19	9±16	20±14	-0.7±1.2	...	...	...	...	(2.0)$^{\rm P}$
115	22±24	-8±21	22±21	1.8±1.2	...	...	...	...	0.9$^{\rm P}$
116	80±18	25±15	11±13	0.6±1.2	16.3±0.6	-14.8	0.14	11.4	0.5$^{\rm I}$
117	48±18	48±15	33±13	11.4±1.2	8.7±1.0	-15.2	0.38	12.2	(1.5)$^{\rm P}$
118	53±18	73±15	52±13	4.4±1.2	11.8±2.8	-15.1	0.90	...	...

APPENDIX E: SPECTRAL ENERGY DISTRIBUTIONS

This Appendix contains observed-frame radio–submm–(mid/near)-IR SEDs for all 118 proposed identifications to the submm peaks (Fig. E1).

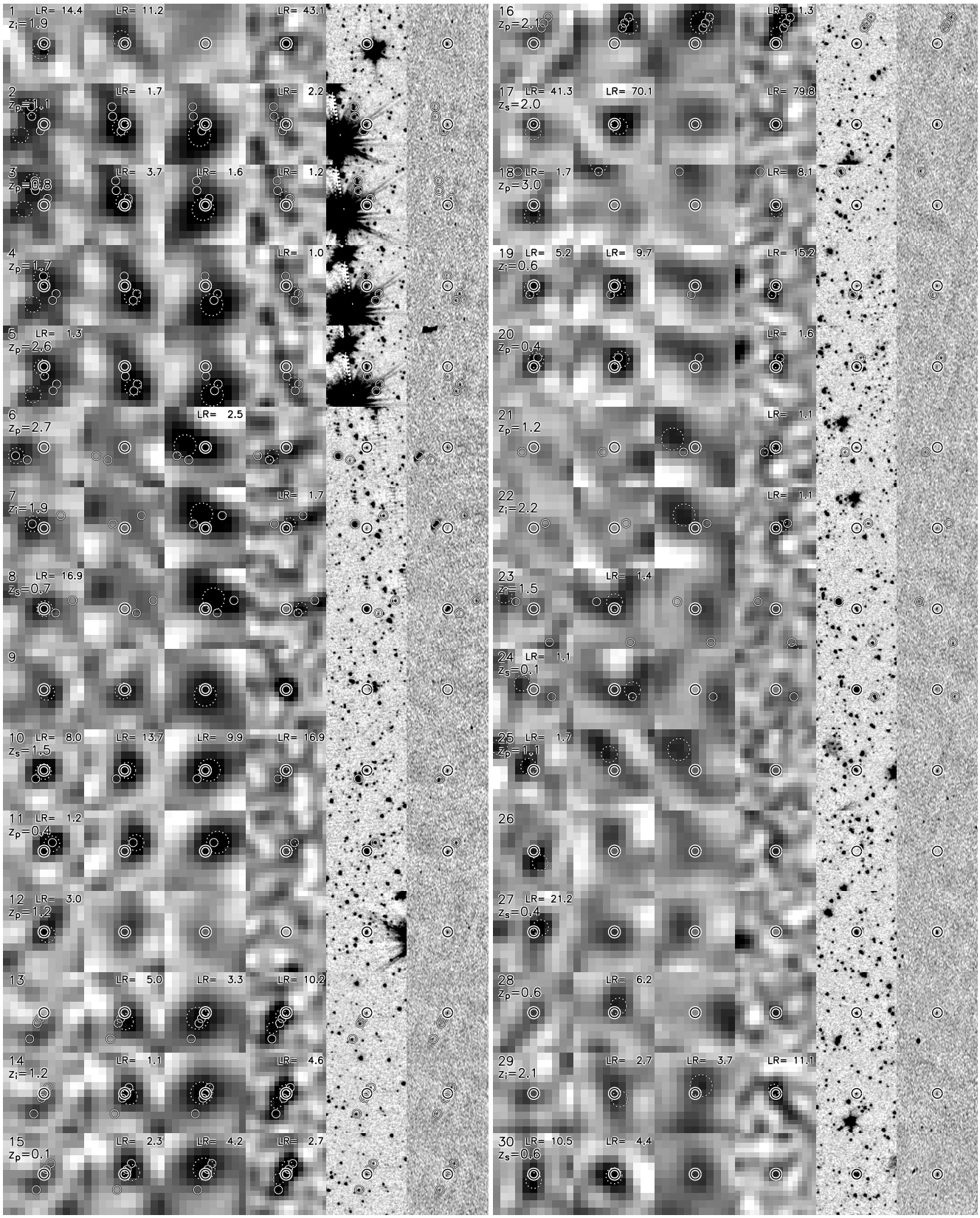

Figure D1. $1.8' \times 1.8'$ Postage stamps for each of the fitted sources. Columns from left to right: 250 µm, 350 µm, 500 µm, 870 µm(SNR maps, scaled between -3σ (white) and +5σ (black), 3.6 µm, and 1.4 GHz (-2 μJy (white), +5 μJy (black)). Small heavy circles indicate the source under consideration. Light smaller circles indicate other nearby sources that have been simultaneously fit in the submm bands. Large dashed circles on the submm images indicate input positions obtained from local maxima in the match-filtered images. Sources were matched to the external catalogue, and the reported redshifts are those that were used in Pascale et al. (2009) when available (subscript 's' indicates spectroscopic redshifts, 'p' optical photometric redshifts, and 'i' IRAC-based photometric redshifts). The likelihood ratios (LR) of the matches to each submm band are indicated in the top-right corners when available.

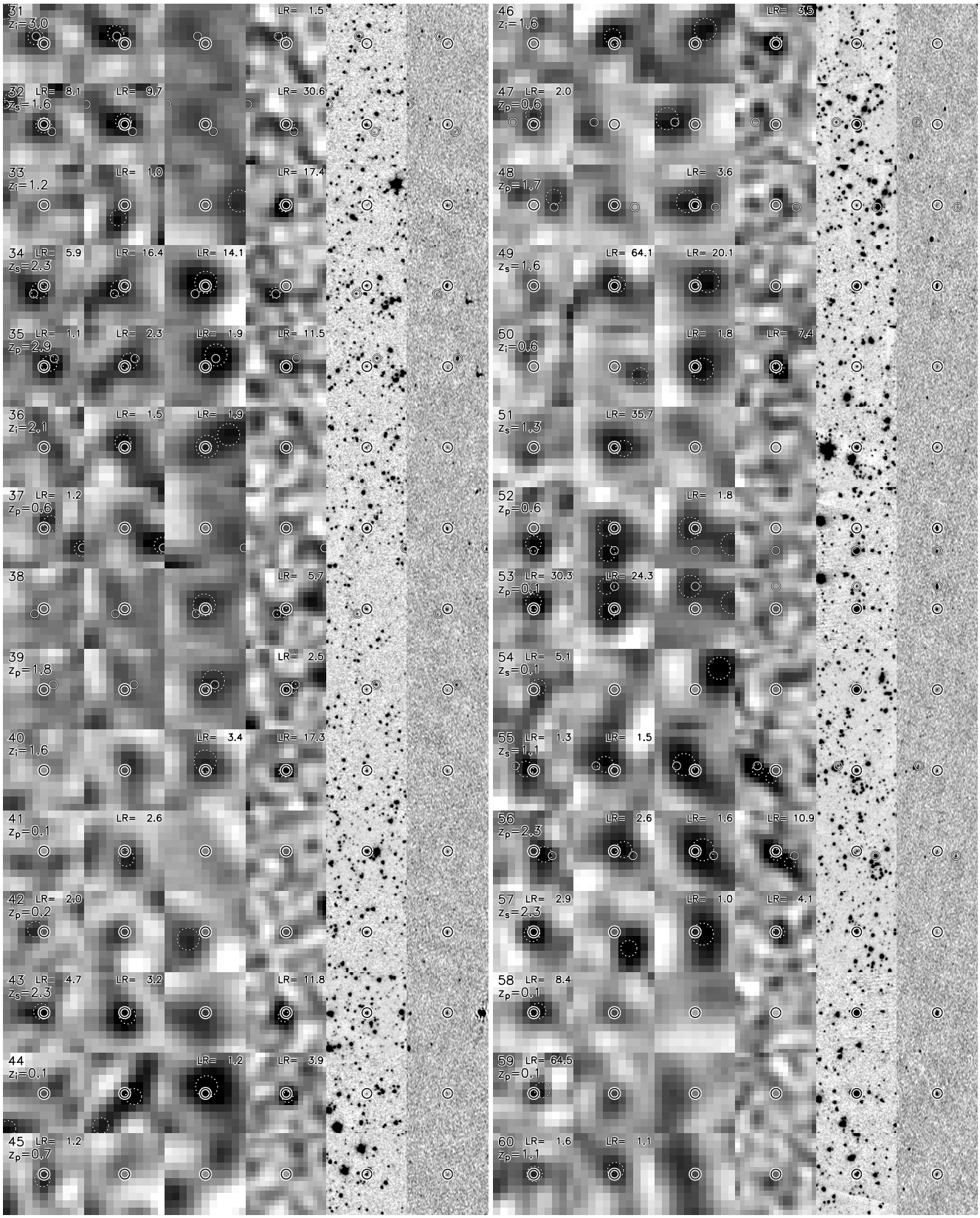
31 LR= 1.5
z_i=3.0
32 LR= 8.1 LR= 9.7 LR= 30.6
z_s=1.6
33 LR= 1.0 LR= 17.4
z_i=1.2
34 LR= 5.9 LR= 16.4 LR= 14.1
z_s=2.3
35 LR= 1.1 LR= 2.3 LR= 1.9 LR= 11.5
z_p=2.9
36 LR= 1.5 LR= 1.9
z_i=2.1
37 LR= 1.2
z_p=0.6
38 LR= 5.7
39 LR= 2.5
z_p=1.8
40 LR= 3.4 LR= 17.3
z_i=1.6
41 LR= 2.6
z_p=0.1
42 LR= 2.0
z_p=0.2
43 LR= 4.7 LR= 3.2 LR= 11.8
z_s=2.3
44 LR= 1.2 LR= 3.9
z_i=0.1
45 LR= 1.2
z_p=0.7
46 LR= 3.5
z_i=1.6
47 LR= 2.0
z_p=0.6
48 LR= 3.6
z_p=1.7
49 LR= 64.1 LR= 20.1
z_s=1.6
50 LR= 1.8 LR= 7.4
z_i=0.6
51 LR= 35.7
z_s=1.3
52 LR= 1.8
z_p=0.6
53 LR= 30.3 LR= 24.3
z_p=0.1
54 LR= 5.1
z_s=0.1
55 LR= 1.3 LR= 1.5
z_s=1.1
56 LR= 2.6 LR= 1.6 LR= 10.9
z_p=2.3
57 LR= 2.9 LR= 1.0 LR= 4.1
z_s=2.3
58 LR= 8.4
z_p=0.1
59 LR= 64.5
z_p=0.1
60 LR= 1.6 LR= 1.1
z_p=1.1

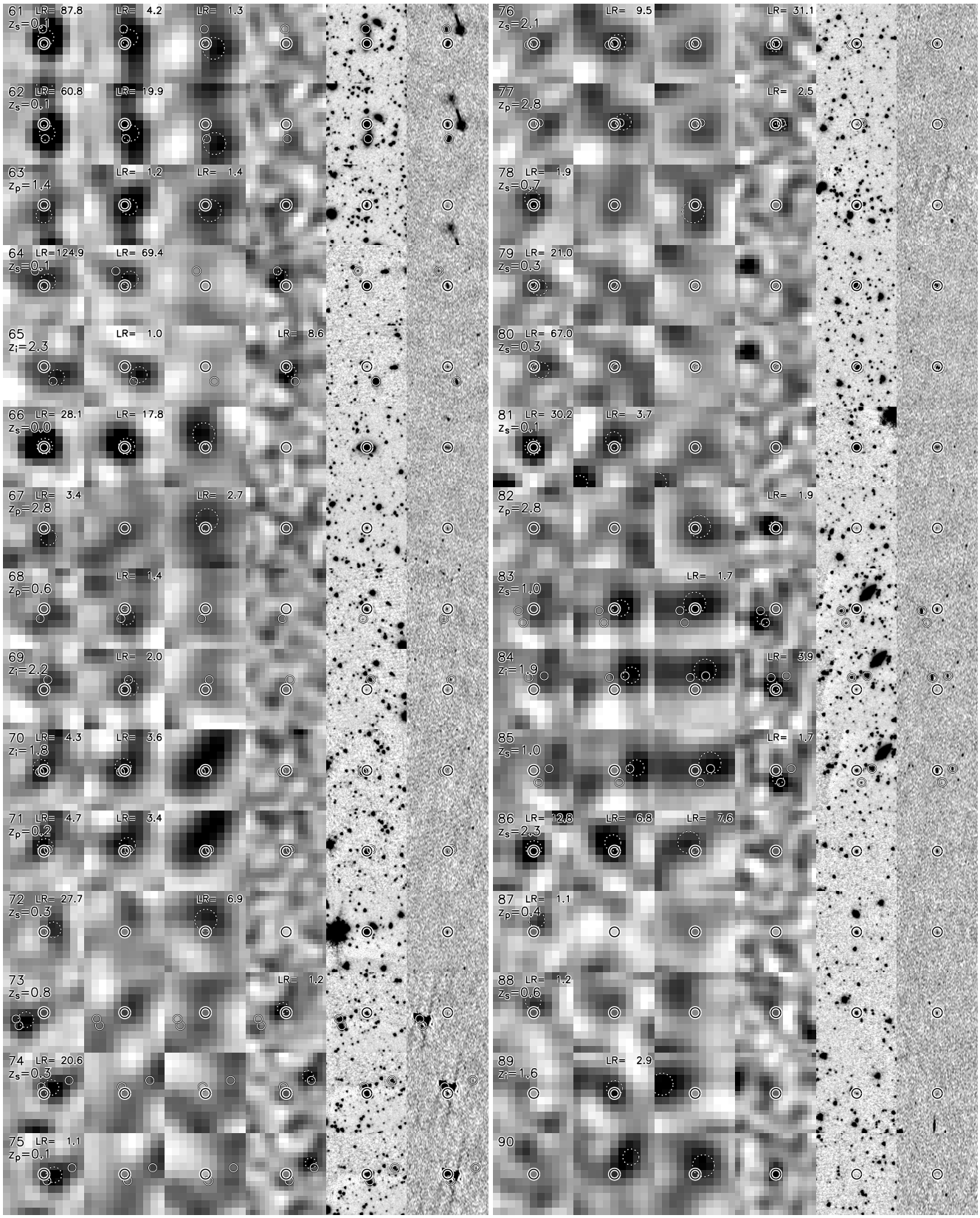
61 LR= 87.8 LR= 4.2 LR= 1.3
z_s=0.1
62 LR= 60.8 LR= 19.9
z_s=0.1
63 LR= 1.2 LR= 1.4
z_p=1.4
64 LR=124.9 LR= 69.4
z_s=0.1
65 LR= 1.0 LR= 8.6
z_i=2.3
66 LR= 28.1 LR= 17.8
z_s=0.0
67 LR= 3.4 LR= 2.7
z_p=2.8
68 LR= 1.4
z_p=0.6
69 LR= 2.0
z_i=2.2
70 LR= 4.3 LR= 3.6
z_i=1.8
71 LR= 4.7 LR= 3.4
z_p=0.2
72 LR= 27.7 LR= 6.9
z_s=0.3
73 LR= 1.2
z_s=0.8
74 LR= 20.6
z_s=0.3
75 LR= 1.1
z_p=0.1
76 LR= 9.5 LR= 31.1
z_s=2.1
77 LR= 2.5
z_p=2.8
78 LR= 1.9
z_s=0.7
79 LR= 21.0
z_s=0.3
80 LR= 67.0
z_s=0.3
81 LR= 30.2 LR= 3.7
z_s=0.1
82 LR= 1.9
z_p=2.8
83 LR= 1.7
z_s=1.0
84 LR= 3.9
z_i=1.9
85 LR= 1.7
z_s=1.0
86 LR= 12.8 LR= 6.8 LR= 7.6
z_s=2.3
87 LR= 1.1
z_p=0.4
88 LR= 1.2
z_s=0.6
89 LR= 2.9
z_i=1.6
90

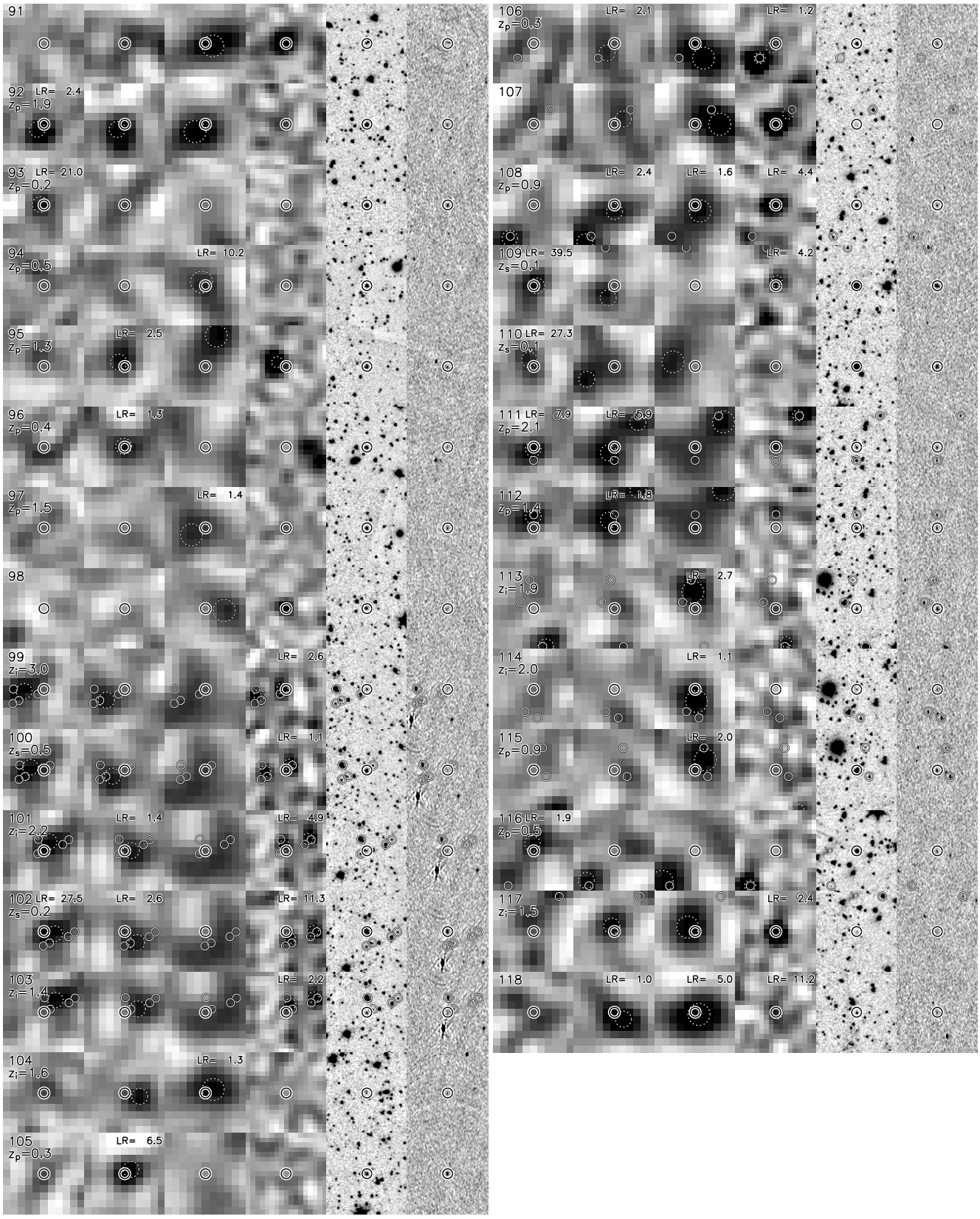
91
92 LR= 2.4
z_p=1.9
93 LR= 21.0
z_p=0.2
94 LR= 10.2
z_p=0.5
95 LR= 2.5
z_p=1.3
96 LR= 1.3
z_p=0.4
97 LR= 1.4
z_p=1.5
98
99 LR= 2.6
z_i=3.0
100 LR= 1.1
z_s=0.5
101 LR= 1.4 LR= 4.9
z_i=2.2
102 LR= 27.5 LR= 2.6 LR= 11.3
z_s=0.2
103 LR= 2.2
z_i=1.4
104 LR= 1.3
z_i=1.6
105 LR= 6.5
z_p=0.3
106 LR= 2.1 LR= 1.2
z_p=0.3
107
108 LR= 2.4 LR= 1.6 LR= 4.4
z_p=0.9
109 LR= 39.5 LR= 4.2
z_s=0.1
110 LR= 27.3
z_s=0.1
111 LR= 7.9 LR= 5.9
z_p=2.1
112 LR= 1.8
z_p=1.4
113 LR= 2.7
z_i=1.9
114 LR= 1.1
z_i=2.0
115 LR= 2.0
z_p=0.9
116 LR= 1.9
z_p=0.5
117 LR= 2.4
z_i=1.5
118 LR= 1.0 LR= 5.0 LR= 11.2

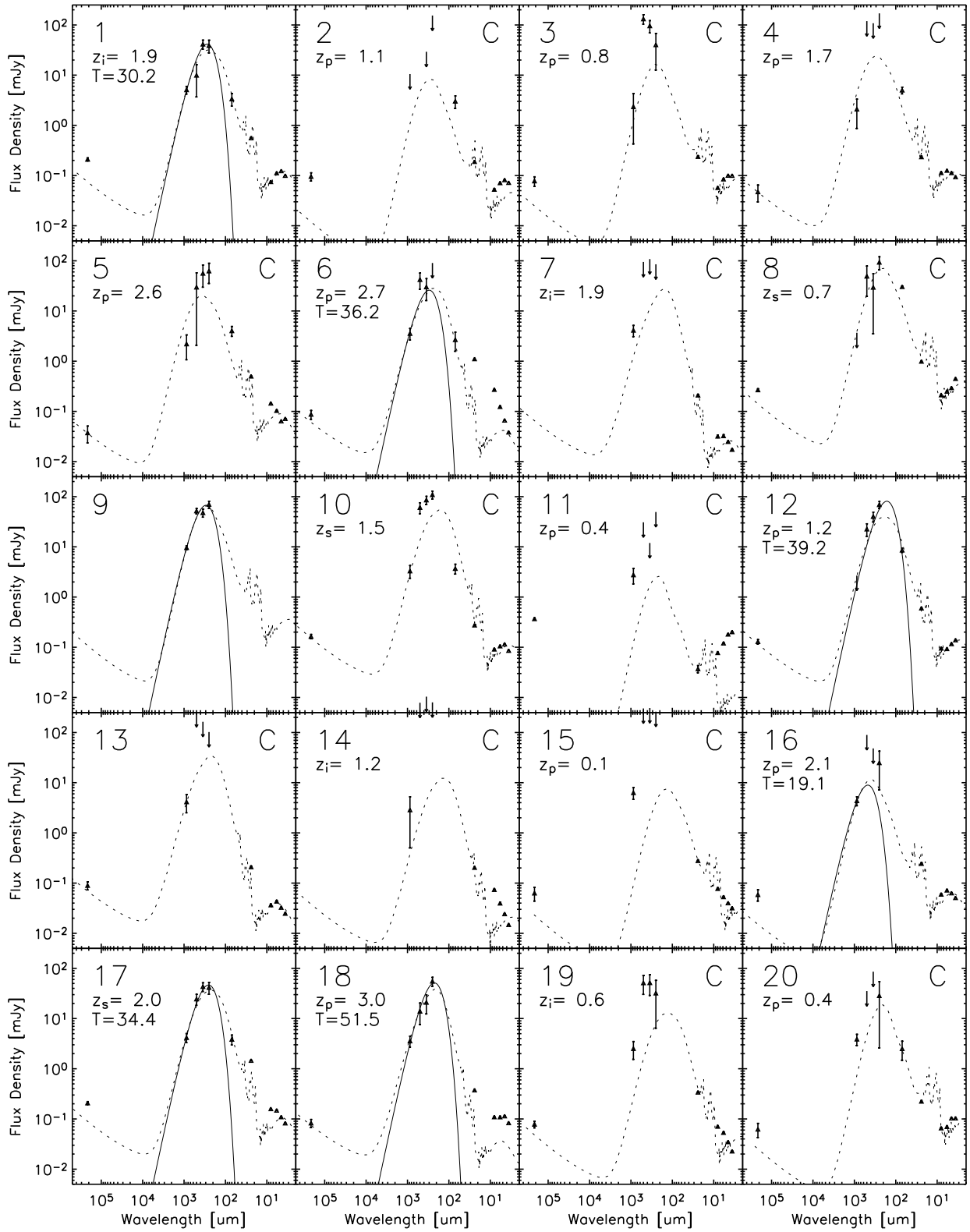

Figure E1. Observed-frame spectral energy distributions. The flux densities at all 118 positions are fit simultaneously in each submm map. In this way flux densities in blends are divided up. All matched sources have IRAC photometry from SIMPLE, and most sources also have 24 μm (and occasional 70 μm) flux densities from FIDEL. Most sources also have 1.4 GHz radio measurements. The only exceptions are sources for which the BLAST data have only been matched to an 870 μm peak from LESS, whose position has been used to re-measure flux densities in the BLAST bands (no SED information given). Redshift labels have the same meaning as in Fig. E1. Dotted lines are SED fits to the submm and FIR photometry using the library of Dale et al. (2001). The 'C' indicates 42 sources that are confused to the point that the submm photometry is unusable, and only the Dale et al. (2001) SEDs are fit (to the radio and mid/near-IR photometry). For the remaining 83 sources a modified blackbody with emissivity $\beta = 2.0$ has been fit, with the maximum-likelihood *rest-frame* temperatures indicated for the 73 sources with redshifts.

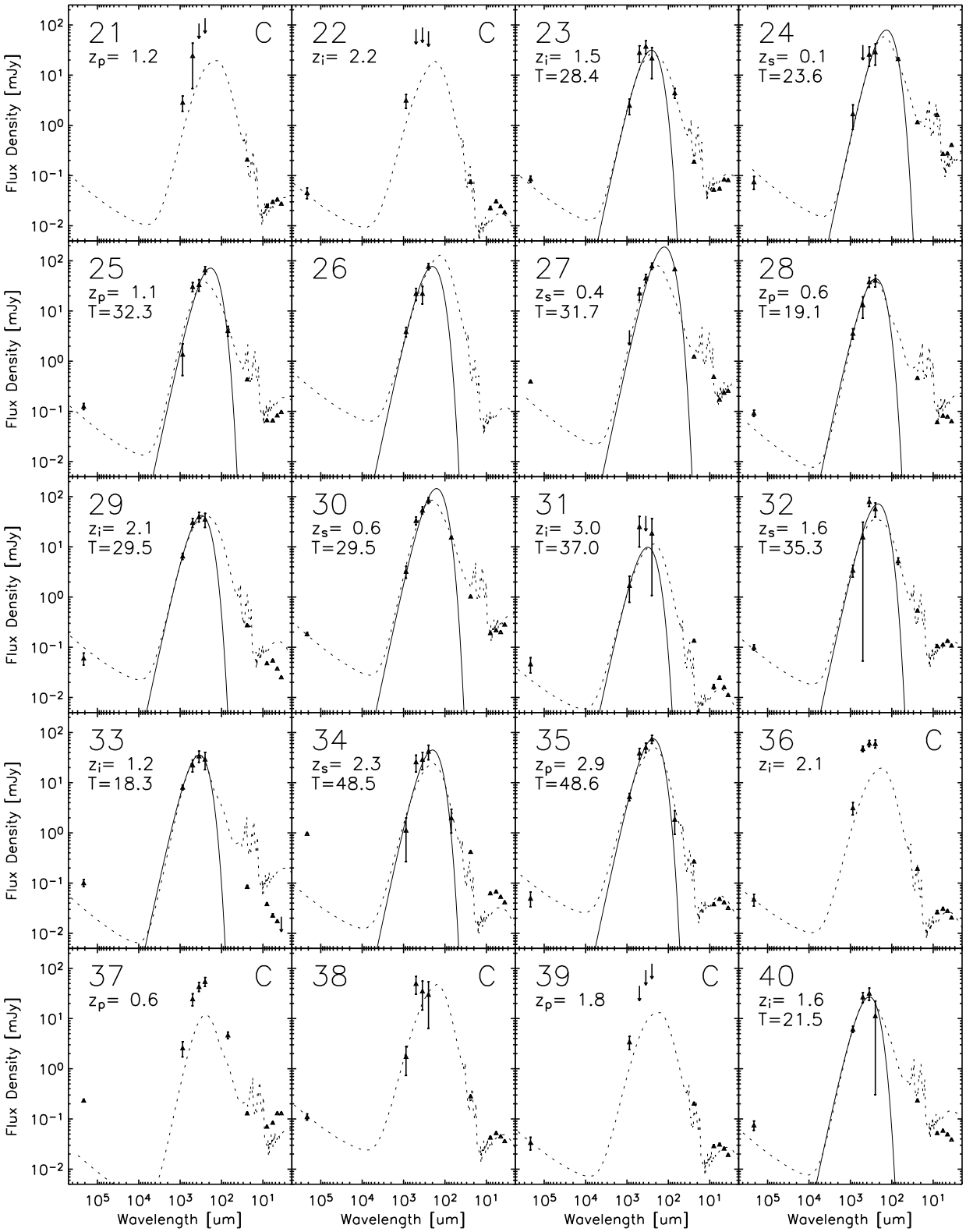
21
z_p= 1.2
C
22
z_i= 2.2
C
23
z_i= 1.5
T=28.4
24
z_s= 0.1
T=23.6
25
z_p= 1.1
T=32.3
26
27
z_s= 0.4
T=31.7
28
z_p= 0.6
T=19.1
29
z_i= 2.1
T=29.5
30
z_s= 0.6
T=29.5
31
z_i= 3.0
T=37.0
32
z_s= 1.6
T=35.3
33
z_i= 1.2
T=18.3
34
z_s= 2.3
T=48.5
35
z_p= 2.9
T=48.6
36
C
z_i= 2.1
37
C
z_p= 0.6
38
C
39
C
z_p= 1.8
40
z_i= 1.6
T=21.5
Flux Density [mJy]
Wavelength [um]

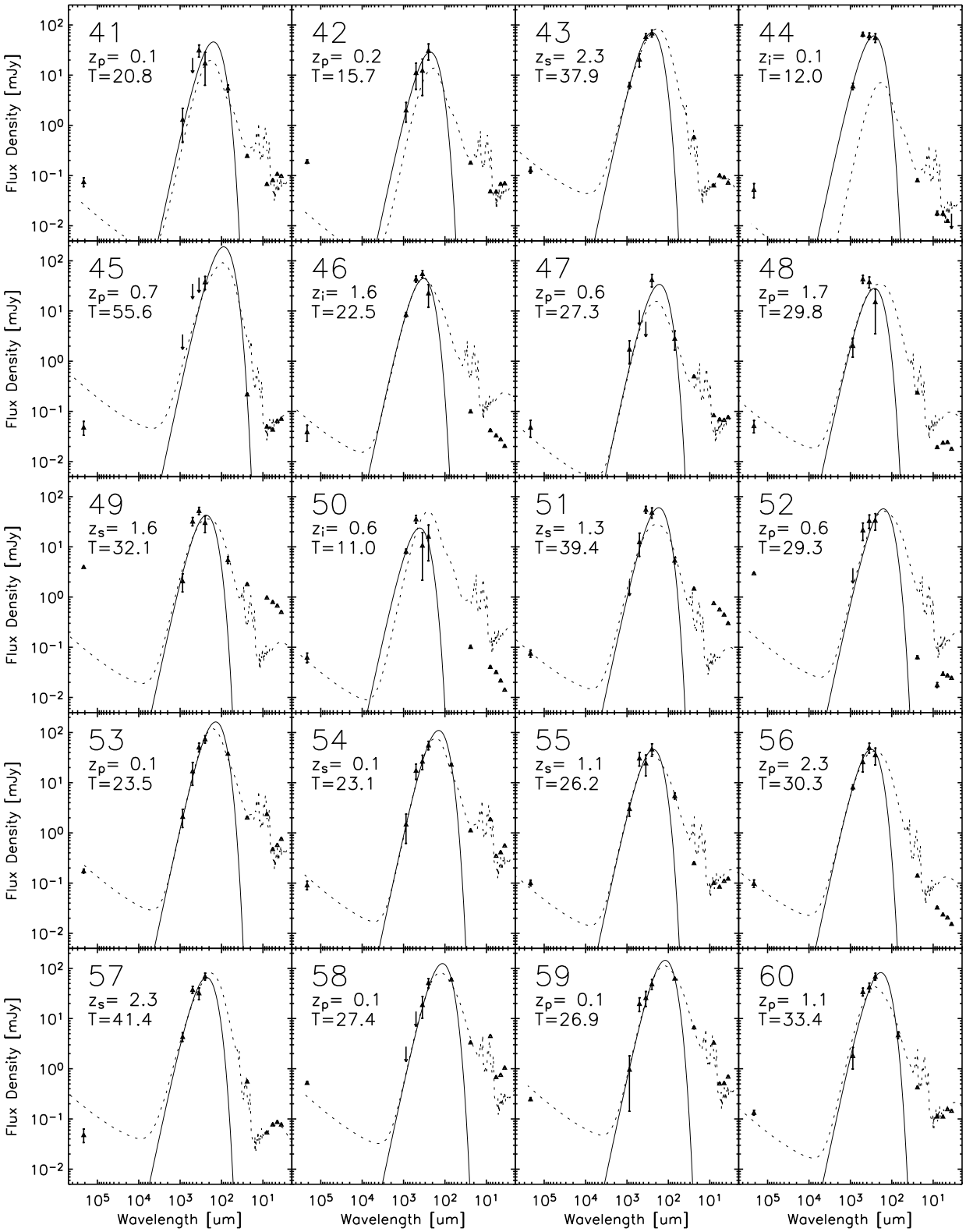
41
z_p= 0.1
T=20.8
42
z_p= 0.2
T=15.7
43
z_s= 2.3
T=37.9
44
z_i= 0.1
T=12.0
45
z_p= 0.7
T=55.6
46
z_i= 1.6
T=22.5
47
z_p= 0.6
T=27.3
48
z_p= 1.7
T=29.8
49
z_s= 1.6
T=32.1
50
z_i= 0.6
T=11.0
51
z_s= 1.3
T=39.4
52
z_p= 0.6
T=29.3
53
z_p= 0.1
T=23.5
54
z_s= 0.1
T=23.1
55
z_s= 1.1
T=26.2
56
z_p= 2.3
T=30.3
57
z_s= 2.3
T=41.4
58
z_p= 0.1
T=27.4
59
z_p= 0.1
T=26.9
60
z_p= 1.1
T=33.4
Flux Density [mJy]
Wavelength [um]

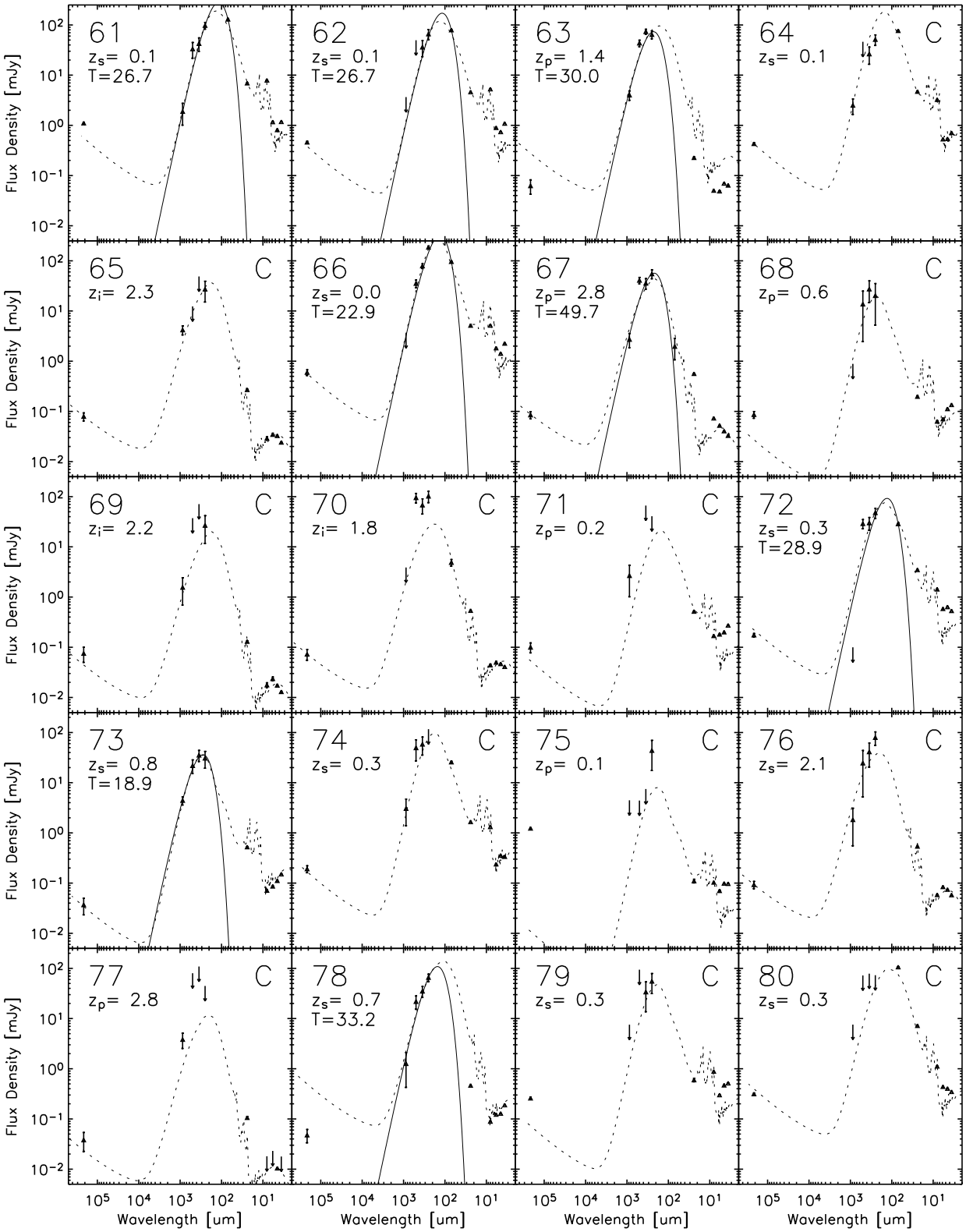
61
z_s= 0.1
T=26.7
62
z_s= 0.1
T=26.7
63
z_p= 1.4
T=30.0
64
C
z_s= 0.1
65
C
z_i= 2.3
66
z_s= 0.0
T=22.9
67
z_p= 2.8
T=49.7
68
C
z_p= 0.6
69
C
z_i= 2.2
70
C
z_i= 1.8
71
C
z_p= 0.2
72
z_s= 0.3
T=28.9
73
z_s= 0.8
T=18.9
74
C
z_s= 0.3
75
C
z_p= 0.1
76
C
z_s= 2.1
77
C
z_p= 2.8
78
z_s= 0.7
T=33.2
79
C
z_s= 0.3
80
C
z_s= 0.3
Flux Density [mJy]
Wavelength [um]

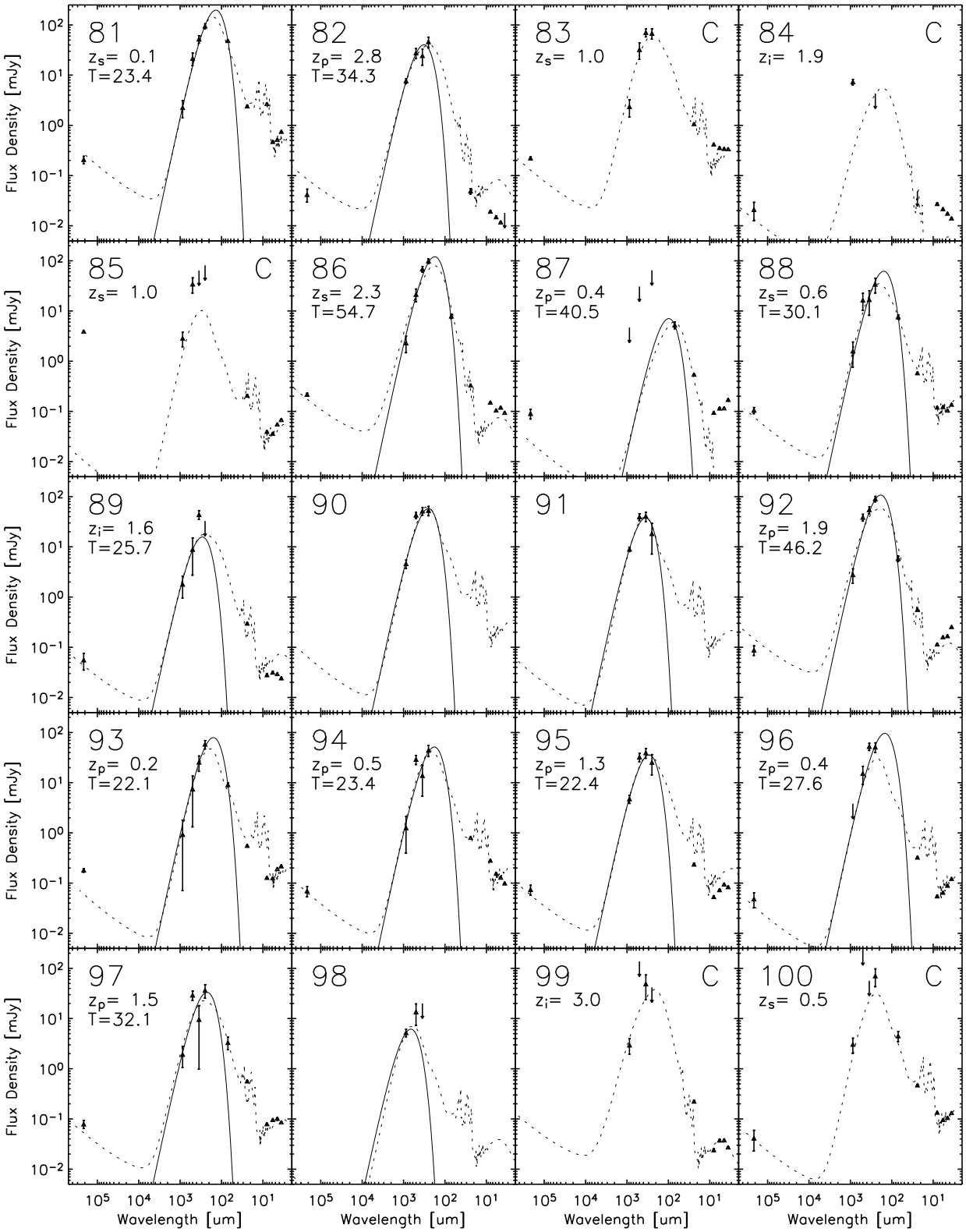
81
z_s= 0.1
T=23.4
82
z_p= 2.8
T=34.3
83 C
z_s= 1.0
84 C
z_i= 1.9
85 C
z_s= 1.0
86
z_s= 2.3
T=54.7
87
z_p= 0.4
T=40.5
88
z_s= 0.6
T=30.1
89
z_i= 1.6
T=25.7
90
91
92
z_p= 1.9
T=46.2
93
z_p= 0.2
T=22.1
94
z_p= 0.5
T=23.4
95
z_p= 1.3
T=22.4
96
z_p= 0.4
T=27.6
97
z_p= 1.5
T=32.1
98
99 C
z_i= 3.0
100 C
z_s= 0.5
Flux Density [mJy]
Wavelength [um]

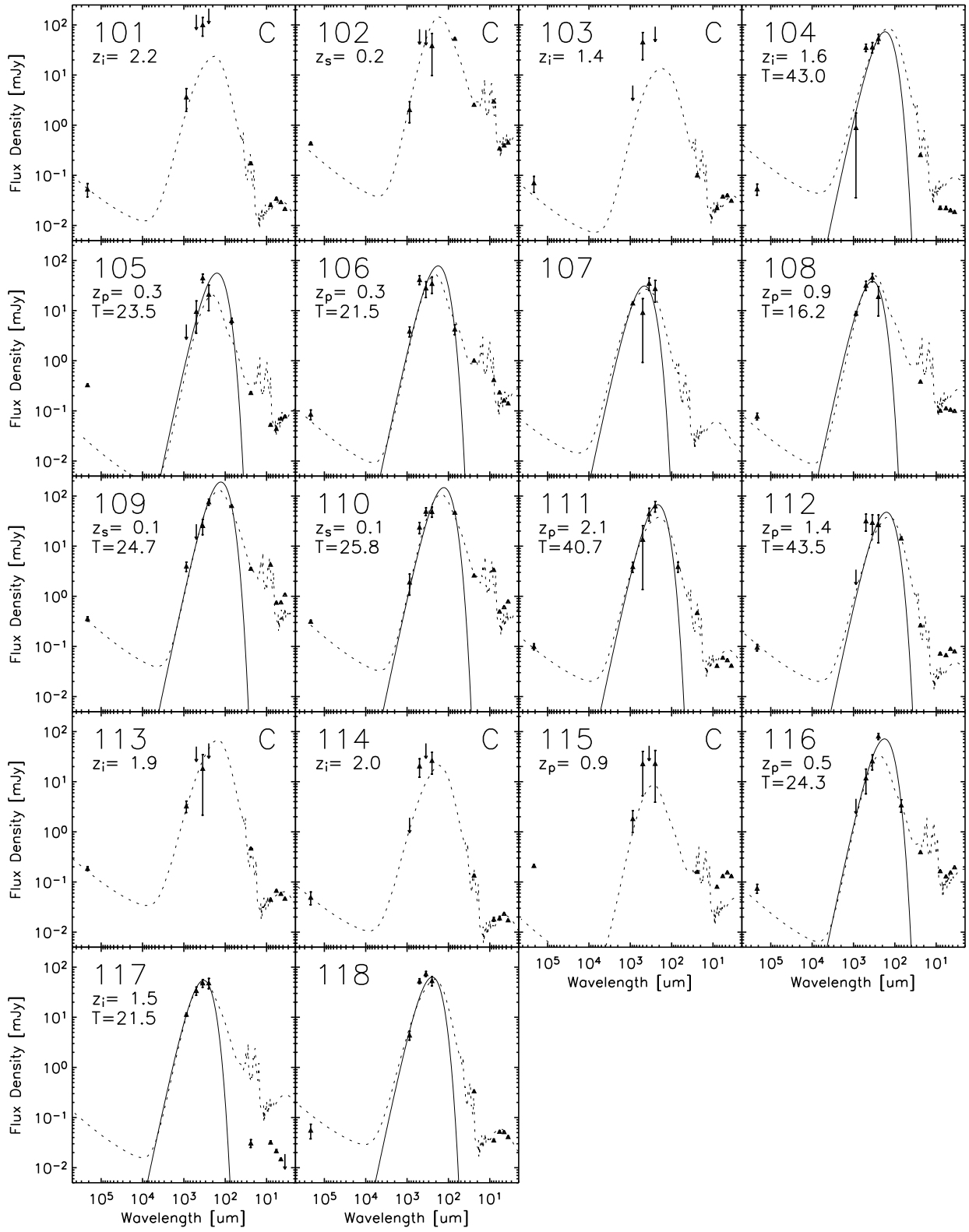
101
C
z_i= 2.2
102
C
z_s= 0.2
103
C
z_i= 1.4
104
z_i= 1.6
T=43.0
105
z_p= 0.3
T=23.5
106
z_p= 0.3
T=21.5
107
108
z_p= 0.9
T=16.2
109
z_s= 0.1
T=24.7
110
z_s= 0.1
T=25.8
111
z_p= 2.1
T=40.7
112
z_p= 1.4
T=43.5
113
C
z_i= 1.9
114
C
z_i= 2.0
115
C
z_p= 0.9
116
z_p= 0.5
T=24.3
117
z_i= 1.5
T=21.5
118
Flux Density [mJy]
Wavelength [um]